Geochemistry, Geophysics, Geosystems®

RESEARCH ARTICLE
10.1029/2022GC010724

# Estimating the Net Magnetic Moment of Geological Samples From Planar Field Maps Using Multipoles

**Eduardo A. Lima[1], Benjamin P. Weiss[1], Caue S. Borlina[1,2], Laurent Baratchart[3], and Douglas P. Hardin[4]**

[1]Department of Earth, Atmospheric, and Planetary Sciences, Massachusetts Institute of Technology, Cambridge, MA, USA, [2]Department of Earth and Planetary Sciences, Johns Hopkins University, Baltimore, MD, USA, [3]Centre de Recherche INRIA Sophia Antipolis-Méditerranée, Valbonne, France, [4]Department of Mathematics, Center for Constructive Approximation, Vanderbilt University, Nashville, TN, USA

**Key Points:**

- A spherical harmonic multipole expansion model can be used to estimate net magnetic moment from magnetic microscopy data
- Planar geometry and indeterminacy of the origin location for the multipole expansion require regularization of an ill-posed inverse problem
- Accurate moment estimates can be obtained for measurements of compact geological samples even with low signal-to-noise ratios

**Supporting Information:**

Supporting Information may be found in the online version of this article.

**Correspondence to:**

E. A. Lima,
limaea@mit.edu

**Citation:**

Lima, E. A., Weiss, B. P., Borlina, C. S., Baratchart, L., & Hardin, D. P. (2023). Estimating the net magnetic moment of geological samples from planar field maps using multipoles. *Geochemistry, Geophysics, Geosystems*, *24*, e2022GC010724. https://doi.org/10.1029/2022GC010724

Received 30 SEP 2022
Accepted 12 MAY 2023

**Abstract** Recent advances in magnetic microscopy have enabled studies of geological samples whose weak and spatially nonuniform magnetizations were previously inaccessible to standard magnetometry techniques. A quantity of central importance is the net magnetic moment, which reflects the mean direction and the intensity of the magnetization states of numerous ferromagnetic crystals within a certain volume. The planar arrangement of typical magnetic microscopy measurements, which originates from measuring the field immediately above the polished surface of a sample to maximize sensitivity and spatial resolution, makes estimating net moments considerably more challenging than with spherically distributed data. In particular, spatially extended and nonuniform magnetization distributions often cannot be adequately approximated by a single magnetic dipole. To address this limitation, we developed a multipole fitting technique that can accurately estimate net moment using spherical harmonic multipole expansions computed from planar data. Given that the optimal location for the origin of such expansions is unknown beforehand and generally unconstrained, regularization of this inverse problem is critical for obtaining accurate moment estimates from noisy experimental magnetic data. We characterized the performance of the technique using synthetic sources under different conditions (noiseless data, data corrupted with simulated white noise, and data corrupted with measured instrument noise). We then validated and demonstrated the technique using superconducting quantum interference device microscopy measurements of impact melt spherules from Lonar crater, India and dusty olivine chondrules from the CO chondrite meteorite Dominion Range 08006.

**Plain Language Summary** Rocks may acquire records of the ambient magnetic field that can be preserved over geological timescales. This occurs when ferromagnetic minerals in those rocks cool, crystallize, or experience a pressure pulse. Magnetic microscopes are very sensitive instruments that can measure weak magnetic fields produced by rock samples at close proximity. They enable the analysis of rocks that were previously inaccessible to traditional paleomagnetic instrumentation. However, special data analysis techniques are required for obtaining the magnetic record preserved in a rock from the measurements collected by a magnetic microscope. We developed a novel analytical technique that allows us to use those instruments to successfully study small rock samples with nonuniform magnetization. We validate and demonstrate the technique using magnetic microscopy measurements of impact spherules from Lonar crater, India and mineral grains extracted from the meteorite Dominion Range 08006.

## 1. Introduction

Records of magnetic fields have played a key role in understanding a diversity of processes related to tectonics and paleoclimate (Tauxe, 2010), evolution of the protoplanetary disk and planet formation (Weiss et al., 2021), planetary thermal evolution (Lapotre et al., 2020), and habitability (Ehlmann et al., 2016). The rock record of past magnetic fields is in the form of natural remanent magnetization, the semi-permanent statistical alignment of electron spins in grains of ferromagnetic minerals that can be preserved over geological timescales. This magnetization may be acquired when the ferromagnetic minerals cool, crystallize, or experience a transient increase in pressure. The field of paleomagnetism seeks to read such records to study the history of planetary processes.

Remanent magnetization is an emergent property representing the aggregate behavior of numerous individual electrons. In particular, it has been shown that statistically meaningful constraints on the strength and direction

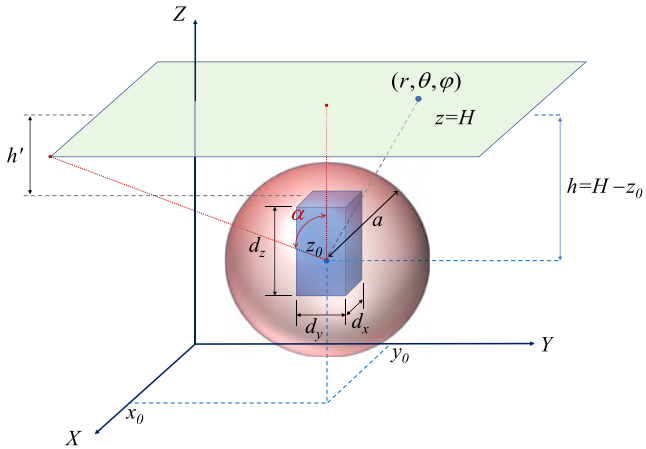


**Figure 1.** Schematic drawing depicting the main geometrical quantities involved. A sample with dimensions $d_x$, $d_y$, and $d_z$ is located below the measurement plane $z = H$ where data are collected. The origin of the spherical harmonic multipole expansion is located at ($x_0$, $y_0$, $z_0$), which is iteratively adjusted to attain the best representation of the data with the multipole model. The distance between the origin of the expansion and the measurement plane is defined as $h$. The sensor-to-sample distance, $h'$, is defined as the distance between the top of the sample and the measurement plane. A reference sphere [radius $a$, centered at ($x_0$, $y_0$, $z_0$)] for the multipole expansion encloses the sample. Planar mapping areas of finite size located solely above the sample result in the polar angle $\theta$ spanning a somewhat limited interval $0 \leq \theta \leq \alpha$, where $\alpha < \pi/2$, compared to spherical data collected around the sample, for which $0 \leq \theta \leq \pi$. ($\alpha$ is the largest value that the polar angle $\theta$ assumes for any point lying within the mapping area.) The evaluation of multipoles on these planar mapping areas make spherical harmonics of the same order but different degree become somewhat similar, resulting in corresponding multipole components that are much alike, as seen in Figure 2.

of ancient magnetic fields require measuring the net magnetic moment (volume integral of magnetization) of $10^4$ or more magnetic grains (Berndt et al., 2016; Kirschvink, 1981; Lima & Weiss, 2016). However, magnetization cannot be directly measured except within a very thin external layer of a geological sample. Instead, the magnetization or the net magnetic moment is typically estimated from measurements of the external magnetic field produced by a magnetized rock sample. The size of the volume in which the net moment is measured is a critical part of the analysis, given that a volume that is too small may fail to include a statistically sufficient number of magnetic grains to capture the paleomagnetic field direction and strength, whereas a volume that is too large may include regions in a geological sample with disparate geological histories and/or heterogeneous magnetic recording properties. Furthermore, for rocks that are weakly magnetized, a larger volume may be necessary to ensure a sufficiently large number of grains to be detectable with a magnetometer.

Typical magnetometers (e.g., spinner magnetometers and superconducting rock magnetometers) obtain net moment estimates for the whole volume of the sample through mathematical relationships that involve approximations associated with specific sample shapes, magnetization patterns, and detector geometries (Collinson, 1983). However, such relationships are often not directly applicable to magnetometers that map magnetic fields on a planar grid at high spatial resolution (e.g., scanning magnetic microscopes, quantum diamond microscopes, and magneto-optical imaging systems) owing to differences in measurement configuration and in the spatial scales involved.

For such magnetometers, one possible approach consists of first computing the inversion of magnetic data for the entire magnetization distribution within the sample (henceforth denoted "full inversion") and then integrating the solution to calculate the net magnetic moment, either in a sub-volume or over the whole sample. While this approach is more general and allows for the reconstruction of extended sources, this type of reconstruction unfortunately requires carefully chosen regularization strategies and selection of regularization parameters, and possibly additional analyses to constrain physical characteristics of the sources, to overcome ill-posedness and obtain physically meaningful solutions [e.g., (Egli & Heller, 2000; Lima et al., 2013; Myre et al., 2019; Pastore et al., 2018, 2021, 2022; Usui et al., 2012; Weiss et al., 2007)]. In practice, taking this approach is often too laborious and time-consuming for processing complete demagnetization sequences of geological samples, with no guarantee of obtaining accurate results for samples containing spatially extended and nonuniform magnetization patterns except in a handful of special cases [e.g., unidirectional or unidimensional magnetizations (Baratchart et al., 2013)]. Thus, for sources that are reasonably localized and exhibit a consistent geological history, other approaches that are tailored to such source characteristics may often be more advantageous for estimating net moment.

In particular, when the sample's dimensions are roughly comparable to the distance from the magnetic sensor to the sample, $h'$, or when field maps exhibit features that are sufficiently spatially isolated from those of adjacent sources, it is possible to estimate net moment by fitting a localized source model to the measured data (Lima & Weiss, 2016) (Figure 1). In its simplest form, this involves fitting a single magnetic dipole (i.e., three-component vector dipole moment and its location) to magnetic maps that are dominantly dipolar in behavior. The rationale for this approach is two-fold: (a) uniformly magnetized samples with certain geometries produce external magnetic fields that are either exactly dipolar (e.g., sphere) or are approximately dipolar at relatively short distances (e.g., cubes and cylinders with unity diameter-height ratio) (Collinson, 1983), and (b) for sufficiently large sensor-to-sample distances compared to the sample's dimensions or to the size of an isolated magnetic feature, the field produced is approximately dipolar.

Whereas the single-dipole fitting approach has been successfully used in many applications (Borlina et al., 2020, 2021; Fu et al., 2014, 2017, 2020; Weiss et al., 2007, 2008, 2018), there still are many samples for which

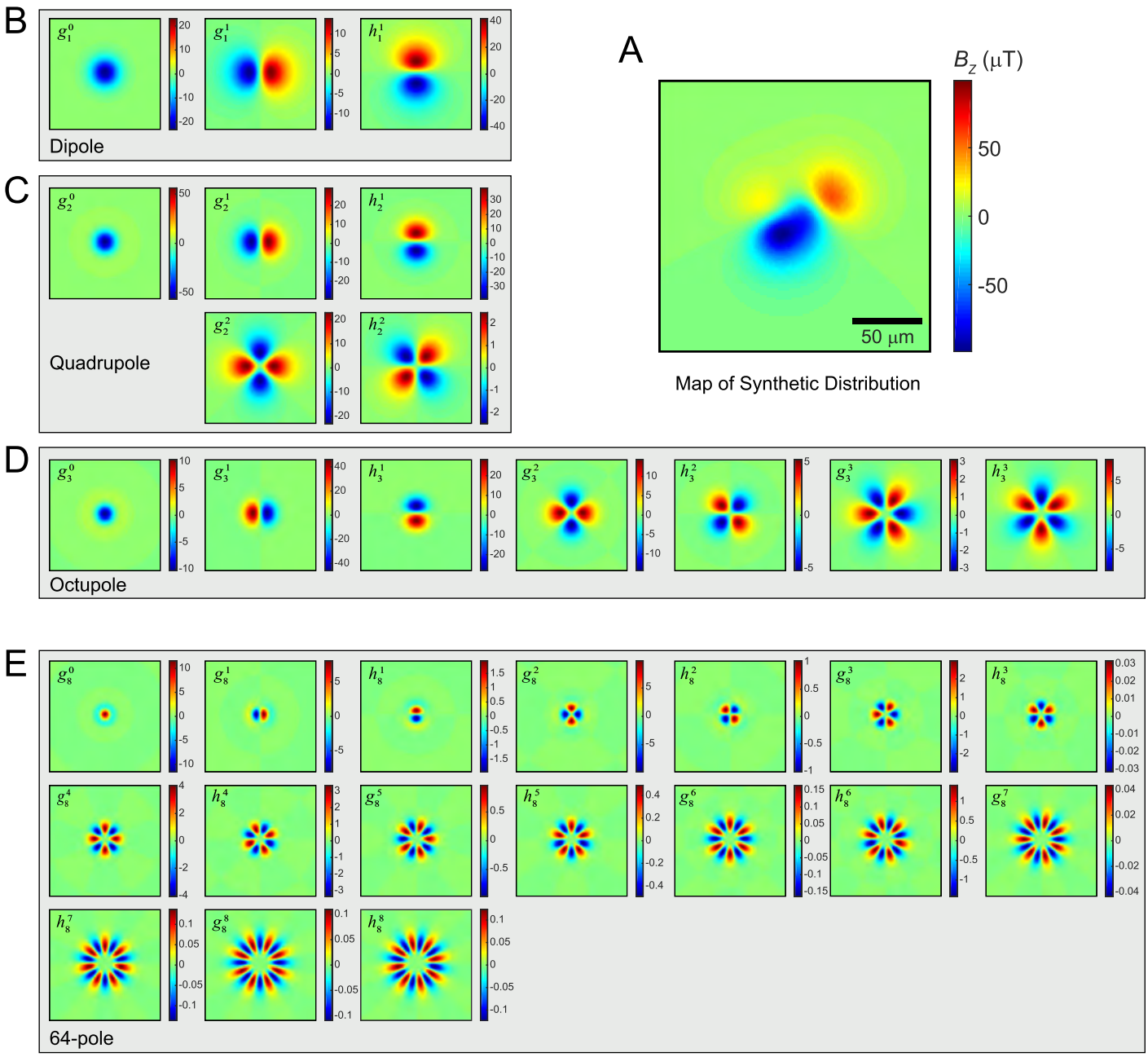


**Figure 2.** Synthetic source distribution (Source A—see Table 2) and its recovered decomposition into a multipole series truncated at degree 8. (a) Simulated map of $B_z$ of Source A with a sensor-to-sample distance of 25 μm. (b–e) Multipole components for degrees 1 (b), 2 (c), 3 (d), and 8 (e) are shown (field units in μT). Notice that, in the planar setting, there is remarkable similarity (except for possible sign changes) of multipole components of the same order $m$ but different degree $n$, such as the first three components in each multipole. For each map in (b–e), the corresponding coefficient in the spherical harmonic multipole expansion is indicated.

such a model does not yield high-accuracy estimates for net moment, particularly when small sensor-to-sample distances relative to the physical size of the source are involved. One way to ameliorate this issue consists of upward-continuing the field map to a greater equivalent sensor-to-sample distance so as to decrease the influence of high-order source terms (Fu et al., 2020). However, this strategy has limitations set by the size of the mapping area and magnetic noise, each of which introduce errors in the upward continued magnetic data and may lead to inaccurate moment estimates [see Fu et al. (2020) and Text S1 in Supporting Information S1].

In view of this, increasing the complexity of the source model while avoiding solving a full inversion for magnetization can often be advantageous. An appealing approach consists of adding higher order multipoles (quadrupole,

octupole, hexadecapole, and so forth) to the dipole model given that multipole expansions of the magnetostatic field can approximate arbitrarily well the field produced by a finite magnetic source outside a sphere enclosing this source and therefore improve over single-dipole fits. In fact, multipoles can be interpreted as an infinite collection of point sources in an arbitrarily small region centered around a reference point (the origin of the multipole expansion) that exactly reproduces the observed magnetic field (Wikswo & Swinney, 1985). Although these individual point sources very rarely correspond to the actual magnetization distribution within a magnetic material producing the measured magnetic field, they possess useful mathematical properties and can sometimes be related to physical quantities of interest [see, for instance, Cortes-Ortuno et al. (2021, 2022) for an application of low-order multipoles to constrain the internal magnetization structure of magnetic grains analyzed with micromagnetic tomography]. Two drawbacks of multipole expansions are that (a) multipoles with orders higher than that of a dipole are strongly dependent on the location of the origin, making their physical interpretation challenging (Lowes, 1994), and (b) multipoles are inefficient for representing extended sources, especially those with asymmetrical dimensions, because a very large number of terms is required to adequately reproduce the magnetic field of such source configurations. Nevertheless, they allow us to invert much more complex field maps for net moment than a single-dipole model does, thus significantly expanding the suite of geological samples that can be effectively analyzed using high-resolution magnetometry.

Spherical harmonic expansions are intricately related to multipole expansions given that they provide a minimal, non-redundant series of multipole components that represent solutions to Laplace's equation (i.e., harmonic functions) in spherical domains (Wikswo & Swinney, 1984). In particular, spherical harmonics are functions defined on a sphere and constitute an orthogonal basis for twice-differentiable spherical functions (Courant & Hilbert, 1991). Spherical harmonic multipole expansions, which contain a radial term, can be used to represent harmonic functions in the whole space outside a reference sphere $r = a$ encompassing the sources.

The magnetic field outside a reference sphere of radius, $a$, enclosing all magnetic sources can be represented as the gradient of a scalar potential, $V$,

$$\vec{B} = -\mu_0 \nabla V, \tag{1}$$

where $\mu_0$ is the magnetic permeability in vacuum and we follow the convention used in physics for the magnetic scalar potential (Jackson, 1999). The potential $V$ satisfies Laplace's equation $\nabla^2 V = 0$ whose solution for $r > a$ can be expressed as the spherical harmonic multipole expansion:

$$V(r,\theta,\varphi) = a \sum_{n=1}^{\infty} \left(\frac{a}{r}\right)^{n+1} \sum_{m=0}^{n} (g_n^m \cos m\varphi + h_n^m \sin m\varphi) P_n^m(\theta), \tag{2}$$

where $r, \theta, \varphi$ denote the radial distance, polar angle and azimuthal angle, respectively, following the International Organization for Standardization (ISO) convention, $a$ is the radius of the reference sphere (units of meters), $g_n^m$ and $h_n^m$ are the Gauss coefficients (units of T), and $P_n^m(\theta)$ is the associated Legendre polynomial of order $m$ and degree $n$ normalized according to Schmidt's scheme (also called the Schmidt quasi-normalized function of order $m$ and degree $n$).

Very importantly, the coefficients of the dipole term ($n = 1$) in a multipole expansion are the components of the net magnetic moment of the underlying magnetization distribution. While this may appear trivial, in general expansions using different basis functions (e.g., rectangular harmonics, spherical cap harmonics, and Taylor expansions) will not have the property of concentrating net moment information in just the first three coefficients [e.g., (Wikswo & Swinney, 1984)]. Moreover, in magnetostatics, the dipole term is invariant with respect to the placement of the origin of the multipole expansion, which is expected given that the net moment is a physical quantity that must not depend on a particular choice for origin. More generally, the first nonzero term in a multipole expansion is translation-invariant (Raab, & de Lange, 2005). In electrostatics, the monopole term (i.e., net electric charge) is the translation-invariant term. Therefore, for spherical magnetic potential (or field) data, one could obtain the net magnetic moment by directly computing the spherical harmonic integral formulas for the three dipole coefficients independently (Butkov, 1968):

$$g_1^0 = \frac{3R^2}{a^3} \int_0^{\pi} V(R,\theta,\varphi) \sin\theta \, d\theta, \tag{3}$$

$$g_1^1 = \frac{3}{4\pi}\frac{R^2}{a^3}\int_0^{2\pi}\int_0^{\pi} V(R,\theta,\varphi)P_1^1(\theta)\sin\theta\cos\varphi\, d\theta\, d\varphi, \tag{4}$$

$$h_1^1 = \frac{3}{4\pi}\frac{R^2}{a^3}\int_0^{2\pi}\int_0^{\pi} V(R,\theta,\varphi)P_1^1(\theta)\sin\theta\sin\varphi\, d\theta\, d\varphi, \tag{5}$$

where $R$ is the radius of the sphere where magnetic data are available.

A fundamental difference that arises when applying spherical harmonic multipole expansions in a planar setting is that restrictions of spherical harmonics to the plane where magnetic field data are measured are no longer orthogonal in that subspace. However, such restrictions still constitute a set of (non-orthogonal) basis functions for restrictions (to the same plane) of the magnetic field of sources encompassed by the reference sphere. Therefore, one cannot retrieve coefficients of the expansion independently by integrating the planar magnetic data against elements of the basis [i.e., computing the orthogonal projections of the data onto the individual elements of the basis via inner products, as in Equations 3–5 above]. Instead, a system of linear equations must be solved to find all coefficients simultaneously. Clearly, the multipole expansion must be truncated at a certain degree for this approach to be computationally feasible.

In other words, for planar magnetic field data, computation of the dipole term coefficients is no longer decoupled from the computation of higher order terms in the spherical harmonic multipole expansion. In this case, the coefficients in a truncated multipole expansion are typically found by solving the abovementioned system of linear equations via least-squares methods, which is often nontrivial. In particular, some of the restrictions of spherical harmonics basis functions to the plane are somewhat similar (Figure 2) owing to the fact that the polar angle $\theta$ does not take any values outside the interval $0 \leq \theta \leq \alpha$ in this case, where $\alpha < \frac{\pi}{2}$ is set by the size of the mapping area and represents the maximum angle between the vertical axis and a vector representing a point on the edge of the mapping area. Adding to this, the large variation in the magnitude of the coefficients coupled with sampling in the space of (noisy) magnetic field data make it a numerically delicate problem, requiring regularization of this discrete ill-posed inverse problem. [An in-depth discussion about the ill-posedness of estimating net magnetic moment from planar magnetic data in general can be found in Baratchart et al. (2019)].

Importantly, whereas the orthogonality properties of spherical harmonic multipole expansions ensure that higher degree terms all have zero net magnetic moment, these terms nonetheless affect the *computation* of the coefficients of the dipole term. That is to say, the dipole term coefficients found via least-squares using a spherical harmonic expansion truncated at the dipole term will be, in general, different than those found using a spherical harmonic multipole expansion truncated at a higher multipole. This stems from the fact that, for non-dipolar magnetization, the magnetic field produced by a higher degree model will be much closer to the observed field than that produced by a lower degree model, thus yielding lower residuals. Hence, the computation of the dipole term will be less influenced by an attempt to reproduce complex features in the field map with lower degree terms, as higher-order multipoles in the expansion will be used instead to better approximate those features. Owing to the ill-posedness of this inverse problem, better reproduction of the observed field map does not necessarily translate into more accurate net moment estimates. Nevertheless, a general trend exists between the degree at which the spherical harmonic multipole expansion is truncated (model degree) and the accuracy in estimating the net moment in the noiseless case. (In fact, this may be surmised from approximation-theoretic considerations, which are outside the scope of this paper. We refer the more mathematically proficient readers to Text S2 in Supporting Information S1 for a proof that spherical harmonic multipole expansions can represent planar magnetic data arbitrarily well).

A further complication in this approach, and one that also applies to spherical data, is the placement of the origin of the spherical harmonic multipole expansion. For any potential field (magnetic, electric or gravity), the location of the origin of a multipole expansion cannot be constrained solely by the field data, since any place should work as long as the reference sphere (which is centered on the origin) encompasses the field sources. However, unlike for gravity, where a center of mass is a natural candidate for placement of the origin given that it enables elimination of the degree-1 term in spherical harmonic expansions of the gravitational potential (Couch et al., 2013; Lowrie & Fichtner, 2020), magnetic problems lack an easily identifiable "center of magnetization" (Lowes, 1994). Even so, the origin placement does have a strong effect on how rapidly the multipole series converges. To illustrate this point, consider a magnetic source comprised of just a single dipole located at position

$\vec{r}_0$. If we compute a spherical harmonic multipole expansion centered at $\vec{r}_0$, such a series will have exactly one nonzero term, namely the dipole term. However, if we instead compute an expansion centered at $\vec{r}_0 + \Delta\vec{r}$, there will be a multitude of nonzero terms (in fact, an infinite number), which are required to reproduce the field of a displaced dipole. The dipole coefficients in the two series will be identical, as they represent the net magnetic moment of the source distribution.

When using non-spherical, incomplete data (i.e., known only in a finite number of points within a limited region) and a truncated multipole expansion model, this fact has a significant impact: a particular choice for origin location may require a much higher degree model to adequately represent the data than a different choice for origin location. On the other hand, we can use this to find the optimal location of the origin as that where a truncated multipole expansion of degree $N$ best represents the data. This is the general strategy we adopt in this paper: for any given origin candidate location (which, as we will show, is provided by a nonlinear optimization algorithm), we find the multipole expansion coefficients via linear least squares and calculate the cost function value associated with that position (i.e., a measure of the difference between model and experimental field maps). We then select the position yielding the smallest cost function value.

To summarize, our choice of using truncated spherical harmonic multipole expansions to enhance our model stems from properties such as (a) the net moment information is concentrated in just the first three coefficients; (b) the dipole term is translation-invariant (for a non-truncated expansion, strictly speaking); (c) higher-order terms have zero net moment; (d) simple recursive formulas allow us to compute the expansion up to an arbitrary degree; and (e) spherical harmonic expansions do not contain redundant terms (i.e., they form an orthogonal basis for the solution space of Laplace's equation in a spherical setting).

We describe in detail our method in Section 2. Given that this work is multi-disciplinary in nature and to make it more accessible and self-contained to a broader audience, which may be less familiar with some mathematical or instrumentation aspects, we present and review a few concepts related to spherical harmonics, linear algebra, magnetic mapping, and sensor noise. We suggest readers with a firmer grasp of these concepts to skip over most of Sections 2.1 and 2.3.

## 2. Method

Prior to describing our method in detail, we briefly comment on alternative methods of net moment estimation. A previous work investigated the conversion of properties and results from spherical harmonic multipole expansions to the planar setting via Kelvin transforms (Baratchart et al., 2017). This formal approach makes it explicit the dependence of the net moment on multipole terms other than the dipole in the rectangular case while also revealing alternative methods for moment estimation using Fourier analysis and asymptotics. A different method consists of formulating net moment estimation as a bounded extremal problem, which allows for the calculation of both local net moments (i.e., moment of a select region of the magnetization) under certain conditions and global net moments, but results in increased theoretical and computational complexity (Baratchart et al., 2019). The multipole method described below exhibits a balance between noise tolerance, computational complexity, and mapping area requirements that bridge the domain covered by those alternative approaches for the computation of global net moments.

### 2.1. Theoretical Considerations

We start the derivation of our multipole model by recalling that the magnetic field outside a reference sphere of radius $a$ encompassing all the sources can be expressed as the gradient of a magnetic scalar potential $V$ [see Equations 1 and 2]. Because the magnetic scalar potential cannot usually be measured directly, we derive explicit formulas for the three components of the magnetic field by inserting Equation 2 into Equation 1 and calculating the gradient in spherical coordinates (Cain et al., 1967):

$$B_r(r,\theta,\varphi) = -\mu_0 \frac{\partial V}{\partial r} = \mu_0 \sum_{n=1}^{N} \left(\frac{a}{r}\right)^{n+2} (n+1) \sum_{m=0}^{n} (g_n^m \cos m\varphi + h_n^m \sin m\varphi) P_n^m(\theta) \tag{6}$$

$$B_\varphi(r,\theta,\varphi) = -\mu_0 \frac{1}{r\sin\theta} \frac{\partial V}{\partial \varphi} = \frac{\mu_0}{\sin\theta} \sum_{n=1}^{N} \left(\frac{a}{r}\right)^{n+2} \sum_{m=0}^{n} m(g_n^m \sin m\varphi - h_n^m \cos m\varphi) P_n^m(\theta) \tag{7}$$

$$B_\theta(r,\theta,\varphi) = -\mu_0 \frac{1}{r}\frac{\partial V}{\partial \theta} = -\mu_0 \sum_{n=1}^{N}\left(\frac{a}{r}\right)^{n+2}\sum_{m=0}^{n}(g_n^m \cos m\varphi + h_n^m \sin m\varphi)\frac{\partial P_n^m(\theta)}{\partial \theta}, \tag{8}$$

where we have truncated the spherical harmonic multipole expansion at a maximum degree, $N$, corresponding to the $N$th multipole. The Schmidt quasi-normalized functions and their derivatives can be recursively calculated. We express these recursion formulas in terms of Gauss-Laplace functions $P^{n,m}(\theta)$, which use a different normalization of the associated Legendre polynomials and lead to simpler recursion formulas than those using $P_n^m(\theta)$, and then renormalize the functions according to Schmidt's scheme:

$$\begin{cases} P^{0,0}(\theta) = 1 \\ P^{n,n}(\theta) = (\sin\theta)P^{n-1,n-1}(\theta), \text{for } n \geq 1 \text{ and } m = n \\ P^{n,m}(\theta) = (\cos\theta)P^{n-1,m}(\theta) - K^{n,m}P^{n-2,m}(\theta), \text{for } n \geq 1 \text{ and } m \neq n \end{cases}$$
$$\begin{cases} \dfrac{\partial P^{0,0}}{\partial\theta}(\theta) = 0 \\ \dfrac{\partial P^{n,n}}{\partial\theta}(\theta) = (\sin\theta)\dfrac{\partial P^{n-1,n-1}}{\partial\theta}(\theta) + (\cos\theta)P^{n-1,n-1}(\theta), \text{for } n \geq 1 \text{ and } m = n \\ \dfrac{\partial P^{n,m}}{\partial\theta}(\theta) = (\cos\theta)\dfrac{\partial P^{n-1,m}}{\partial\theta}(\theta) - (\sin\theta)P^{n-1,m}(\theta) - K^{n,m}\dfrac{\partial P^{n-2,m}}{\partial\theta}(\theta), \text{for } n \geq 1 \text{ and } m \neq n, \end{cases} \tag{9}$$

where $K^{n,m} = \frac{(n-1)^2-m^2}{(2n-1)(2n-3)}$. Notice that, although the recursion formulas for $n = 1, m = 0$ contain terms with negative values for the first index, this is not an issue given that such terms are multiplied by $K^{1,0} = 0$ and therefore ignored.

The Schmidt quasi-normalized function are then obtained by means of the scaling factors $S^{n,m}$:

$$P_n^m(\theta) = S^{n,m}P^{n,m}(\theta), \tag{10}$$

where these scaling factors are also computed recursively

$$\begin{cases} S^{0,0} = 1 \\ S^{n,0} = S^{n-1,0}\left(2 - \dfrac{1}{n}\right), \text{for } n \geq 1 \text{ and } m = 0 \\ S^{n,m} = \sqrt{\dfrac{C(n-m+1)}{n+m}}S^{n,m-1}, \text{for } n \geq 1 \text{ and } m \neq 0, \end{cases} \tag{11}$$

$$\text{and } C = \begin{cases} 2, \text{if } m = 1 \\ 1, \text{otherwise.} \end{cases}$$

The measurement configuration most commonly used in scanning magnetic microscopes and magnetic imaging systems is best described using a Cartesian coordinate system (Figure 1) and is based on the detection of the field component normal to the sample plane (i.e., the $B_z$ component; see Section 2.3.1):

$$B_z(r,\theta,\varphi) = (\cos\theta)B_r(r,\theta,\varphi) - (\sin\theta)B_\theta(r,\theta,\varphi). \tag{12}$$

Substituting Equations 6 and 8 in Equation 12, we get

$$B_z(r,\theta,\varphi) = \mu_0 \sum_{n=1}^{N}\left(\frac{a}{r}\right)^{n+2}\sum_{m=0}^{n}\left[(n+1)\cos(\theta)P_n^m(\theta) + \sin(\theta)\frac{\partial P_n^m(\theta)}{\partial\theta}\right](g_n^m \cos m\varphi + h_n^m \sin m\varphi). \tag{13}$$

Note that although we will focus our analysis on the $z$-component of the field, which exhibits the important property of rotational invariance, expressions for other Cartesian field components can be easily derived from Equations 6 to 8 and suitable conversion formulas between vector components in spherical and Cartesian coordinate systems.

It is important to realize that Equation 13 shows that $B_z$ (and more generally, the vector magnetic field $\vec{B}$) depends linearly on the coefficients $g_n^m$ and $h_n^m$, with terms in $r, \theta, \varphi$ acting as basis functions. That is to say, $B_z$ is a linear combination of basis elements in a function space and $g_n^m$ and $h_n^m$ represent the coefficients of this linear

combination. This allows us to express such a relationship in matrix form for a finite number, $K$, of discrete magnetic field measurements:

$$\begin{bmatrix} Q_1^{1,0} & Q_1^{1,1} & R_1^{1,1} & Q_1^{2,0} & \dots & R_1^{N,N} \\ Q_2^{1,0} & Q_2^{1,1} & R_2^{1,1} & Q_2^{2,0} & \dots & R_2^{N,N} \\ \vdots & \vdots & \vdots & \vdots & & \vdots \\ Q_K^{1,0} & Q_K^{1,1} & R_K^{1,1} & Q_K^{2,0} & \dots & R_K^{1,N} \end{bmatrix} \begin{bmatrix} g_1^0 \\ g_1^1 \\ h_1^1 \\ g_2^0 \\ \vdots \\ h_N^N \end{bmatrix} = \begin{bmatrix} B_z(r_1,\theta_1,\varphi_1) \\ B_z(r_2,\theta_2,\varphi_2) \\ \vdots \\ B_z(r_K,\theta_K,\varphi_K) \end{bmatrix}, \text{ or } \mathbf{Aw} = \mathbf{b}, \tag{14}$$

where $Q_k^{n,m} = \mu_0 \left(\frac{a}{r_k}\right)^{n+2} \left[(n+1)\cos(\theta_k) P_n^m(\theta_k) + \sin(\theta_k) \frac{\partial P_n^m(\theta)}{\partial \theta}|_{\theta=\theta_k}\right] \cos m\varphi_k$ and $R_k^{n,m} = \mu_0 \left(\frac{a}{r_k}\right)^{n+2} \left[(n+1)\cos(\theta_k) P_n^m(\theta_k) + \sin(\theta_k) \frac{\partial P_n^m(\theta)}{\partial \theta}|_{\theta=\theta_k}\right] \sin m\varphi_k$.

For a source model of degree $N$ (i.e., containing $N$ multipoles), there are $N^2 + 2N$ Gauss coefficients to be determined. We generally wish to work with overdetermined systems of linear equations so as to better constrain the solution in the presence of noise. That means that the number of points in the magnetic field map should satisfy $K > N^2 + 2N$.

The Cartesian components of the net magnetic moment are related to the first three Gauss coefficients (Blakely, 1996) as follows:

$$\begin{aligned} m_x &= 4\pi a^3 g_1^1 \\ m_y &= 4\pi a^3 h_1^1, \\ m_z &= 4\pi a^3 g_1^0 \end{aligned} \tag{15}$$

where the scaling factor $1/\mu_0$ has already been incorporated by means of the definition used in Equation 1. Thus, by solving the system of linear Equation 14, we can compute an estimate for the net moment just using the first three Gauss coefficients in the vector **w** (i.e., the dipole coefficients).

However, this presupposes that an origin for the multipole expansion has been chosen so that each of the coordinates $r_k, \theta_k, \varphi_k$ representing the vector from the origin to a given measurement position, $k$, can be computed and the matrix **A** can be constructed. As we discussed before, the location of the origin of the expansion is generally not constrained in the magnetostatics case. We next see how this can be done in a practical manner.

### 2.2. Basic Algorithm

For a set maximum model degree $N_{\max}$, we use the following procedure to obtain a moment estimate:

1. Obtain an approximate estimate for the origin location based on inspection of the field map of the sample and on an estimate for the sensor-to-sample distance. The total field map, which can be computed from the $B_z$ map (Lima & Weiss, 2009), typically attains its maximum over the magnetic source and this location provides an estimate for the optimal horizontal coordinates of the origin that is somewhat independent of the magnetization direction. The sensor-to-sample distance provides a lower limit for the vertical coordinate of the origin. If appropriate, sample thickness can also be incorporated into the vertical coordinate estimation.
2. Arrange field map data as a column vector **b.**
3. **Loop A:** starting with model degree $N = 1$ (dipole) and increasing at each iteration, repeat steps (3.a) through (3.d) until the model degree exceeds $N_{\max}$.
   - 3.a **Loop B:** generate an initial guess for the origin location by introducing random perturbations to the three coordinates obtained in (1) and pass it to a non-linear optimization algorithm (e.g., Levenberg-Marquardt, trust-region-reflective, or quasi-Newton methods) along with the magnetic data vector **b.**
     - 3.a.1 **Loop C:** populate all $K\left(N^2 + 2N\right)$ entries of matrix **A** according to the current guess for the origin location.

3.a.2 Solve the system of linear Equation 14 for the multipole expansion coefficients **w** using linear least-squares methods.

3.a.3 Compute the modeled field data $\tilde{\mathbf{b}}$ by multiplying matrix **A** by the solution vector **w**.

3.a.4 Calculate the residuals $\tilde{\mathbf{b}} - \mathbf{b}$ and their Euclidean norm normalized by the number of field measurements available, $\varepsilon = \frac{1}{K}\sqrt{\sum_{k=1}^{K}\left(\tilde{b}_k - b_k\right)^2}$. The Euclidean norm of the residuals is assigned as the value of the cost function for that choice of origin location.

3.a.5 Using the nonlinear optimization algorithm, compute a new candidate for the origin location based on the residuals/cost function behavior.

3.a.6 **End C:** quit optimization if the (local/global) minimum of the cost function is reached or the maximum number of iterations is exceeded.

3.b Obtain the net moment associated with the final solution provided by the optimization algorithm and store it for subsequent comparison. Moment estimate is computed by plugging the first three components of **w** into Equation 15.

3.c **End B:** exit loop after computing ≥30 solutions using different initial guesses for the origin location.

3.d Compare solutions and establish which one attains the global minimum of the cost function. The net moment vector associated with the global minimum is then set as the estimate obtained for a given model degree *N*.

4. **End A:** exit loop if residuals for the current model degree are uncorrelated and at noise level or if moment estimates begin to diverge rapidly
5. Select final solution based on stability of the estimates and low residuals.

It is typically not advantageous to use models containing multipoles of order higher than necessary to adequately represent the magnetic field data given that both numerical instability, noise magnification, and computational time increase with model degree. In addition, this may often lead to overfitting, which manifests as the cancellation of noise in the central region of the field map because high-degree models progressively become capable of reproducing rapid variations in the field map related to noise in that region as model complexity increases (this issue is illustrated in Section 3.2). Thus, one may expect net moment estimates to converge to a steady value and then start to diverge as the number of multipoles in the model increases.

## 2.3. Numerical and Experimental Considerations

### 2.3.1. Magnetic Microscopy Instruments and Measurement Configurations

Magnetic microscopes can be broadly divided into two different categories: (a) scanning microscopes and (b) imaging microscopes (Table 1). Although they can be treated indistinguishably in many situations, specific characteristics sometimes need to be considered to better capture the nature of the magnetic data being analyzed. For instance, different magnetic sensing technologies may exhibit distinct noise characteristics, which in turn may impact moment estimation accuracy in different ways.

In scanning microscopes, the sample is displaced horizontally in a grid of positions and measurements are taken sequentially at each location. Low-temperature superconducting quantum interference device (SQUID) sensors and room-temperature magnetic sensors (e.g., Hall-effect, magnetoresistance, magnetoimpedance, magnetic tunnel junction (MTJ) sensors) are typically kept at a fixed position to reduce vibration issues and avoid picking up variations in the background field (Egli & Heller, 2000; Fong et al., 2005; Gruhl et al., 2001; Hankard et al., 2009; Kawai et al., 2016; Kletetschka et al., 2013; Lima et al., 2014; Uehara & Nakamura, 2007). The first allow for very high field sensitivity at the expense of spatial resolution owing to cryogenic constraints required to keep the sensor at very low temperatures while measuring samples maintained at room temperature; the latter have increased spatial resolution but reduced field sensitivity, in part due to a much higher sensor operating temperature and associated increase in sensor noise.

Imaging microscopes typically use digital cameras to capture fluorescence or reflected/transmitted light that is affected by the sample's magnetic field via a diamond chip with nitrogen-vacancy centers [quantum diamond microscopy (QDM)] or via a garnet film [magneto-optical imaging (MOI)] (Bobyl et al., 2007; Glenn et al., 2017; Uehara et al., 2010). Both transducer and sample are kept stationary and all measurements at different locations within the field of view are captured simultaneously. Samples are only displaced to capture different fields

**Table 1**
*Comparison of General Characteristics of the Two Categories of Magnetic Microscopes*

| | Scanning microscopes | Imaging microscopes |
|---|---|---|
| Spatial resolution | >5 μm (RT sensors)<br>>100 μm (SC sensors) | >5 μm |
| Step size/pixel size | >1 μm | >1 μm |
| Mapping area/field of view | <2,500 $mm^2$ | <15 $mm^2$ |
| Sensor-to-sample distance | >5 μm (RT sensors)<br>>100 μm (SC sensors) | >1 μm |
| Noise floor | >1 μT (MTJ)<br>>10 pT (SQUID) | >10 nT (QDM)<br>>100 μT (MOI) |
| Bias field | No[a] | No (MOI); Yes (QDM, <1 mT) |
| Measured field components | Single (typically $B_Z$[b]) | MOI: Single ($B_Z$)<br>QDM: Vector ($\vec{B}$ projected along each of the four <111> crystallographic directions); Single ($\vec{B}$ projected along a single <111> direction) |
| Optical registration | Indirect | Direct |

*Note*. MTJ, magnetic tunnel junction; RT, room temperature; SC, superconducting.
[a]Some magnetic sensors placed at very close proximity to the sample (e.g., <30 μm) may interfere with its magnetization in some situations owing to features like flux focusers and magnetic fields produced by sensor bias currents. [b]The field component normal to the sample's top surface ($B_Z$, in our axis orientation convention) exhibits rotational invariance and does not change with the relative orientation of the sensor with respect to the sample, except for a possible rotation of the field map. Other field components do not exhibit this property and the maps will be different depending on the relative orientation. This complicates interpretation and requires careful registration of the orientation of the sensor with respect to the sample, which is more readily obtained in imaging systems.

**Table 2**
*Synthetic Sources Used in the Characterization of the Performance of the Net Moment Estimation Technique*

| Test magnetization | # Source elements | Description | Net moment |
|---|---|---|---|
| Source A | 2 | Dipole 1: $m_1 = 1.0 \times 10^{-11}$ $Am^2$, $i_1 = -20°$, $d_1 = 20°$<br>Dipole 2: $m_2 = 1.0 \times 10^{-11}$ $Am^2$, $i_1 = 0°$, $d_1 = 305°$<br>Relative displacement: $\Delta x = 30\ \mu m$, $\Delta y = 12\ \mu m$ | $m = 1.577 \times 10^{-11}$ $Am^2$<br>$i = -12.5°$, $d = 341°$ |
| Source B | 2 | Dipole 1: $m_1 = 1.0 \times 10^{-11}$ $Am^2$, $i_1 = -20°$, $d_1 = 20°$<br>Dipole 2: $m_2 = 1.0 \times 10^{-11}$ $Am^2$, $i_1 = 0°$, $d_1 = 305°$<br>Relative displacement: $\Delta z = 30\ \mu m$ | $m = 1.577 \times 10^{-11}$ $Am^2$<br>$i = -12.5°$, $d = 341°$ |
| Source C | 1 | Uniformly magnetized thin square slab (50 μm × 50 μm × 0 μm) | $m = 1.0 \times 10^{-11}$ $Am^2$<br>$i = -45°$, $d = 20°$ |
| Source D | 1 | Single magnetic dipole | $m = 1.0 \times 10^{-11}$ $Am^2$<br>$i = 30°$, $d = 285°$ |
| Source E | 2,000,000 | Distribution of 2 million dipoles with identical magnitudes ($1.0 \times 10^{-16}$ $Am^2$) and random directions within a 100 μm cubic volume. Magnetization efficiency of 1.5% along the direction $i = -12.6°$, $d = 333.4°$ | $m = 1.56 \times 10^{-12}$ $Am^2$<br>$i = -14.0°$, $d = 334.9°$ |
| Source F | 2,000,000 | Distribution of 2 million dipoles with identical magnitude ($1.0 \times 10^{-16}$ $Am^2$) and random directions within a 100 μm cubic volume. Magnetization efficiency of 0%, corresponding to a fully demagnetized state | $m = 1.32 \times 10^{-13}$ $Am^2$<br>$i = -36.0°$, $d = 180.4°$ |

*Note*. The symbols $m$, $i$, $d$ stand for the strength, inclination, and declination of the test source's net moment. For samples composed of two dipoles, the index is associated with the moment of each dipole, and $\Delta x$, $\Delta y$, and $\Delta z$, represent the displacement between the two dipoles in the $x$, $y$, and $z$ directions, respectively.

of view for an enlarged mapping area or to analyze different regions of the sample. Imaging systems allow for near-perfect registration with optical images of the sample, as the same camera and objective are used for magnetic imaging and optical imaging.

In both categories, the magnetic sensors/transducers are brought into very close proximity to the geological sample's top surface to maximize both spatial resolution and magnetization/moment sensitivity. Estimating the distance between the sensor and the top surface of the sample is often useful to provide lower limits for the $z$ coordinate of the source model/measurement plane and to constrain solutions to physically meaningful regions when applicable. This can be accomplished by using either magnetic or optical techniques. In the first case, mapping the field along horizontal lines perpendicular to a long thin current-carrying wire can provide a good estimate of this distance, as the separation between the observed peaks in the field is approximately twice the sensor-to-sample distance (Baudenbacher et al., 2003; T. S. Lee, et al., 1997). Alternatively, the full width at half maximum of the single-peak field produced by a very small magnetic source that is magnetized into/out of the sample plane can be used to provide an estimate for the sample-to-sensor distance (Lima et al., 2014). In the second case, optical distance measurement techniques, such as focal depth and interferometry, can be used to estimate the sensor-to-sample distance (Berkovic & Shafir, 2012).

Lastly, for some instrument configurations it may be necessary to model the finite size of the sensing area/volume of magnetic sensors, either by deconvolving the measured data or by incorporating integration/averaging effects associated with a finite sensor size into the modeling. We refer the reader to some of the literature discussing this issue (Egli & Heller, 2000; Lima & Weiss, 2016; Lima, et al., 1999, 2002; Roth et al., 1989; Tan et al., 1996).

#### 2.3.2. Limitations From Incompleteness of Magnetic Measurements

Attention must be paid to two aspects of the magnetic microscopy measurements that limit the accuracy of net moment estimates: (a) the magnetic field is usually only mapped on a single plane above the top surface of the sample; and (b) the field data are noncontinuous and bounded, as measurements are taken only at discrete points and only over a finite planar area. These factors reveal limitations of magnetic data and trade-off choices that go beyond a particular instrument design.

Unlike a spherical setting, where measurements are taken all around the magnetization of interest, a planar mapping configuration does not directly measure field information from the opposite side of the sample. Instead, it can be shown that such information is spread over large lateral distances from the center of a single-sided map (Baratchart et al., 2017). However, owing to instrumentation constraints, it is usually not realistic to map very large areas with fine step sizes. Not only would this produce very large data sets that require extensive measurement time but also there is no advantage in mapping the sample's field past the region where it drops below the noise floor of the instrument or below background sources such as contamination in the sample mount, the sample holder itself, or temporal variations of the ambient field.

A critical issue in the computations is the stabilization of the $(a/r)^{n+2}$ terms in Equations 6–8, which can rapidly decrease with increasing $n$ depending on the value of $a$. Because $r$ is not a constant on the measurement plane, unlike for spherical data, the choice for the value of $a$ is even more critical. Although the particular choice for $a$ gets canceled out in Equation 15, it can directly impact accuracy when performing calculations using double precision. Thus, we choose $a = h$, where $h$ is the distance between the measurement plane and the origin of the multipole expansion (Figure 1). This ensures that $(h/r)^{n+2} \leq 1$, taming the decay with increasing $n$, where the equality holds right above the origin given that $r \geq h$ by definition and that $1 \leq n \leq N$.

#### 2.3.3. Noise Sources

This study focuses on applications of the multipole technique to SQUID microscopy. However, our multipole fitting technique can be easily adapted and further optimized for data obtained with other magnetic microscopy instrumentation. In this and subsequent sections, noise characteristics, signal-to-noise ratios (SNRs), and sensor-to-sample distances representative of different types of magnetic microscopes are considered.

Any experimental setup for magnetic field detection will introduce imperfections into the measurements. Additive noise and sample contamination are the most common forms of degradation experienced in magnetic microscopy (e.g., Figure S8 in Supporting Information S1). In some scanning microscopes, errors in the positioning of the sample by the sample horizontal translation ($X$-$Y$) stage may lead to a noticeable signal-dependent noise component known as position noise (S. Y. Lee et al., 2004). In fact, the smaller the sensor-to-sample distance, the more critical position noise issues may become owing to the more rapid variations of the field in space.

Here, we only consider sources of additive noise, as position noise is not prevalent in our SQUID microscope and in other systems using high-precision stages whose positioning precision and accuracy are adequate for the sensor-to-sample distances involved. However, this might not be the case for other scanning magnetometer systems and performance of the moment estimation technique can be negatively impacted as a result.

Additive noise is uncorrelated with the field being measured and may be understood as a component that is added to the sample's detected field by the magnetic sensor itself, its read-out electronics, instrument parts, and/or the environment. This type of noise is typically a time-varying signal that becomes spatially distributed in a field map owing to the process of mapping or imaging a sample's magnetic field. Similarly, sample contamination can produce spurious magnetic sources that create magnetic signatures superimposed on the sample's uncontaminated magnetic field. They are usually static in nature and lead to recognizable features in a field map, such as small dipoles (Figure S8a in Supporting Information S1).

Additive noise consists of different components associated with the operation of a magnetic sensor and with electromagnetic fields that may be present in the measurement environment. Flicker noise (also known as $1/f$ noise owing to its spectral decay with frequency, $f$) is ubiquitous in electronic devices and is often the largest instrument noise component found at lower frequencies (<100 Hz). Thermal noise is usually white (i.e., spectral content is constant with frequency) and tends to be visible beyond a "corner frequency" at which the $1/f$ noise drops below the white noise floor level (see, e.g., Figure S8c in Supporting Information S1). Some noise components originating from the readout electronics and the magnetic sensors may be ameliorated by using signal and bias modulation schemes and temperature compensation (Drung & Mück, 2004; Kawai et al., 2016; Koch et al., 1994; Lima et al., 2014; Schöne et al., 1997). Environmental noise is commonly composed of peaks in the spectrum, which are often associated with the fundamental frequency of power lines (60 or 50 Hz depending on the country) and its harmonics. Other sources may also be present in the environment, creating both transient signals (e.g., elevators, vehicles and the subway) and steady signals (e.g., monitors and other pieces of electronic equipment). Environmental noise contamination can be mitigated by operating the instrument inside a shielded chamber or shielded room, which is also critical for minimizing induced magnetization in the sample.

One of the key advantages of magnetic sensors operating at very low temperatures is the substantial decrease in $1/f$ noise and thermal noise (Cantor & Koelle, 2004), leading to corner frequencies below 1 Hz (Figure S8c in Supporting Information S1). This minimizes sensor output low-frequency "drift" and allows for very weak magnetic sources to be successfully mapped, which can be further improved with post-measurement background correction techniques that aim to reduce any residual sensor drift effects observed in the data. Nevertheless, considering that the spectrum of the time-varying magnetic field originating from displacing a geological sample at scanning velocities ranging from 1 to 5 mm/s underneath our SQUID sensor lies predominantly below 20 Hz, there is a large spectral overlap between the $1/f$ component and the signal of interest, particularly for higher sensitivity scales of the SQUID read-out electronics.

Other sources of instrument noise are time-varying signals associated with precision positioners in scanning microscopes and laser excitation/light sources in imaging systems. Lastly, the displacement of a sample holder in scanning microscopes and residual background magnetization of instrument parts may produce perceptible features in a field map when measuring weak samples. However, in properly designed instruments, such noise sources are of secondary importance.

Instrument and environmental noise components in field maps obtained using scanning magnetic microscopy can be somewhat complex, as they are comprised of nonadjacent segments of noise time series stitched side by side in space. Usually, field measurements are not taken during the retrace of the scanning stage between scan lines. This helps prevent spatial misalignment of magnetic data along neighboring scan lines due to unequal flexing of the structures attached to the scanning stage (e.g., pedestal and sample holder) when moving in opposite directions. Therefore, noise characteristics in the scan direction and in the transverse are distinct, with the latter corresponding to a very coarse sampling of the noise time series.

Synthetic Gaussian white noise is frequently used to represent noise contamination in measurements owing to its special mathematical properties (it is a zero-mean stationary and ergodic stochastic process) and the simplicity of generating it on computers. Although this could be an adequate first-order approximation in some applications (e.g., QDM), it is critical to test the technique with actual measured instrument and environmental noise to fully

capture the noise sensitivity of the technique under typical experimental conditions. As we will see in Section 3, the technique performs differently to distinct types of noise, which is expected particularly for more complicated mixed linear-nonlinear inverse problems such as the one studied in this paper.

Sample contamination issues can be critical when measuring weak samples. Spurious sources in the magnetic map will directly influence net moment estimation if they cannot be successfully isolated and removed. Preparing samples in a cleanroom and using carefully chosen nonmagnetic tools, adhesives, and substrates can be quite effective in mitigating this problem, with only a few scattered weak sources remaining. Contamination can be considered a noise source as it may lead to variations in the estimated moments, particularly if its signature changes during stepwise demagnetization and leads to irregular perturbation of the moment estimates. A key advantage of magnetic microscopy techniques is the ability to visualize spurious sources in a particular sample and either exclude them by cropping the field map or identify whether cleaning and remounting are required should the contamination be too close to the rock sample.

As a final note, the vast majority of sensors used in magnetic imaging of geological samples are not absolute sensors. This means that a reference for zero field must be provided. In practice, the sensor's output signal is zeroed in a region of the sample expected to be away from any magnetic sources. Therefore, imperfect zeroing of the sensor's output and amplitude offset introduced by the $1/f$ noise component and other noise components may lead to a spurious offset in the map. Preprocessing of the magnetic data prior to moment estimation can often ameliorate these issues but, as we will discuss in Section 3.4, small residual offsets that could not be fully removed from the maps may still impact the accuracy of the moment estimations and have to be handled by the model.

#### 2.3.4. Sensitivity to Noise

We expect that the higher the noise level in the measurements, the lesser the accuracy of the estimation method. It is critical that the condition number of the matrix $\mathbf{A}$ (i.e., a measure of how much the solution changes for small perturbations in the input data, often calculated as the ratio of the largest to the smallest singular value of $\mathbf{A}$) be not excessively large to ensure reasonable stability of the solution and avoid overamplification of noise present in the magnetic data. The condition number can be improved by choosing a mapping area that extends sufficiently far from the source such that its magnetic field is near zero at the edges of the map [e.g., below a few percent of the peak field value or, for maps with low signal-to-noise ratios, below the noise floor]. The condition number can also be reduced by avoiding sampling the map too finely (e.g., using mapping step sizes that are not significantly smaller than 1/10 of the sensor-to-sample distance). As higher order multipoles are incorporated into the model and the matrix $\mathbf{A}$ grows large, the condition number grows and a regularization strategy may be needed to stabilize the least-squares solution and tame sensitivity to noise.

Singular-value decomposition (SVD) offers a way to both understand the causes of noise amplification and mitigate its effects. In essence, a real $p \times q$ matrix $\mathbf{A}$ can be decomposed as (Golub & Van Loan, 2013; Hansen, 1987)

$$\mathbf{A} = \mathbf{U}\boldsymbol{\Sigma}\mathbf{V}^{\mathbf{T}} = \sum_{i=1}^{p} \mathbf{u_i}\sigma_i\mathbf{v_i^T}, \tag{16}$$

where $\mathbf{U}$ and $\mathbf{V}$ are $p \times p$ and $q \times q$ matrices, respectively, with orthonormal columns (i.e., $\mathbf{U^TU} = \mathbf{I_p}$ and $\mathbf{V^TV} = \mathbf{I_q}$), $\boldsymbol{\Sigma}$ is an $p \times q$ diagonal matrix with nonnegative diagonal elements arranged in nonincreasing order (known as singular values), $\mathbf{u_i}$ and $\mathbf{v_i}$ are denoted the $i$th left singular vector and the $i$th right singular vector, respectively and are the $i$th columns of $\mathbf{U}$ and $\mathbf{V}$, respectively, $\sigma_i$ is the $i$th diagonal element of $\boldsymbol{\Sigma}$, $\mathbf{I_p}$, and $\mathbf{I_q}$ are identity matrices with dimensions $p \times p$ and $q \times q$, respectively, and $^{\mathbf{T}}$ denotes a transpose operation. The pseudo-inverse (or Moore-Penrose) inverse of $\mathbf{A}$, which is denoted $\mathbf{A}^+$, is then given by

$$\mathbf{A}^+ = \mathbf{V}\boldsymbol{\Sigma}^+\mathbf{U}^{\mathbf{T}} = \sum_{i=1}^{p} \mathbf{v_i}\sigma_i^{-1}\mathbf{u_i^T}, \tag{17}$$

$$\text{where } \sigma_i^{-1} = \begin{cases} 0, \text{if } \sigma_i = 0 \\ 1/\sigma_i, \text{otherwise.} \end{cases}$$

The pseudoinverse is a generalization of the inverse matrix, which is only defined for square matrices, and can be used to obtain minimum-norm least-squares solutions to systems of linear equations such as Equation 14. In this case, the solution is given by

$$\mathbf{w} = \mathbf{A}^{+}\mathbf{b} = \sum_{i=1}^{s} \frac{\mathbf{u_i^T b}}{\sigma_i}\mathbf{v_i}, \tag{18}$$

where $s$ represents the number of nonzero singular values. If field measurements are contaminated by additive noise (here denoted $\boldsymbol{\eta}$), we have

$$\tilde{\mathbf{w}} = \mathbf{A}^{+}(\mathbf{b} + \eta) = \sum_{i=1}^{s} \frac{\mathbf{u_i^T b}}{\sigma_i}\mathbf{v_i} + \sum_{i=1}^{s} \frac{\mathbf{u_i^T}\eta}{\sigma_i}\mathbf{v_i} = \mathbf{w} + \mathbf{w}_\eta, \tag{19}$$

which corresponds to the solution for noiseless data ($\mathbf{w}$) with an added component ($\mathbf{w_\eta}$) associated with the noise. The effects of the singular values on the noise can be understood by analyzing the different operations performed in Equation 19: (a) the projection of $\boldsymbol{\eta}$ onto one of the left singular vectors $\mathbf{u_i}$ is calculated; (b) this projection is multiplied by $1/\sigma_i$; (c) the right singular vector $\mathbf{v_i}$ is scaled by the quantity obtained in (b). For very small singular values, this means that small perturbations introduced in the magnetic data by noise may result in large changes to the solution by virtue of the large scaling of the last right singular vectors $\mathbf{v_i}$.

In our moment estimation problem, by definition, the left and right singular vectors associated with non-zero singular values form an orthonormal basis for the measurement subspace (i.e., column space of $\mathbf{A}$) and spherical harmonic coefficient space (i.e., row space of $\mathbf{A}$), respectively. In particular, although the left singular vectors $\mathbf{u_i}$ are orthogonal, they do not directly correspond to single multipole components given that the latter are not orthogonal in the planar setting, as was discussed in Section 1. In fact, the vectors $\mathbf{u_i}$ are associated with linear combinations of multipole components. Thus, net moment information is not concentrated at just three pairs of singular vectors $\mathbf{u_i}$, $\mathbf{v_i}$ but is instead spread across a large number of singular vectors. Whether or not all such vectors are relevant to estimating the net moment in a given situation is directly related to the contribution of a particular $\mathbf{v_i}$ to the net moment (i.e., the magnitude of the first three components of $\mathbf{v_i}$, which correspond to the first three Gauss coefficients representing the dipole term) combined with the (scaled) projection of the magnetic data onto the left singular vectors $\mathbf{u_i}$, $P_i(\mathbf{b}) = \frac{\mathbf{u_i^T b}}{\sigma_i}$, that is part of Equation 19. If that projection is very small and/or if the first three components of that particular $\mathbf{v_i}$ are negligible, then that right singular vector is not relevant to net moment estimation.

As expected in SVD, the higher the index $i$, the higher the oscillations in the singular vectors. In particular, this means that more high-order multipole terms are incorporated into $\mathbf{u_i}$ while at the same time the projection of moderately non-dipolar data $\mathbf{b}$ onto $\mathbf{u_i}$ becomes smaller. If the unscaled projection of the data, $\mathbf{u_i^T b}$, falls faster than the scaling factor $1/\sigma_i$ grows as the index $i$ increases, the net moment estimation approaches (within a prescribed error) the correct value at $i = s_1$, where $s_1 \leq s$. When data are contaminated with noise, it may not be effective to compute the pseudoinverse up to $i = s_1$, depending on the scaled projection of the noise onto the left singular vectors $P_i(\eta) = \frac{\mathbf{u_i^T}\eta}{\sigma_i}$. Such terms may easily become dominant past a certain index $i = s_0$, where $s_0 < s_1 \leq s$, thus negatively impacting the accuracy of the estimates.

Importantly, truncating the SVD at $i = s_0$ is generally not equivalent to truncating the multipole expansion at a corresponding degree, since as discussed above, the singular vectors may be comprised of linear combinations of several multipole components of different orders and degrees. A truncated SVD will instead discard basis elements that lead to excessive noise magnification.

As a final remark, we note that the scaled projection of the noise $P_i(\eta)$ is directly linked to the specific noise being projected onto $\mathbf{u_i}$. Therefore, the performance of the algorithm is affected not just by the SNR but also by the type of noise present in the magnetic data. Moreover, each realization of the random noise will generally yield different projections and lead to some scatter in the estimates, an effect that is more pronounced for maps with lower SNRs.

### 2.4. Regularization Strategies

A discrete ill-posed inverse problem, such as those studied in this paper, will generally not show a large gap in the singular values, exhibiting instead a continuous decay. This makes choosing the cutoff point for discarding singular values and associated singular vectors more complicated: discarding too many singular values will compromise the accuracy of the moment estimates, while discarding too few may yield large variations in the moment estimates that may not seem to converge to a well-defined value. The absence of a large gap in the singular value spectrum suggests a trivial nullspace for matrix **A**, and very large condition numbers lead to instabilities associated with the smallest singular values. Indeed, this is an issue similar to the downward continuation of magnetic fields in the sense that there is overmagnification of noise that does not strictly involve nonuniqueness but instead arises from stability issues. Provided that (a) we have more measurements than unknown coefficients and (b) the magnetic field is adequately sampled on a planar grid above the sample, the least-squares fit of the multipole expansion to the data is generally unique for a given origin location. However, silent sources in the full continuous problem lead to nearly silent sources (i.e., singular vectors with very small singular values) when the degree of the multipole expansion grows in which case the solution of the fitting procedure may be too sensitive to perturbations introduced by noise, as explained in the previous subsection, thus requiring regularization.

Because it takes progressively increasing time to obtain an optimal net moment estimate for higher-degree models for larger maps, regularization strategies that rely on repeatedly solving the inverse problem a large number of times may not be realistic in some cases. In view of those constraints, we chose the following approach: a fixed cutoff point determined by the total number of coefficients in the model, such that all singular values and singular vectors beyond the cutoff index were discarded and not used in solving the linear least-squares problem. We tested other methods such as (a) computing the full SVD expansion and determining the truncation point by capping the condition number, and (b) using standard techniques for solving the least-squares problem that do not involve decomposition truncation, with or without added Tikhonov regularization. However, those did not yield consistent results, which we attribute to the nonlinear part of the inverse problem and the changing nature of matrix **A** resulting from the optimization procedure for picking the origin location.

Specifically, in our regularization strategy, we discard as many singular values as the number of coefficients associated with the last $L_{\mathrm{REG}}$ multipoles in the expansion truncated at degree $N$ while always preserving at least the first three singular vectors/singular values in the SVD to ensure we recover a moment estimate. A multipole of degree $N$ has $2N + 1$ coefficients associated with it. Thus, for $L_{\mathrm{REG}} = 1$ and $N \geq 2$, we discard an equivalent number of singular values; specifically, the last $2N + 1$ singular values and associated singular vectors of matrix **A** are discarded. Similarly, for $L_{\mathrm{REG}} = 2$ and $N \geq 3$, we discard the last $(2N + 1) + [2(N - 1) + 1] = 4N$ singular values and associated singular vectors, which is the same number of coefficients associated with multipoles of degrees $N$ and $N - 1$. More generally, for $N \geq L_{\mathrm{REG}} + 1$, the last $L_{\mathrm{REG}}(2N + 2 - L_{\mathrm{REG}})$ singular values and associated singular vectors are discarded, while for $N \leq L_{\mathrm{REG}}$, all but the first three singular values and associated singular vectors are discarded.

Although this strategy may sometimes yield a slightly sub-optimal cutoff point for the singular values, it has the advantage that it is much faster than other truncation approaches as it does not require scanning through a variety of cutoff candidates. In fact, our tests showed only marginal improvement by choosing the SVD truncation point anywhere between 1 and $s$. This can be explained by the structure of the singular vectors in this problem and the general existence of a series of triplets of singular values associated with the three net moment components, as explained below.

We illustrate all these points with an example using synthetic data (Figure 2). We simulated the field map of a synthetic source distribution (hereafter denoted Source A) comprised of two magnetic dipoles of identical strength and different directions separated by 30 μm in the $x$-direction and by 12 μm in the $y$-direction (see Table 2). The sensor-to-sample distance used was 25 μm. Based on these data, we computed the multipole expansion associated with the optimal solution after fitting for the origin location following the algorithm detailed in Section 2.2. Notice the significant similarity of multipole terms in the planar setting. Specifically, the first three terms of multipoles of order greater than 1 (quadrupole and above) are very similar to dipole components but with different field decays. This is a manifestation of the ill-posedness of the associated inverse problem and illustrates the difficulty in separating the dipole term (i.e., net moment) from contributions from higher order terms. As discussed previously, whereas all those *multipole components* are linearly independent and form a basis for the magnetic field space, they are not orthogonal when restricted to the measurement plane subspace.

On the other hand, the *left singular vectors* $\mathbf{u_i}$ form, by definition, an orthonormal basis for the same magnetic field subspace (Figure 3). While there appears to be some similarities with a few multipole components, detailed comparison of the two figures reveals key differences. First, the initial three left singular vectors (Figure 3, panels 1–3), associated with the largest singular values, are not the dipole components (cf. Figure 2b); instead, they appear similar to the first three components of a multipole of order between 4 and 7 (cf. Figures 2d and 2e), although not quite exactly because otherwise they would not contribute to the net moment. Second, the corresponding right singular vectors $\mathbf{v_i}$ have significant dipole terms (i.e., first three coefficients of each singular vector as shown in Figure 4a, ordered according to non-increasing singular values shown in Figure 4b). Third, in fact many other right singular vectors (typically in triplets, but not necessarily grouped consecutively as in this example) contribute significantly to each of the dipole components. This is perhaps best seen by computing the Euclidean norm of the dipole components for each $\mathbf{v_i}$ (Figure 4c). It can be observed that higher right singular vectors actually have larger dipole norms than lower ones. In this example, the ratio between the norms of the 64th and 1st, 65th and 2nd, and 66th and 3rd singular vectors range between 3.0 and 4.7. However, because the $\mathbf{v_i}'$s are scaled by the reciprocal of the corresponding singular values, we observe a fast increase (power law) in the contribution of higher order terms to the net moment. The same ratios computed with scaled right singular values range from 200 to 430! That means that any noise component with non-negligible projection onto the highest left singular vectors $\mathbf{u_i}$ will lead to significant contributions to the net moment, potentially compromising the accuracy of the estimate. Thus, it is critical to tame the scaling of the highest-order right singular vectors that contribute to the net moment. That is the goal of introducing a regularization scheme (Figure S1 in Supporting Information S1 illustrates how varying the regularization parameter $L_{\mathrm{REG}}$ affects the model and its ability to reproduce the field map data, which is traded off for stabilizing the net moment estimates and improving accuracy in the presence of noise).

Notice that the incorporation of regularization only entails relatively minor changes to the basic algorithm described in Section 2. Specifically, step (3.a.2) involves solving the linear least-squares problem using a pseudoinverse based on the truncated SVD associated with a prescribed $L_{\mathrm{REG}}$, which is typically chosen in advance depending on the SNR and noise characteristics of the magnetic data being analyzed. In addition, step (5) may require the use of auxiliary metrics to help pick out the optimal solution as the range of model degrees producing stable estimates can become quite narrow at higher noise levels.

The greater complexity in regularizing this particular inverse problem stems from the fact that it is a mixed linear-nonlinear inverse problem in which the regularization factors for the linear part (model degree and SVD truncation point) and nonlinear part (origin location) are not decoupled. As a result, at least two of those factors are operating at any given time and interacting with one another. Nevertheless, we can successfully estimate net magnetic moments, as will be demonstrated in the next two sections. Mixed linear-nonlinear inverse problems are also found in other branches of geophysics (e.g., Fukuda & Johnson, 2010) and generally require more sophisticated regularization.

## 3. Application to Synthetic Data

To test the method and characterize its performance, we used six synthetic magnetizations to generate simulated field maps (Table 2). These maps were then corrupted with prescribed amounts of synthetic additive Gaussian white noise and experimental SQUID microscope noise [the latter is more complex and combines different noise components (Figure S8 in Supporting Information S1 and Section 2.3.3)]. Such data allow us to understand sources of inaccuracies and assess the overall performance of the moment estimation algorithm given that we know the exact magnetic moment of the source distribution. Based on this characterization, we demonstrate the method with experimental data in the next section (Table S2 in Supporting Information S1 summarizes the parameters and algorithms used to obtain the moment data shown in the figures).

Testing the technique with different types of noise, particularly actual instrument noise measured under typical experimental conditions, is critical for assessing the performance of the technique and optimizing it for processing experimental data. In most of our tests, we use a sensor-to-sample distance of 25 μm, which is intermediate between those in SQUID microscopy and those in higher resolution non-cryogenic techniques, such as QDM and MTJ microscopy (see Table 1). The sensor-to-sample distance is, itself, not particularly critical beyond its potential effect on the SNR; instead, the ratio between sample dimensions and sensor-to-sample distance and between mapping area dimensions and sensor-to-sample distance are the key quantities (Figure 1). Multiplying

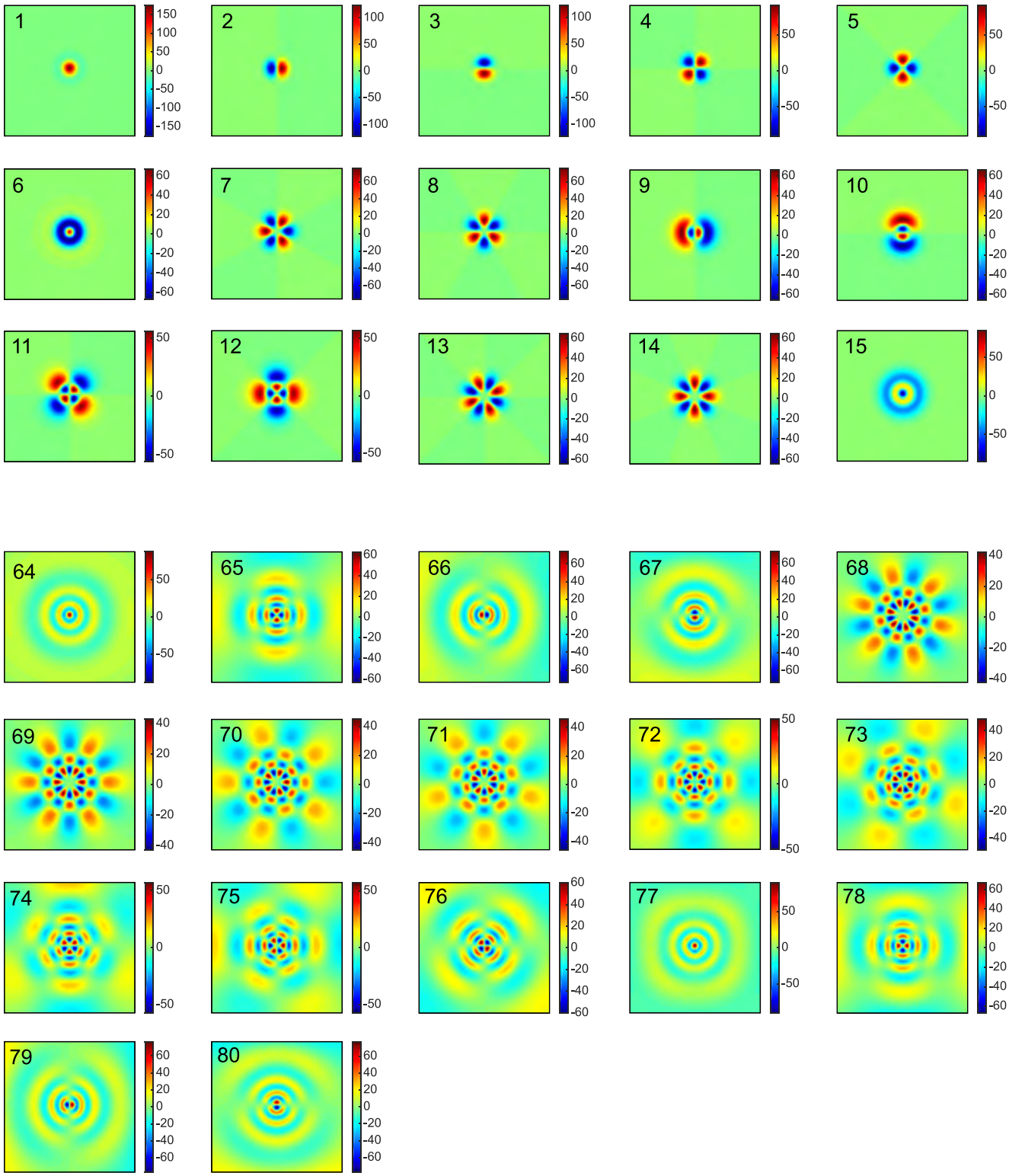


**Figure 3.** Select left singular vectors of a singular-value decomposition (SVD) obtained for the moment estimation of the same field map of Source A shown in Figure 2. Vectors are ordered according to non-increasing corresponding singular values (see Figure 4b). Notice similarities and differences between the left singular vectors and the multipole components shown in Figure 2, with the left singular vectors corresponding to linear combinations of multipole components. Singular vectors shown in arbitrary units, as output by the SVD algorithm.

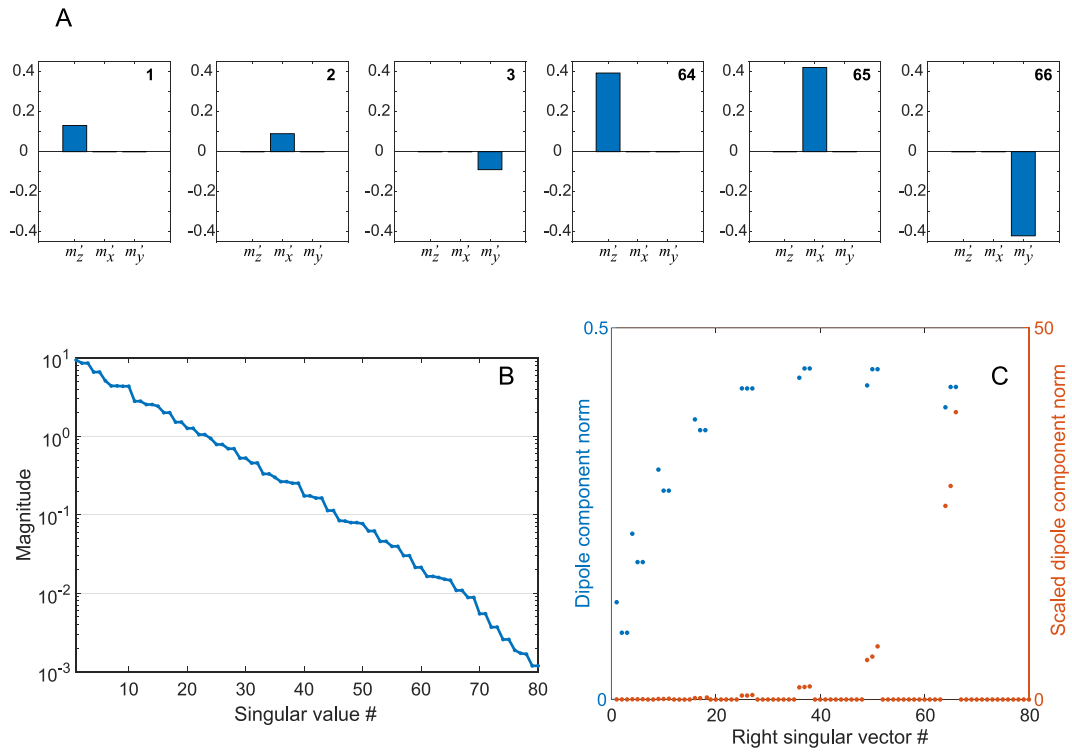


**Figure 4.** Singular values and components of select right singular vectors for the singular-value decomposition used in Figure 3, which was obtained for the same field map of Source A shown in Figure 2. (a) First three components of select right singular vectors $\mathbf{v_i}$, here denoted by $m'_z$, $m'_x$, and $m'_y$. Shown are the components of the 1st, 2nd, 3rd, 64th, 65th, and 66th right singular vectors. (b) Spectrum of singular values showing no clear gap and $\sim 10^4$ decay in magnitude. (c) Norm of the dipole components for each right singular vector, $\left[(m'_z)^2 + (m'_x)^2 + (m'_y)^2\right]^{1/2}$. Norm for unscaled right singular vectors shown in blue and norm for right singular vectors scaled by the reciprocal of the corresponding singular values shown in orange.

all dimensions by a constant essentially does not change the moment estimation problem except for an amplitude scaling factor provided the SNR does not change. Thus, a 10 μm cubic source mapped on a $100 \times 100$ μm$^2$ planar grid 25 μm above this source is similar to a 100 μm cubic source mapped on a $1 \times 1$ mm$^2$ planar grid 250 μm above that source, such that the results can be conveniently scaled up or down.

### 3.1. Noiseless Data

We begin by testing the method with noiseless data. No regularization is introduced, as it is not necessary to stabilize the moment estimation process. This also allows us to understand the impact on accuracy of subsequently incorporating our regularization scheme into the inverse problem. We begin our analysis with Source A (see Section 2.4, Table 2, and Figures 2–4). We quantify the percent error in the estimation of the net moment by vector-subtracting the true magnetic moment, $\vec{m}$, from the moment estimate, $\vec{\tilde{m}}$, and subsequently normalizing the magnitude of this difference by the magnitude of the true magnetic moment:

$$\varepsilon_m = \frac{|\vec{\tilde{m}} - \vec{m}|}{|\vec{m}|} \times 100\% \,. \tag{20}$$

This error metric has the advantage of quantifying discrepancies in both magnitude and direction and corresponds to the (normalized) distance between the estimate vector and the true moment vector. Notice that, in practice, this metric cannot be computed for experimental data as the true magnetic moment is unknown and is, in fact, the vector quantity we seek to estimate as accurately as possible from the magnetic data. Discrepancies between the model field map, $\tilde{b}$, and the true field map, $b$, are quantified by means of normalized residuals:

$$\hat{\varepsilon} = \sqrt{\sum_{k=1}^{K} \left(\tilde{b}_k - b_k\right)^2} \Big/ \sqrt{\sum_{k=1}^{K} b_k^2} \,. \tag{21}$$

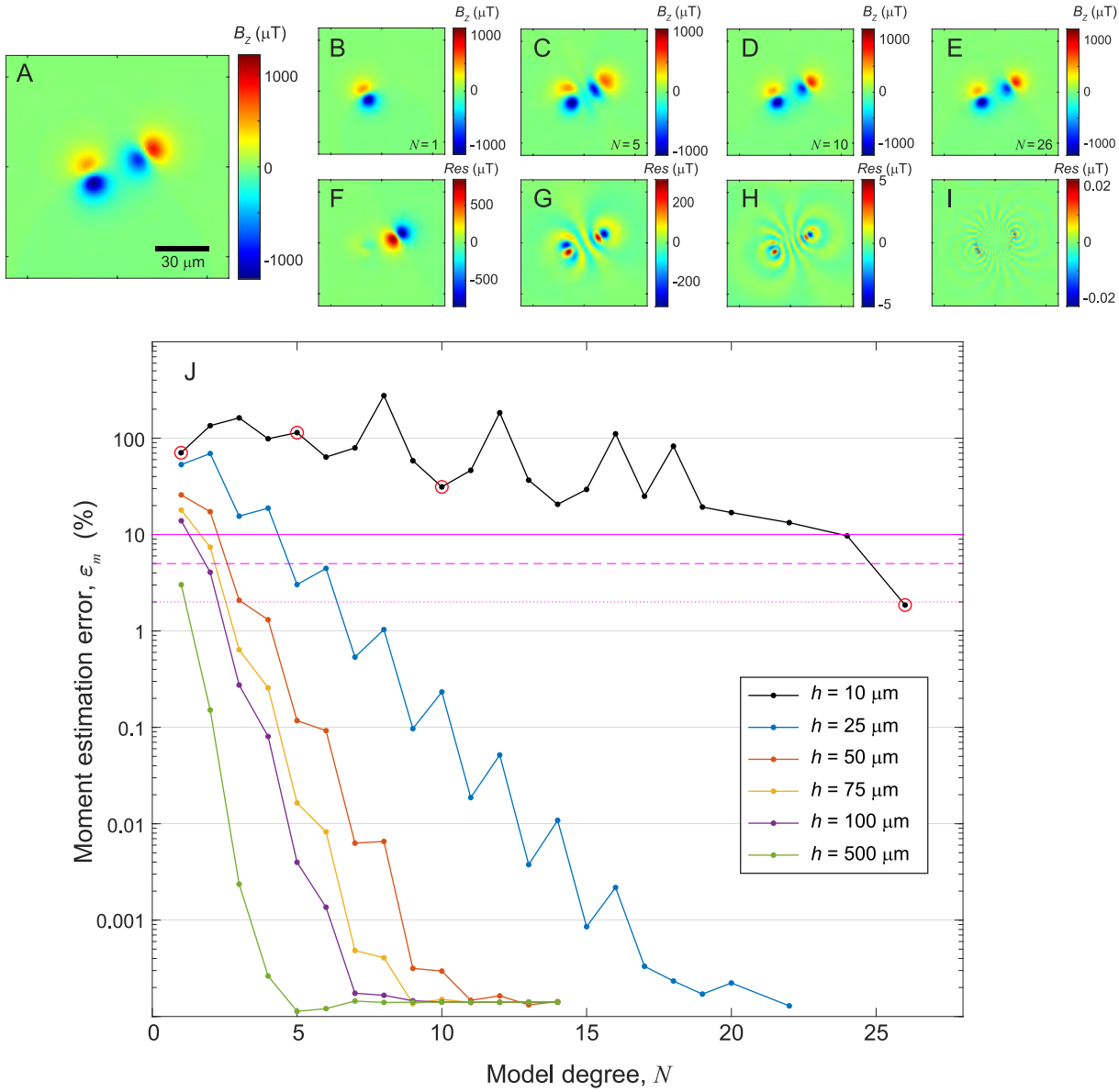


**Figure 5.** Net moment estimation results for Source A (noiseless case) with varying multipole model degree using simulated field maps at different sensor-to-sample distances. (a) Simulated $B_z$ field map for a sensor-to-sample distance of 10 μm. See Figure 2 for a simulated field map corresponding to a sensor-to-sample distance of 25 μm. (b–e) Model field for select model degrees [1 (dipole), 5, 10, 26, respectively]. (f–i) Difference (residuals) between the model field maps (b–e) and the original field map shown in (a). (j) Net moment estimation error as a function of model degree for different sensor-to-sample distances. Solid, dashed, and dotted magenta lines represent 10%, 5%, and 2% thresholds for the moment estimation error, respectively. Red outline circles indicate moment estimation errors corresponding to select model degrees for the maps shown in (b–e).

By normalizing the residuals, we can readily compare results for different sensor-to-sample distances and different sources.

Results for the noiseless case for Source A with different sensor-to-sample distances are shown in Figure 5. The larger the sensor-to-sample distance, the lesser the contribution from high-order multipoles to the field, which is demonstrated by the faster convergence of the moment estimates in those cases. This stems from the fact that the $(a/r)^{n+2}$ terms in Equation 13 decay faster with increasing $n$ as $r$ grows. Therefore, we observe a decrease in convergence rate as the sensor-to-sample distance is close to or smaller than the distance between the two magnetic dipoles. This is expected given that an increasingly higher number of multipoles is needed to reproduce the fine features present in the map in those cases. We also notice more pronounced oscillations in the error

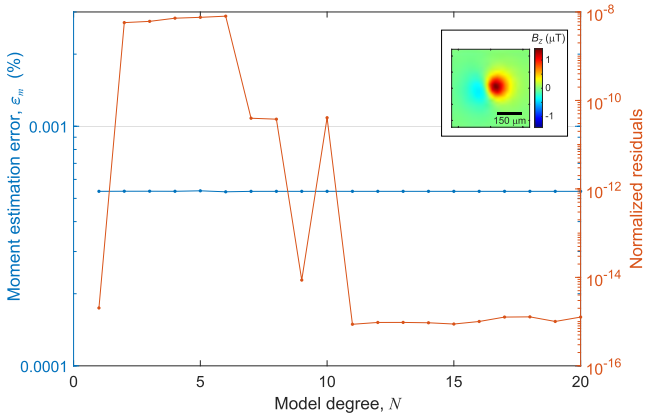


**Figure 6.** Net moment estimation error as a function of model degree for a test source comprised of a single magnetic dipole (Source D, noiseless case). Only one sensor-to-sample distance (100 μm) was tested as results do not depend on that quantity. Moment estimation error shown in blue (left axis) and normalized residuals shown in orange (right axis). Inset: synthetic $B_z$ field map for Source D at a sensor-to-sample distance of 100 μm that was used for these inversions.

curves as the sensor-to-sample distance decreases. Comparable results were observed for Source B [composed of two dipoles with same magnitude and direction as those in Source A but displaced vertically (i.e., in the $z$ direction) instead of horizontally; Figure S2 in Supporting Information S1) and Source C (uniformly magnetized square thin slab; Figure S3 in Supporting Information S1]. Differences in convergence rates are associated with distinct spatial decays due to the particular multipole content of a given source. For instance, Source C decays less rapidly with distance than Source B. Because it consists of a uniformly magnetized extended region instead of a small number of point sources magnetized in different directions, an infinite number of identical point sources are integrated, leading to a slower decay. (For distances that are large compared to the size of the magnetized region, the field decay becomes comparable to that of a dipole, as expected.) However, for a sensor-to-sample distance of 10 μm, Source C converges faster than Source A owing to its comparatively lower multipolar content.

One point that should be emphasized is that this technique will generally not recover the actual sensor-to-sample distance that was used in the mapping of a sample. As discussed in the Introduction and in Section 2, the location of the origin of the multipole expansion cannot be generally constrained by the magnetic data. For a truncated expansion, a certain location will provide the best representation of the measured field by the multipole model. To achieve that, the origin is often placed by the optimization algorithm at a deeper location so as to ensure that the truncated multipole expansion can adequately represent the data. We illustrate this point for Source A (noiseless case) with a nominal sensor-to-sample distance of 25 μm (Figure S4 in Supporting Information S1 and Figure 5).

Next, we test how the algorithm performs for a purely dipolar source while using higher degree models. We are motivated by the fact that the multipole content of a given experimental distribution is not known beforehand, such that it is important to understand whether overfitting can occur that might impact the estimation accuracy. While we expect such effects to be more pronounced when inverting noisy data, tests with noiseless data can reveal fundamental problems that may exist even under the most favorable conditions. Given that the field decay and multipole content of a magnetic dipole do not change with sensor-to-sample distance, we only test the case of a sensor-to-sample distance of 100 μm (Figure 6). We notice that, despite variations in the normalized residuals, the moment estimation error is very low and virtually constant for a range of model degrees. In addition, the residuals highest levels are essentially negligible ($10^{-8}$). This suggests that the method is somewhat robust to the choice of model degree, provided the latter is sufficient to adequately characterize the magnetization.

### 3.2. Noisy Data

We now introduce different amounts of noise contamination into the simulated field maps to characterize its impact on estimation accuracy and test our regularization strategy. We choose Source A with a 25 μm sensor-to-sample distance for these tests as this distance is comparable to the separation of the two dipoles in that test source, leading to a moderately slow convergence of the multipole expansion (see Figure 5). Following Section 2.3.4, we expect that the ability to fit and recover higher order multipoles is directly related to the noise level present in the magnetic data: the higher the noise, the more truncation of the multipole expansion and/or of the SVD is needed to avoid excessive noise magnification, which has a negative impact on net moment estimation.

To simulate spatially distributed sensor noise, we start by adding different levels of Gaussian white noise (with zero mean) to the noiseless field maps to produce prescribed SNRs, where

$$\mathrm{SNR} = 10\log_{10}\left(\frac{P_{\mathrm{signal}}}{P_{\mathrm{noise}}}\right) = 10\log_{10}\left(\frac{\sigma^2_{\mathrm{signal}}}{\sigma^2_{\mathrm{noise}}}\right), \tag{22}$$

and $P_{\mathrm{signal}}$ and $P_{\mathrm{noise}}$ denote the power [i.e., energy per time interval or, equivalently, the square of its root-mean-square (RMS) level] of the signal and the power of the noise, respectively, and $\sigma^2_{\mathrm{signal}}$ and $\sigma^2_{\mathrm{noise}}$ denote

the variance of the signal and the variance of the noise. Although white noise may be a somewhat simplistic noise model for most magnetic sensors (e.g., SQUIDs, MTJs, Hall-effect, GMR/GMI), it is adequate for others (e.g., QDM) and has the advantage of possessing useful mathematical properties, as discussed in Section 2.3.3. Because our signal (i.e., noiseless field map) always has approximately zero mean owing to the properties of magnetic fields of sources with finite dimensions, we use the ratio of variances as a measure of SNR.

SNRs are typically defined in terms of ratios of power given that many signals, such as sinusoids, have infinite energy (i.e., infinite L2 norm) as they are not square integrable over their whole extension. In addition, the definition involves RMS values as those capture the average behavior of the signal within a time interval, whereas amplitude is strictly a quantity defined by just one or two points in the signal depending on the definition used. Notice that an SNR of 10:1, for instance, means that the power of the signal is 10 times greater than that of the noise. In terms of amplitudes, it means the amplitude of the signal is roughly $\sqrt{10} \simeq 3.2$ times greater than that of the noise for sinusoids. Clearly, the relationship between amplitude and RMS value strongly depends on the type of signal/noise under consideration. For instance, white noise can have very large spikes at particular instants/locations due to the statistical nature of Gaussian distributions. A rule-of-thumb factor of 6.6 to convert from RMS to peak-to-peak amplitude is often used for white noise with the caveat that 0.1% of the time the noise level may exceed that amplitude.

We compare (Figure 7) five different SNRs: $\infty$ (noiseless), 100:1, 10:1, 3:1, and 1:1. In our experience, SNRs below 10:1 represent significant amounts of noise contamination, with a SNR of 1:1 representing the practical limit for the detectability of the magnetization's field. Unlike the noiseless case (blue curve in Figure 7j), for which the moment estimation error continues to decay on average with increasing model degree, there is a point in the error curves past which the error levels off or increases, often subsequently displaying larger oscillations (Figure 7j). (No SVD truncation regularization is introduced yet, as we first want to assess how moment estimation accuracy is impacted by noise.) Similarly, the normalized residuals show a slower reduction with increasing model degree past a certain degree (Figure 7k), which corresponds to the situation where correlated features have been removed and residuals continue to decline mostly by the cancellation of noise in the central region of the map. This is best evidenced at very poor SNRs (Figures 7a–7i, inset in Figure 7k). Comparable results for moment estimation error were obtained for Source B (Figure S5 in Supporting Information S1) and Source C (Figure S6 in Supporting Information S1).

Next, we analyze how noise contamination impacts the ability of higher degree models to accurately estimate the magnetic moment of sources with low multipolar content. We add five different noise levels to the field produced by Source D (dipole) and plot curves for moment estimation error as a function of model degree (Figure 8a) and for the normalized residuals error as a function of model degree (Figure 8b). Comparison between Figures 8a and 7j shows a steep rise in moment estimation error with model degree, suggesting that models with increasingly higher order than necessary to accurately model the data do a progressively poorer job of estimating net moment of sources with low multipole content in the presence of noise. This is due to reduced projections of the dipole map onto higher-order left singular vectors. The behavior of normalized residual curves is also different (compare Figures 8b and 7k), with no region of rapid improvement in residuals at lower degrees; instead, residuals steadily decay very slowly owing only to the fitting of noise in the central region by higher order multipoles. Such contrasting behavior indicates that the overall characteristics of residuals decay may be a good indicator of multipole content and help avoid unnecessary computations with higher degree models.

Although these tests reveal important characteristics of the method's performance, we do not have access to the estimation error in practice given that the true net moment is not known. The question then becomes how to pick the optimal model degree that best estimates the net moment of a given magnetic field map. Moreover, can we improve estimation accuracy in light of the theoretical results regarding the regularization of the solutions discussed in Section 2.3.4. It is encouraging that even under contamination with large amounts of white noise, we can achieve, in principle, moment errors below 10% (see purple and green curves in Figure 7j). Still, the accuracy is somewhat below what is achieved by single-dipole fitting of nearly dipolar sources [see (Lima & Weiss, 2016) and initial point of the purple and green curves in Figure 8a]. While this decrease in accuracy is expected as more multipole terms are introduced in the model, proper regularization may often further improve accuracy and reduce scatter in the estimates.

To test the effect of regularization, we take the field map of Source A with an SNR of 3:1 (Figure 9). This represents a very poor SNR that is still above the detection limit (i.e., SNR of 1:1). Compared to the unregularized case

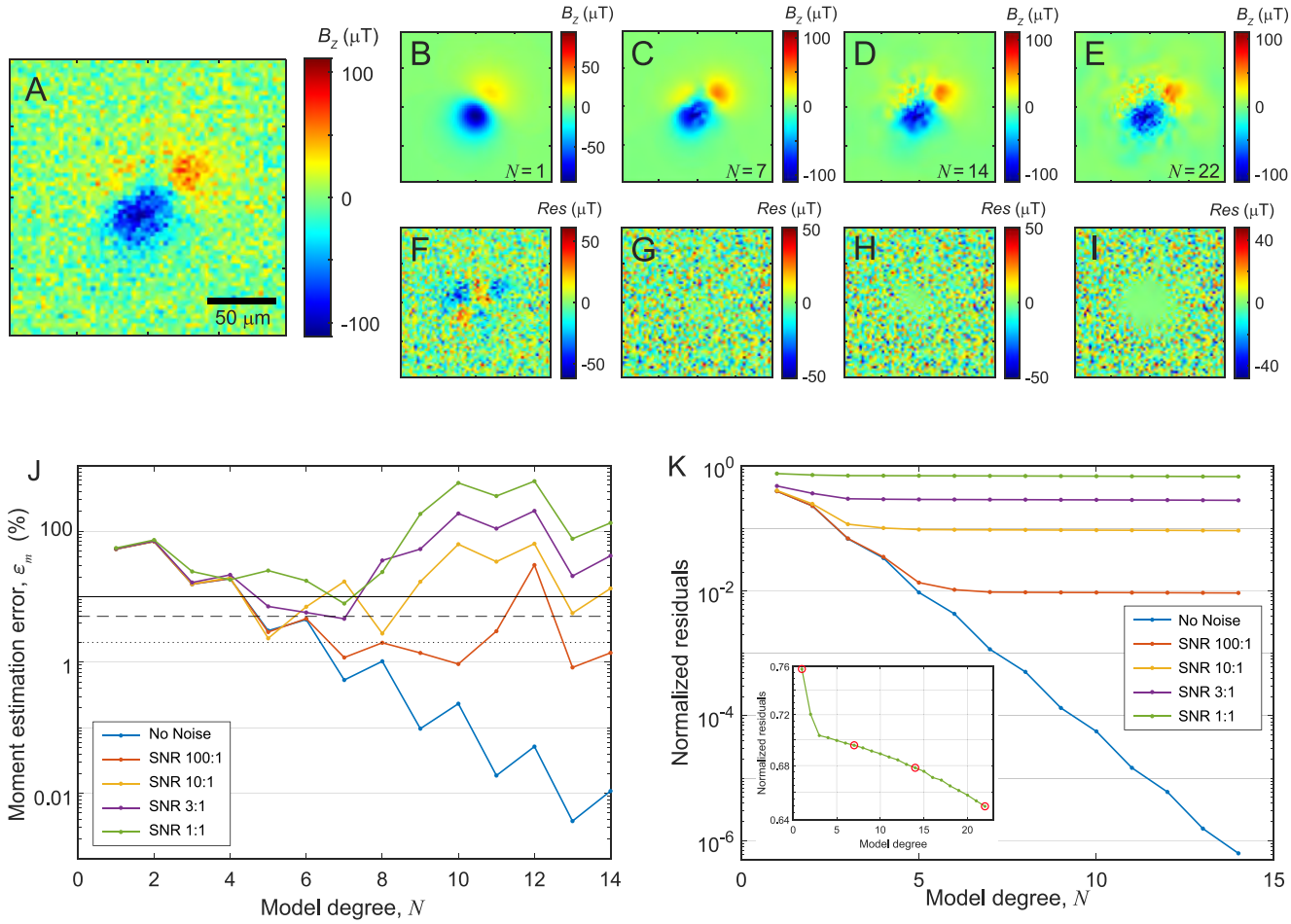


**Figure 7.** Net moment estimation results obtained from synthetic magnetic field maps of Source A corrupted by additive Gaussian white noise. Results are shown for varying model degree and different signal-to-noise ratios (SNRs). (a) Simulated $B_z$ field map for a sensor-to-sample distance of 25 μm and a very poor SNR of 1:1 used for the inversions in (b–k). See Figure 2a for a simulated field map corresponding to the noiseless case. (b–e) Model field for select model degrees [1 (dipole), 7 (minimum estimation error), 14, and 22, respectively]. (f–i) Difference (residuals) between the model field maps (b–e) and the original field map shown in (a). Notice that noise is progressively subtracted from central area of the map for high-degree models owing to overfitting. Moment estimation error (j) and normalized residuals (k) as a function of model degree for 5 different SNRs. Solid, dashed, and dotted black lines in (j) represent 10%, 5%, and 2% thresholds for the estimation error, respectively. Inset in (k) shows a separate view of normalized residuals curve for a SNR of 1:1 (extending to degree 22). Notice that residuals continuously decrease with increasing model degree, albeit more slowly for higher degrees, due to noise cancellation in the central region of the map. Red outline circles indicate normalized residuals corresponding to select model degrees for the maps shown in (b–e).

($L_{\mathrm{REG}} = 0$), there is an improvement in the accuracy by a factor of about 3 when truncating the SVD, bringing it to the 2% threshold or below for these test data.

While it is reassuring that the method can output solutions with low estimation error and tame the pernicious effect of noise on the net moment estimates with added regularization, it leads to the important question of how to select the optimal solution. Specifically, how to choose the best model degree given a fixed SVD truncation. For that, we need to find a proxy for the moment estimation error that can be computed from the properties of the solution and/or the residuals, which are the available data when using experimental field maps. Unfortunately, this is a complicated issue due to the characteristics of this inverse problem. As we explained in Section 2, the model degree is one of the three regularization factors acting on this inverse problem, the other two being the SVD truncation and the location of the origin for the multipole expansion. We tested numerous strategies including the traditional L-curve criterion and various regularization terms (e.g., norm of the dipole coefficients, norm of all recovered multipole coefficients, norm of all multipole coefficients above degree 1, and absolute value of the vertical coordinate of the origin).

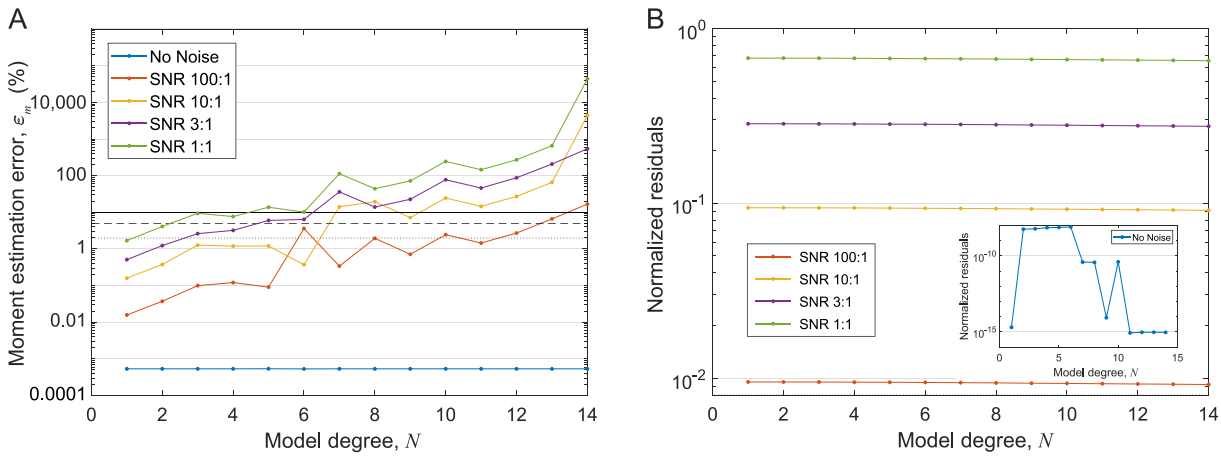


**Figure 8.** Net moment estimation results for Source D (single dipole) with varying model degree for different signal-to-noise ratios (SNRs). Moment estimation error (a) and normalized residuals (b) as a function of model degree for 5 different SNRs. Solid, dashed, and dotted black lines represent 10%, 5%, and 2% thresholds for the estimation error, respectively. Normalized residuals for noiseless magnetic data are shown as an inset in (b) owing to the >8 orders of magnitude difference in residuals magnitude compared to noisy data.

In the L-curve criterion (Hansen & O'Leary, 1993), a plot of the norm of the solution versus the norm of the residuals is constructed for different values of the regularization parameter so as to identify a near-optimal value for the latter (Hansen, 1987). The L-curve's knee indicates the optimal tradeoff between matching of the data (i.e., small residuals) and minimizing the norm (i.e., "size") of the solution. Owing to the concurrent mechanisms associated with these 3 factors and the nonlinear nature of the problem, most of these traditional approaches did not yield consistent results (e.g., L-curve approach using norm of all multipole coefficients as regularization term, as shown in Figure S7 of the Supporting Information S1). To tackle this problem, we need to investigate different types of noise components that may be present in the magnetic data as well as imperfections in the measurement process, such as amplitude offset. We return to this discussion in Section 3.5, once we have considered these other elements and also the idea of using upward continuation for regularization purposes.

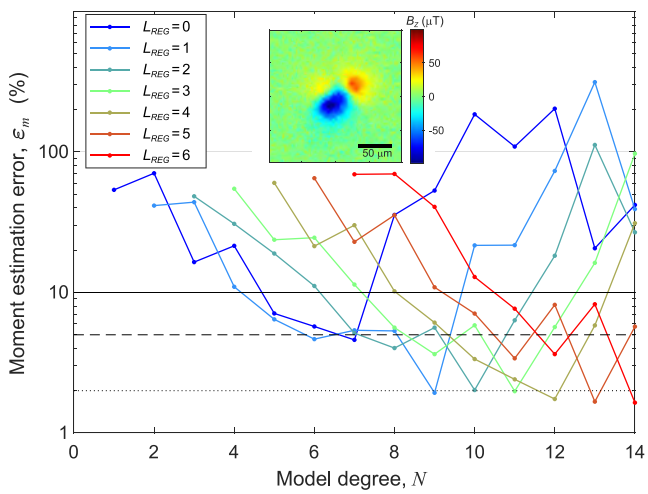


**Figure 9.** Net moment estimation error as a function of model degree for Source A for a sensor-to-sample distance of 25 μm and a SNR of 3:1. Each curve corresponds to a different truncation point for the singular-value decomposition, as determined by the regularization parameter $L_{\mathrm{REG}}$. Note that no regularization is introduced for $L_{\mathrm{REG}} = 0$. Curves start at increasing model degrees for visual clarity, since enough multipole terms are needed in the regularized case in order to add a set number of singular values and singular vectors to the model. Solid, dashed, and dotted black lines represent 10%, 5%, and 2% thresholds for the estimation error, respectively. Inset shows the field map of Source A corrupted with Gaussian white noise, which were the data used in this analysis.

### 3.3. Upward Continuation Strategy for Improving Regularization

One potential strategy for dealing with noise magnification issues in the computation of multipole coefficients is to incorporate upward continuation of field maps prior to net moment estimation. The idea is to spatially low-pass filter the original map to reduce the model degree required to adequately reproduce the magnetic data and estimate net moment. While this has been successfully used in moment estimation with single-dipole models (Fu et al., 2014, 2020), the end result is not so straightforward for multipole models.

First, owing to this significant overlap between the spectrum of spatial noise and the spectrum of the field produced by magnetic sources, basic linear filtering techniques (including upward continuation) are generally unable to separate the noise component from the signal of interest and no clear increase of the SNR may be realized. This means that any improvements introduced by upward continuation are associated with enabling lower degree models to adequately represent the data and not through SNR increase due to noise filtering.

Second, the process of calculating an upward-continued field map, despite being numerically stable, introduces artifacts in the data. Such artifacts will negatively impact the accuracy of net moment estimation even in the absence of noise. Two main causes for this are (a) the finite extent of the mapping area and

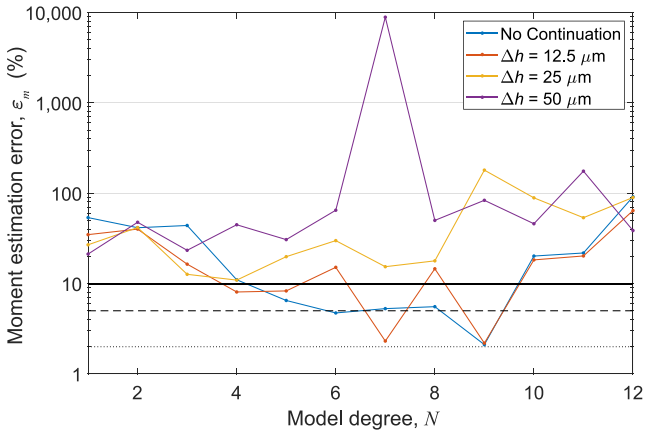


**Figure 10.** Effect of upward continuation of the magnetic data on the moment estimation error for different amounts of continuation. Data correspond to Source A with varying model degree and no singular-value decomposition truncation for a SNR ratio of 3:1 and a sensor-to-sample distance of 25 μm (compare with Figure 9). For typical mapping areas, upward continuing by an amount larger than 1–2x the sensor-to-sample distance yields inferior moment estimates. Notice, however, that the dipole model (degree 1) is generally more robust to upward continuation errors. Its accuracy improves for increasing continuation amounts up to the point where upward continuation errors become large enough and estimation error begins to increase, which typically occurs at 2–4× nominal sensor-to-sample distance.

(b) the discrete spacing of the measurement points. If spatial sampling of the field map is performed adequately, (a) is the predominant source of error in the continued data. It is possible to derive analytical expressions for the error introduced by a finite mapping area and by a finite step size in the upward continuation of a magnetic field map (see Text S1 in Supporting Information S1). Such expressions show how the error grows with the amount of upward continuation and how the magnetic field lying outside the mapping area affects the error. In addition, they show that the error intrudes into the central region of the field map as upward continuation is performed over larger distances.

The combined effect of all these factors on the net moment estimation can be seen in Figure 10. Whereas upward continuation does indeed improve the accuracy of the moment estimations for a single dipole model (i.e., degree 1), it may be less beneficial or even detrimental, particularly when larger amounts of upward continuation are introduced. For magnetizations that are relatively homogeneous, it is generally preferable to use a multipole expansion model with a higher degree than to upward continue the field map (see Figure 10), unless the SNR of the field map is very poor. On the other hand, inhomogeneous magnetizations, particularly in direction, and those whose dimensions are larger than the sensor-to-sample distance may require a high degree multipole model to properly represent their magnetic field maps and to obtain an estimate of the moment with low error, even in the noiseless case.

In such situations, upward continuation of the magnetic field map prior to estimating the moment offers clear advantages (Figure 11). First, we may obtain moment estimates of comparable accuracy at lower multipole model degrees, which is particularly helpful for noisy maps of complex sources. Second, a much smaller amount of continuation is required to achieve low estimation error compared to a dipole model, thus obtaining higher moment estimation accuracy. As can be seen in Figure 11, magnetization distributions in a fully demagnetized state can be particularly challenging to estimate net moment (compare blue and orange traces in Figure 11d and residuals evolution with increasing degree in Figures 11a and 11b). This example also illustrates a common misunderstanding: magnetizations in a demagnetized state (i.e., no coherent alignment of magnetic domains) are often clearly visible in magnetic microscopy maps such that low net moment does not necessarily imply very weak magnetic fields. In fact, in this example, the difference in magnetic field magnitude between a magnetized and demagnetized state is merely a factor of ∼2.

When introducing upward continuation (yellow, purple and green traces in Figure 11d), we observe that the estimation error for upward continued data increases rapidly past a certain degree, where a minimum in the estimation error is realized. The effects of artifacts introduced by continuation into the magnetic map become more dominant once the model is able to account for the main features in the map and noticeable residuals appear near the edges of the residuals map (e.g., model degree 3 in Figure 11c). Further increasing the model degree will result in upward continuation artifacts being modeled (e.g., model degree 10 in Figure 11c), negatively impacting the accuracy of moment estimates. In practice, deciding whether or not upward continuation is needed depends on a visual inspection of the field map to evaluate magnetization inhomogeneity and of the residuals map for solutions obtained with the original magnetic data to determine whether or not a good fit is being realized at moderately low model degrees (e.g., <15). For typical mapping areas used in SQUID microscopy (such as those shown in this paper), which capture most of the field decay, upward continuing the data by an amount greater than one or two times the sensor-to-sample distance may often lead to noticeable inaccuracies in moment estimation, even in the absence of extraneous magnetic sources near the edges of the map.

### 3.4. Offset Sensitivity

When dealing with experimental data, it is important to ensure that there is not a spurious amplitude offset (i.e., additive constant) introduced in the field maps as it can negatively impact moment estimation. Such artifacts, even if small, may be nearly indistinguishable (within the mapping area) from fields due to a deeper source and

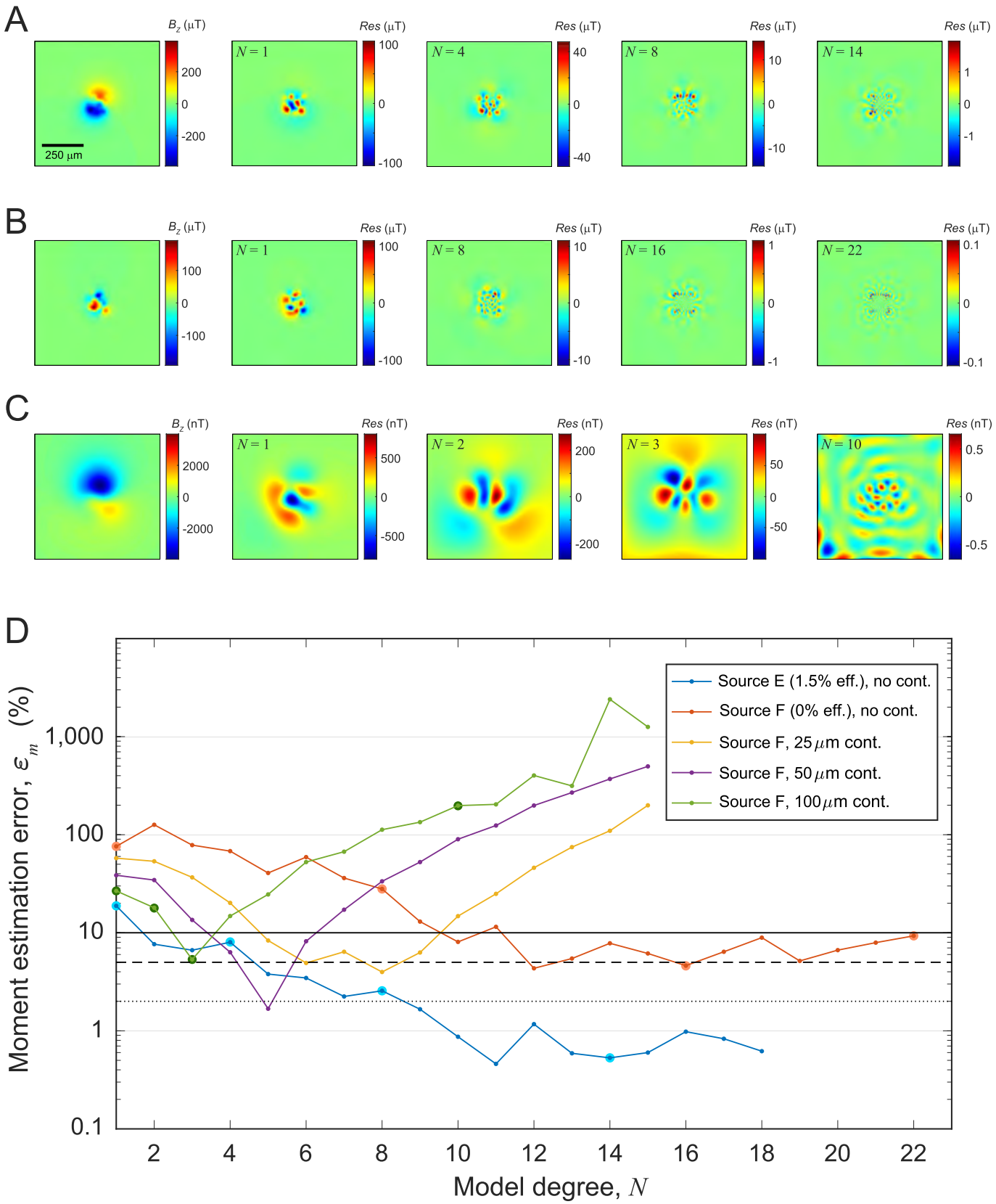


**Figure 11.**

therefore will negatively influence the moment estimation. However, because it is not realistic to expect perfect offset cancellation during the measurement and preprocessing stages, we need to incorporate mechanisms to handle any residual amplitude offset in the magnetic data.

All of our examples so far have involved magnetic data contaminated by Gaussian white noise with zero mean, which may not fully represent the noise components found in many magnetic sensors used in magnetic microscopy, as discussed in Section 2.3.3. The most noticeable manifestation of $1/f$ noise is a low-frequency drift observed on the output sensor, which means that the baseline of the output signal changes as the sample's field is mapped. Whereas such imperfections can be ameliorated by pre-processing the data (e.g., subtracting the average of the first or last few points in each scan line), an effective residual amplitude offset in the magnetic data may persist, particularly when the field map is cropped to analyze a certain feature or to decrease the influence of noise and/or surrounding contamination.

While single-dipole models for net moment estimation are somewhat insensitive to such offsets, multipole expansion models are much more affected by such imperfections owing to the increased number of degrees of freedom for fitting the data, such that moment estimates can easily become dominated by those artifacts. We successfully tackled this issue by introducing a constant term into the multipole expansion and recovering it through the general linear-least squares procedure used to solve Equation 14. Its implementation is somewhat straightforward and involves adding an extra column with 1's to matrix **A** and a corresponding element to the coefficient vector **w,** as seen in Equation 24.

$$B_z(r,\theta,\varphi) = C + \mu_0 \sum_{n=1}^{N} \left(\frac{a}{r}\right)^{n+2} \sum_{m=0}^{n} \left[(n+1)\cos(\theta) P_n^m(\theta) + \sin(\theta)\frac{\partial P_n^m(\theta)}{\partial \theta}\right](g_n^m \cos m\varphi + h_n^m \sin m\varphi), \quad (23)$$

$$\begin{bmatrix} \mathbf{A} & \mathbf{1}_K \end{bmatrix} \begin{bmatrix} \mathbf{w} \\ C \end{bmatrix} = \mathbf{b}. \quad (24)$$

The main drawback of this approach is the change in the structure of matrix **A** and the impact on the singular vectors and singular values stemming from adding a constant term to the multipole expansion. However, we have observed that the main effect is the creation of a first left singular vector that is a constant function, which is then followed by singular vectors very similar to those for the uncompensated case (which are shown in Figure 2). There typically is a noticeable gap in the singular values between the first one, corresponding to the constant left singular vector, and the remaining ones associated with the regular spherical harmonic multipole expansion.

Our numerical experiments involving noiseless magnetic data with added offsets show that the overall performance is only slightly degraded by incorporating this offset compensation scheme (Figures 12a–12c). In particular, significant errors in both magnitude (orange solid line) and direction (green dashed line) are observed when magnetic data have an amplitude offset and moments are estimated without offset compensation (Figure 12d). Notice that the errors are much smaller for the dipole model (degree 1), particularly in direction, illustrating the reduced sensitivity of that model to offset in the data. However, offset compensation can successfully correct the moment estimates obtained by the multipole model in the presence of offset with negligible impact to estimation accuracy (compare blue and yellow solid lines, and light blue and purple dashed lines in Figure 12d). This example highlights the critical importance of offset compensation when processing experimental data.

**Figure 11.** Moment estimation results for Source E and Source F, each comprised of 2,000,000 dipoles of equal intensity randomly distributed in a $100 \times 100 \times 100$ μm$^3$ volume and whose directions were randomly chosen to uniformly sample the unit sphere. Source E has 1.5% magnetization efficiency along a prescribed direction (inclination = −12.6°, declination = 333°), whereas Source F has zero magnetization efficiency (i.e., it is in a fully demagnetized state). Magnetization efficiency represents the degree of alignment of the magnetization in the direction of the applied field. No noise was added to these maps and no singular-value decomposition truncation was used in the inversion. (a) Simulated $B_z$ field map of Source E (left) for a sensor-to-sample distance of 25 μm, followed by residuals for select model degrees. (b) Simulated $B_z$ field map of Source F (left) for a sensor-to-sample distance of 25 μm, followed by residuals for select model degrees. (c) Upward continuation of the map shown in (B, leftmost panel) to yield an effective sensor-to-sample distance of 125 μm, followed by residuals for select model degrees. Notice larger residuals near the map edges due to upward continuation inaccuracies. (d) Moment estimation error as a function of model degree for Source E (blue), and Source F with no upward continuation (orange), with upward continuation of 25 μm (yellow), 50 μm (purple), and 100 μm (green). Colored circles in the blue, orange, and green curves indicate model degrees with corresponding residual maps shown in (a), (b), and (c), respectively. Solid, dashed, and dotted black lines represent 10%, 5%, and 2% thresholds for the estimation error, respectively.

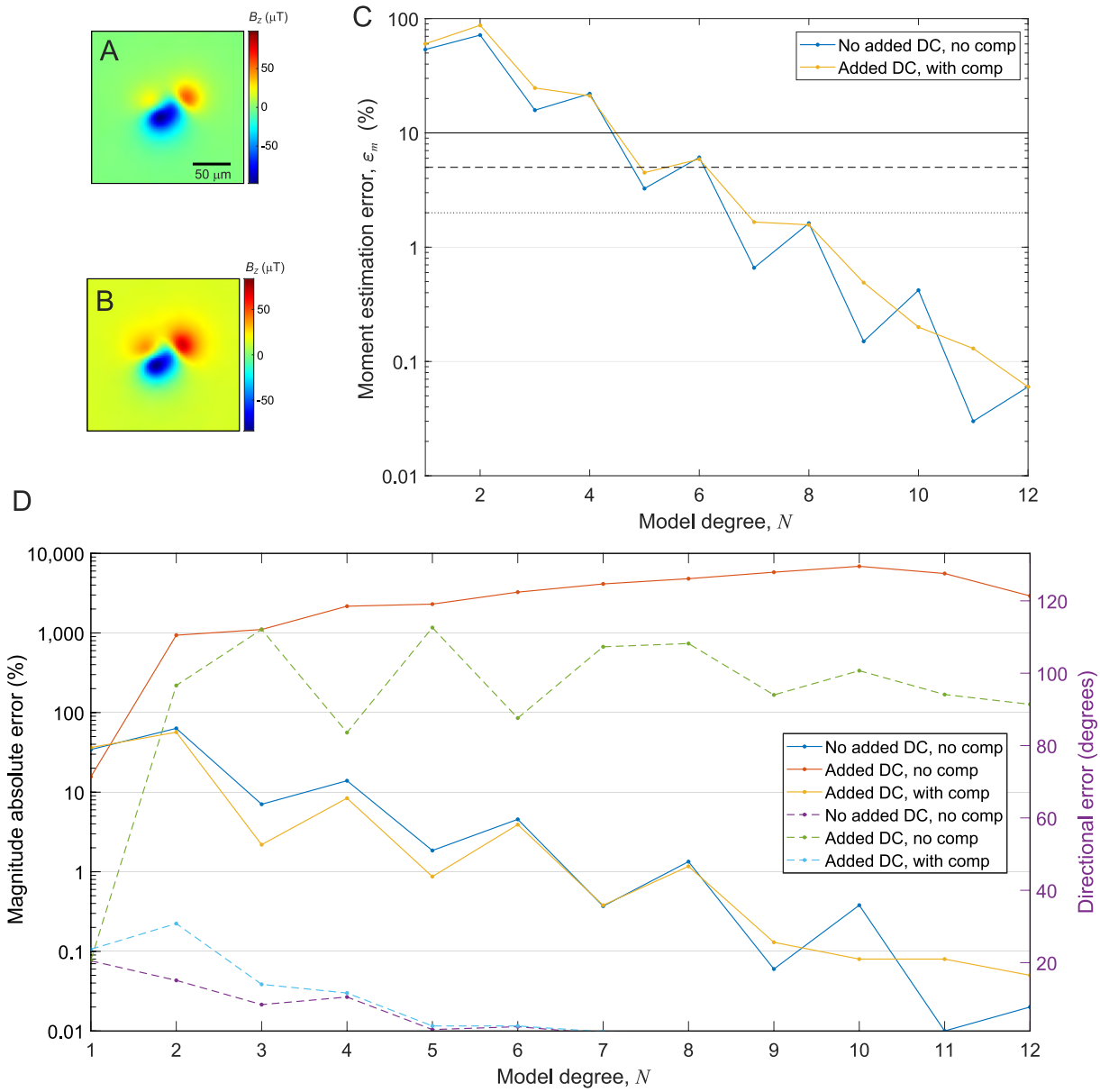


**Figure 12.** Comparison between net moment estimates obtained using models with and without offset compensation (noiseless data, no regularization, offset compensation). (a) Simulated $B_z$ field map of Source A for a sensor-to-sample distance of 25 μm with no added offset (DC). (b) Simulated $B_z$ field map of Source A for a sensor-to-sample distance of 25 μm with an added amplitude offset of +14 μT. (c) Moment estimation error for different model degrees for data shown in (a) using an uncompensated model (blue trace; see Figure 5, noiseless case) and for offset data shown in (b) using a compensated model. Only a slight decrease in accuracy results from introducing offset compensation into the model. Black lines represent 10% (solid), 5% (dashed), and 2% (dotted) error thresholds. (d) Breakdown of the estimation vector error shown in (c) as magnitude absolute error (solid lines) and directional error (dashed lines). Also shown is the case of uncompensated model processing magnetic data with added offset, which results in very large estimation errors (solid orange line, dashed green line). Notice that offset compensation successfully corrects both magnitude and direction estimates, and that the dipole model (degree 1) is noticeably less sensitive to amplitude offset. (Coincidentally, the offset helped improve the estimate moment in this particular case.)

### 3.5. Noisy Data With 1/*f* Component

To properly assess the performance of the moment estimation technique using scanning magnetic microscopy data, we added measured SQUID noise to our synthetic sources. We opted to use real noise measurements given that the simulation of 1/*f* noise is not trivial and may mask some features present in the 1/*f* noise component of our SQUID sensor. In addition, measuring the actual output noise captures all components present in the instrument's output signal and not just the 1/*f* noise.

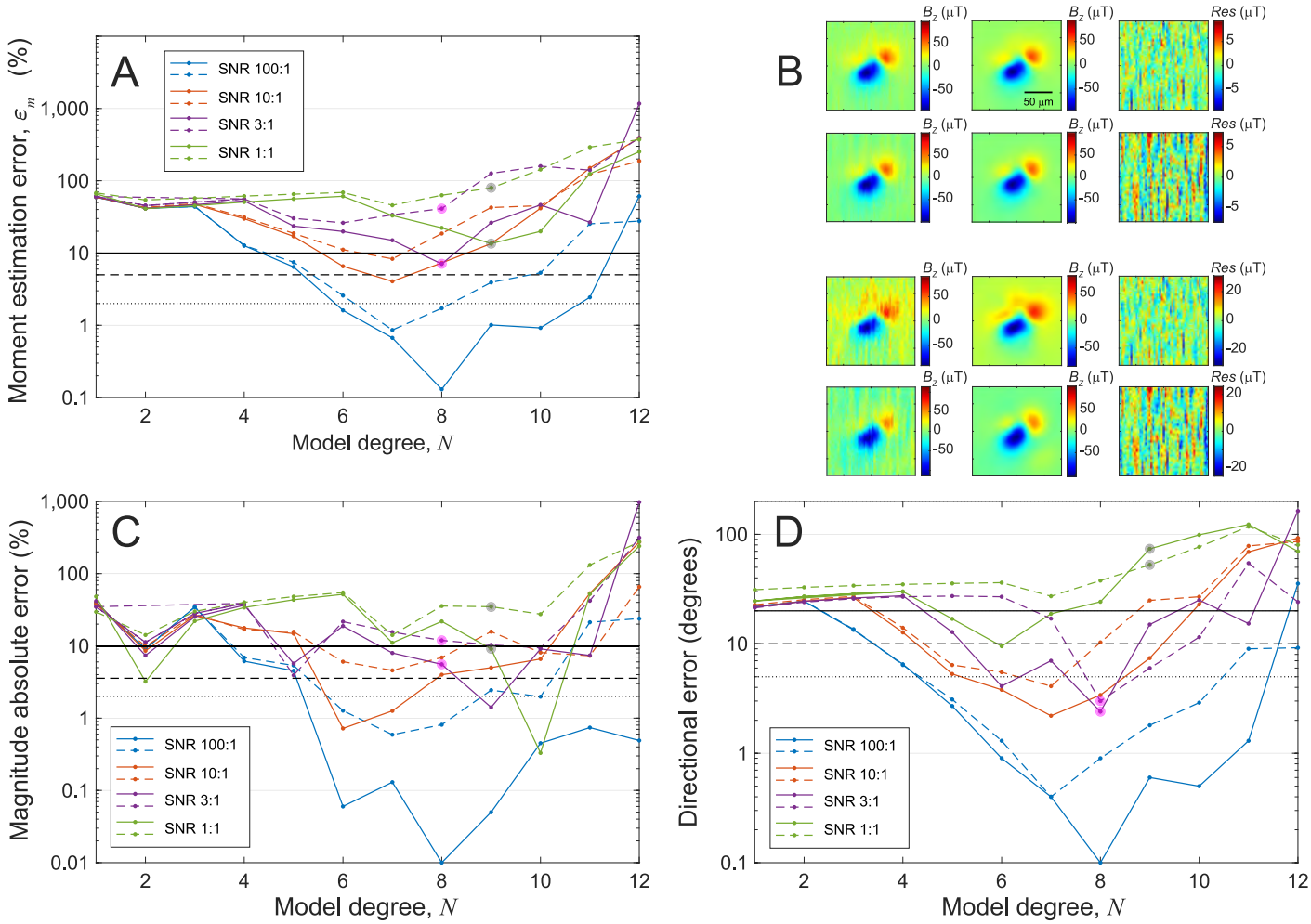


**Figure 13.** Magnetic net moment estimates obtained using offset compensation from simulated magnetic field maps of Source A corrupted by real superconducting quantum interference device (SQUID) microscope noise. (a) Moment estimation error as a function of model degree for two particular noise realizations (solid and dashed lines) and four different SNRs (represented by distinct colors). Variations seen between the results for the two noise realizations represent the typical range of spread observed for a series of repeated maps of the same source. (b) Left column: simulated $B_z$ maps of Source A for a sensor-to-sample distance of 25 μm with added SQUID microscope noise to yield SNRs of 3:1 (top two maps) and 1:1 (bottom two maps). Central column: $B_z$ maps produced by the multipole expansion model at select model degrees (degree 8 for top two maps, degree 9 for bottom 2 maps). Notice the yellowish tinge in the third map from the top, which results from compensating an offset introduced by the noise. Right column: residuals (difference) between synthetic maps (left column) and modeled maps (central column). First and third rows correspond to one noise realization (dashed lines in a, c and d), while second and fourth rows correspond to the other noise realization (solid lines in a, c and d). Pink circles in (a, c and d) highlight results associated with top two rows; gray circles in (a, c and d) highlight results associated with bottom two rows. (c, d) Breakdown of the moment estimation error into magnitude error (c) and directional error (d), following plotting conventions used in (a). Solid, dashed, and dotted black lines represent (a, c) 10%, 5%, and 2% thresholds for the estimation error, respectively; or 20°, 10°, and 5° thresholds for the directional error, respectively.

To test the performance for different noise realizations, we measured a large map of a non-magnetic sample while displacing the scanning stage as in a real mapping procedure with the SQUID readout electronics set to its most sensitive range (Figure S8 in Supporting Information S1). We created different realizations of the SQUID microscope noise by cropping a randomly chosen region of the large noise map that matched the size of the synthetic source map. The amplitude of the map is then scaled to provide the prescribed SNR. We use the inter-quartile range in Equation 22 instead of the variance to better quantify dispersion in actual experimental noise. Note that this procedure does not reproduce exactly the noise observed in a map of a given size, since the gap between adjacent time series segments may be bigger than in an uncropped map of the same size. Nevertheless, such differences are of secondary importance.

Different noise realizations lead to a spread in the recovered moments, as expected due to different projections of the noise component onto the left singular vectors and the stochastic nature of the noise. Figure 13 shows the

moment estimation error for two different SQUID microscope noise realizations, chosen to illustrate the typical spread in moment estimates observed in a set of 10 repeat measurements. Whereas the moment estimation error quantifies the overall discrepancy in estimating the net moment vector, it is instructive to also look separately at the directional error and the magnitude error (absolute value) since these three quantities are non-linearly related to one another, such that the minimum of one quantity may not necessarily correspond to the minimum of the others. Given that $1/f$ noise usually has larger projections onto the left singular vectors and, consequently, a greater impact on estimation accuracy, it may be advantageous to devise other criteria for solution selection that aim to pick the solution with smallest directional error or the one with the smallest magnitude error, whichever may be beneficial depending on the application. We find that even under severe noise contamination (e.g., SNR of 1:1), errors of a few percent may be obtained for some noise realizations. This suggests that additional preprocessing steps of the magnetic data targeting noise reduction may further help decrease the overall spread in the estimates and improve accuracy. Additionally, for maps with very poor SNRs (e.g., below 3:1) it may be worth doing a small series of repeat measurements (∼2–6 maps) and averaging the moment estimates obtained for each map as a way to further improve accuracy and reduce scatter in the estimates stemming from noise (Borlina et al., 2020, 2021).

### 3.6. Solution Selection Criteria

We tested many different strategies for solution selection, but the vast majority of them did not work satisfactorily. Unlike a typical Tikhonov regularization, in which a penalty criterion is introduced to enforce some property of the solution (e.g., minimum norm or maximum smoothness) and a single parameter controls the amount of regularization introduced, the matrix in our linear-least squares problem is constantly changing at each step of the optimization. This makes decoupling the various regularization mechanisms that act in tandem (i.e., model degree, expansion origin, and SVD truncation) somewhat difficult. Given the complexities of mixed linear-nonlinear inverse problems, such as the one investigated in this paper, and the difficulty in devising selection criteria based solely on mathematical theory, we followed a heuristic approach to regularization, as is often the case in such types of inverse problems.

In particular, L-curve plots of the norm of the residuals versus norm of the solution can appear particularly unpredictable, sometimes full of zigzags and with no distinguishable pattern in some cases (Figure S7 in Supporting Information S1), while in others they exhibit their more familiar L-shape. One strategy that proved useful in this case to partially improve the visualization and reduce the occurrence of zigzags in the L-curves consists of sorting the data points such that the curve is plotted with increasing solution norm instead of increasing model degree. Nevertheless, L-curves by themselves did not seem to yield a consistent criterion to choose a solution. Plots of moment versus height, height versus residuals, moment magnitude versus model degree, among others, were similarly unsuccessful in pinpointing with consistency which solution is the optimal solution.

One quantity that appears to lead to robust solution selection is the vector difference between consecutive moment estimates obtained with increasing model degree for a fixed SVD truncation (i.e., a constant $L_{\mathrm{REG}}$). More specifically, the plot of the reciprocal of the norm of the vector difference versus model degree tends to peak around the optimal solution (Figure 14), indicating a somewhat stable solution between two consecutive steps. We chose the reciprocal of the norm as it is much easier to visually detect a peak in a curve than a slight dip, given that the reciprocal emphasizes changes in small values. For high SNRs, the solution tends to stabilize over a larger range of model degrees as noise effects are somewhat subdued. However, for increased noise levels, the solution may quickly stray off the optimal value.

The basic idea is to inspect side-by-side plots corresponding to different SVD truncation factors (typically, $L_{\mathrm{REG}}$ ranging from 0 to 3 or 4) and check which seem to give the best indication of the optimal solution (Figure 14). In general, the greater the SVD truncation, the less rapid the variations the solutions will exhibit with varying model degree. However, care should be taken to not introduce excessive regularization that could impact accuracy. As customary, one should employ the least amount of regularization needed to stabilize the solutions.

It is clear from this example that sometimes multiple peaks may be present in some of those plots. While in general the highest peak corresponds to the optimal solution, this is not necessarily always true and examination

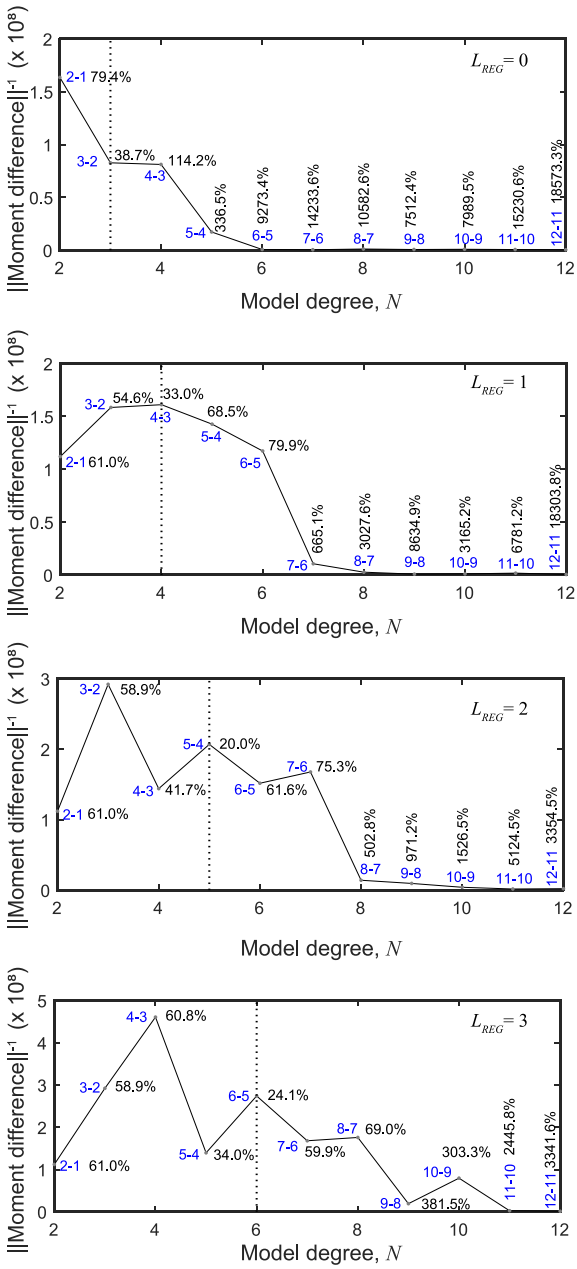


**Figure 14.** Example of plots used in the selection of the optimal solution for different singular-value decomposition truncation factors ranging from $L_{\text{REG}} = 0$ (no regularization, top) to $L_{\text{REG}} = 3$ (higher regularization, bottom). Each plot shows the reciprocal of the norm of the vector difference between moment estimates versus model degree. Numbers in blue indicate the difference computed, while percentages in black indicate the (vector) moment estimation error of the solution with corresponding model degree. The optimal solution (represented by a black dotted vertical line) often corresponds to peaks in such plots, but auxiliary data may be required to resolve ambiguities. Moment estimates computed from a field map of Source A, at a 25 μm sensor-to-sample distance and contaminated with superconducting quantum interference device microscope noise (SNR of 3:1; see map on the top left of Figure 13b).

of auxiliary plots, such as residual maps for features corresponding to underfitting or overfitting, may help pinpoint which one of the peaks corresponds to the optimal solution. In particular, for non-zero $L_{\text{REG}}$, a peak will tend to appear in the lowest model degrees (i.e., $\leq L_{\text{REG}}$), which is associated with an increase in model order without a corresponding increase in the number of recovered coefficients. Additionally, the vector moment difference, by definition, yields one data point less than the number of estimates, and careful inspection of the plot is required to determine whether or not the dipole solution might be the optimal one. A workflow is presented summarizing the various steps involved in the selection of the solution (Figure 15).

## 4. Results With Experimental Data

We further demonstrate the performance of the multipole fitting technique using two sets of experimental data. In both examples, to improve the accuracy of the estimates, raw field maps were pre-processed by mean-subtraction performed on individual scan lines to further reduce residual drift and offset, as discussed in Sections 2.3.3, 3.4, and 3.5. The first set is comprised of a series of maps obtained using the SQUID microscope housed in the Massachusetts Institute of Technology (MIT) Paleomagnetism Laboratory, corresponding to an 8-step alternating-field (AF) demagnetization sequence of two submillimeter basaltic glass impact spherules collected from the Lonar crater, India (Louzada et al., 2008; Weiss et al., 2010). They were first demagnetized to a peak AF field of 145 mT and then imparted a 200 mT isothermal remanent magnetization (IRM) in an arbitrary direction to ensure a near-dipolar individual magnetization. The two spherules were subsequently mounted sufficiently apart (>4 mm) on a nonmagnetic quartz disc to allow for individual mapping of each spherule without interference from the adjacent spherule. The orientation of the spherules was not preserved during the mounting process, such that each spherule carried a magnetization in an arbitrary direction. Although full maps of this sample cannot be adequately inverted using the spherical harmonic multipole expansion model owing to the very high aspect ratio of the source configuration, this arrangement is ideal for experimental validation and performance assessment. By mapping each spherule individually, we are able to obtain independent net moment estimates for each source using our previously developed moment estimation technique based on single-dipole fitting (Lima & Weiss, 2016). Vector addition of the pair of dipole moment estimates at each AF step provides an accurate estimate for the net moment of the overall sample.

To determine the accuracy of the multipole fitting technique using these experimental data, we synthetically brought the two spherules close to each other by adding together cropped versions of the two individual maps. The center of each spherule was determined based on the maximum value of the corresponding total field map, which was calculated from the $B_z$ field map following the procedure described in Lima and Weiss (2009). The $B_z$ map of the first spherule was centered on that source, while the $B_z$ map of the second spherule was centered on a point displaced 80 μm to the left and 80 μm to the top from the center of the second source. This displacement enhanced the multipolar nature of the combined field map, whereas cropping ensured that every data point in the combined field map results from the addition of a corresponding data point in each individual map (Figure S9 in Supporting Information S1).

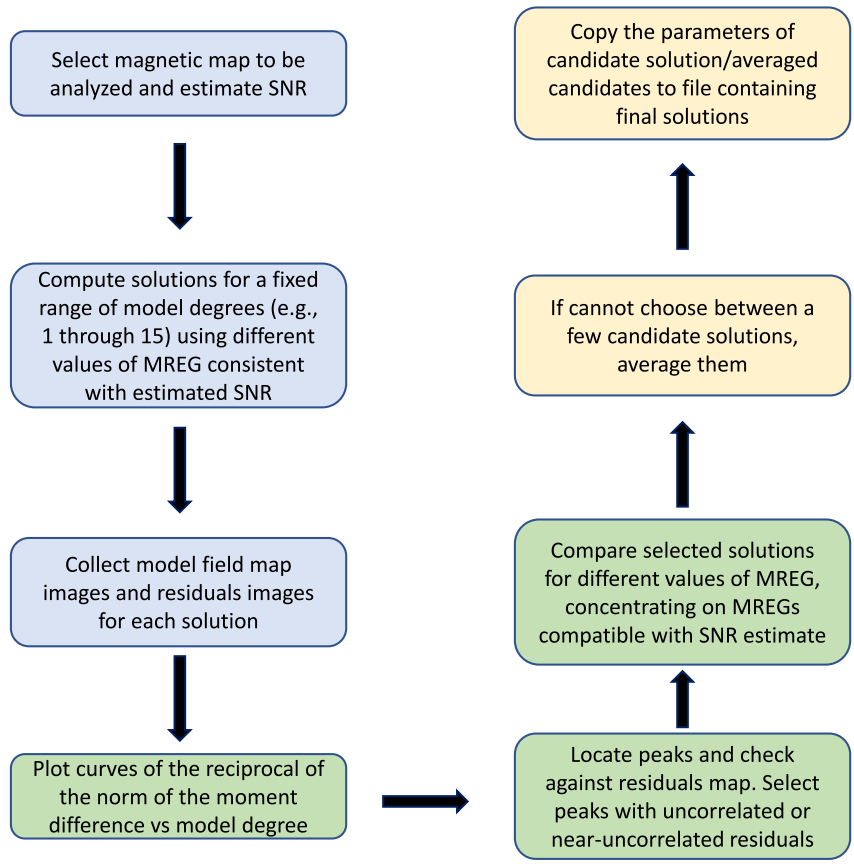


**Figure 15.** Workflow for selecting optimal or near-optimal solutions. Inversion data collection tasks shown in blue, analysis tasks shown in green, and final selection/data output tasks shown in yellow. In case of ambiguity that cannot be resolved by analysis of residuals map and model field map, candidate solutions can be averaged. Predictably, the noisier the magnetic data, the harder it may become to identify an optimal solution. In particular, solutions may approach the true moment and be stable for just one or two model degrees in such cases.

We then applied the multipole fitting technique to estimate the net moment of each combined map capturing both spherules (Figure 16). We tested four regularization factors for each map ($L_{\mathrm{REG}}$ ranging from 0 to 3), computing solutions with models of degree 1 through 15 in each case. Optimal solutions were selected according to the procedure described in Section 3.6. The vector endpoint diagram (Figure 16a) shows the projection of the net moment vector onto two orthogonal planes, while the equal-area plot (Figure 16b) shows an area-preserving projection of unit vectors representing moment direction on a sphere. Both plots show very good agreement between the two sets of independent estimates. Taking the dipole inversions set as the reference, the maximum (absolute) discrepancy in moment magnitude between estimates is −7.8% (AF 100 mT) and the minimum (absolute) discrepancy is +1.2% (AF 40 mT). The maximum angular discrepancy is 3.6° (AF 200 mT) and the minimum angular discrepancy is 0.9° (AF 40 mT). See Table S1 in Supporting Information S1 for tabulated values for each step and for individual dipole inversions of each spherule. We attribute part of the small discrepancy between estimates to the single-dipole inversions, given that the spherules are not perfectly dipolar, and part to the error in the multipole inversions. Considering that the SNR of the field maps in this set is estimated to range from 300:1 (IRM) down to 10:1 (AF 200 mT), the discrepancy between estimates in the first demagnetization steps is unlikely to originate primarily from noise sensitivity issues. The fact that in six of the eight demagnetization steps, the single-dipole model produces higher magnitude estimates seems to suggest uniformly magnetized extended sources that are not perfectly spherical (and thus not perfectly dipolar) as a likely source of the small mismatch in magnitude (Lima & Weiss, 2016).

As typical of regularization strategies for inverse problems, solution selection criteria may have led to slightly sub-optimal picks at some demagnetization steps. The multipole fitting technique did output solutions that were even closer to the combined single-dipole estimates in a few cases. However, those were not chosen because we

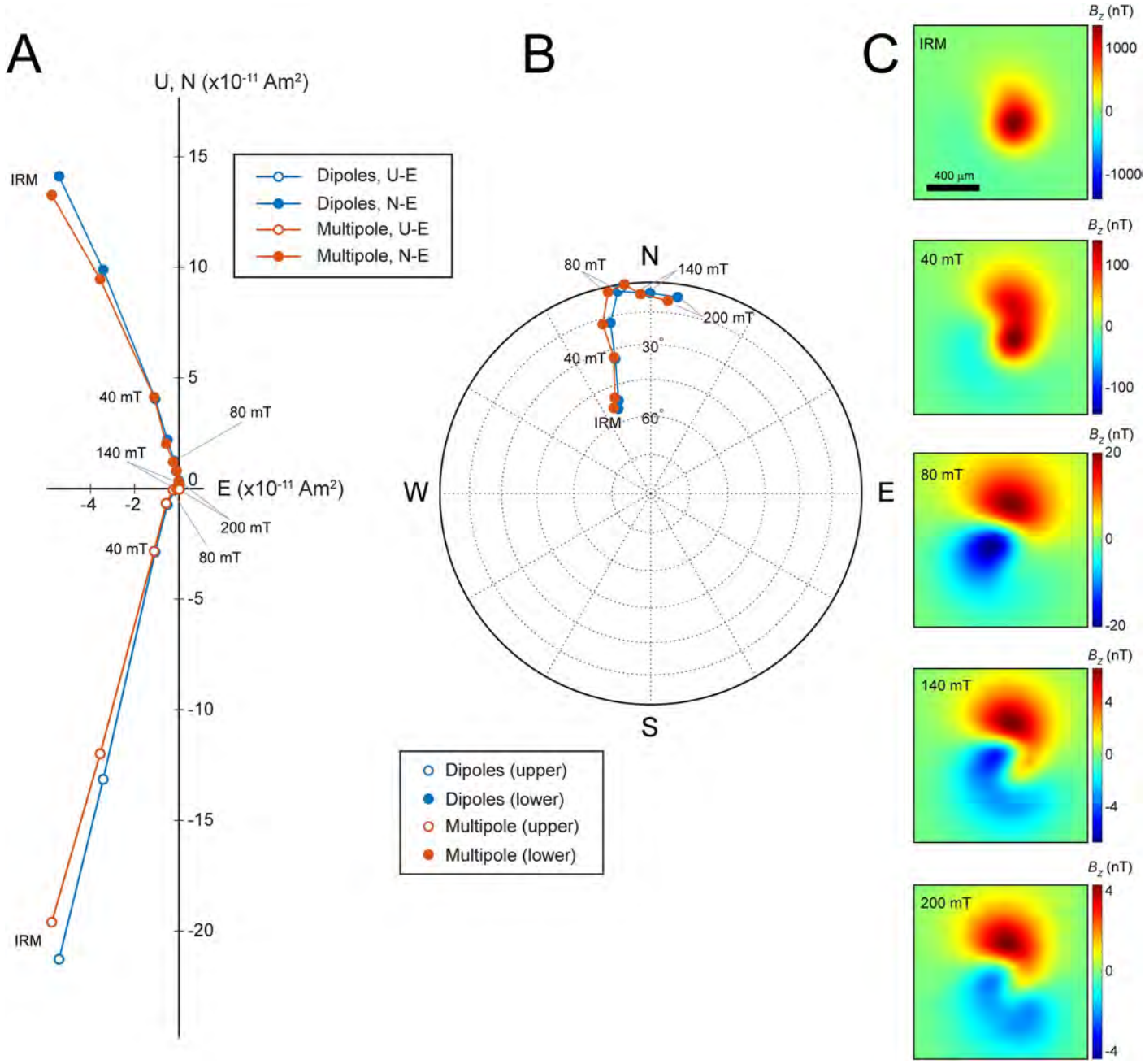


**Figure 16.** Comparison between net moment estimates using the multipole fitting technique and a single-dipole technique for a pair of impact spherules from Lonar crater, India that were imparted a 200 mT isothermal remanent magnetization and progressively demagnetized using alternating fields. The two spherules were mounted adjacent to each other, but sufficiently apart such that they could be individually mapped. (a) Plot of the orthographic projections of the net moment vector obtained by the multipole fitting technique applied to combined individual field maps of each spherule (orange) and by first estimating the moment of each spherule separately with a dipole-fitting technique and subsequently adding the estimates together (blue). (b) Equal-area plot showing the projection of unit vectors on a sphere representing moment directions. Notice the very good agreement between directional estimates obtained with the multipole fitting technique (orange) and with the single-dipole fitting technique (blue). Mismatch in magnitude was smaller than 7.8% and directional mismatch was smaller than 3.6°. (c) Combined $B_z$ maps of the two spherules for select demagnetization steps labeled in (a) and (b). Directional changes of the net moment during the 8-step AF demagnetization sequence [(b) and Table S1 in Supporting Information S1] resulted from the unequal rates of moment loss in the spherules. While the magnetization in Spherule #1 decayed by a total factor of ~220 during AF demagnetization, the magnetization in Spherule #2 decayed by a factor of just ~45, with the latter also exhibiting greater directional stability at higher AF levels than the first. These maps were measured at a sensor-to-sample distance of ~200 μm and were used to compute the multipole fitting inversions shown in orange in (a) and (b). Field data were bilinearly interpolated for visualization purposes only.

wanted to pick solutions without bias stemming from knowledge of independent moment estimates, as would be the case in any paleomagnetic or rock magnetic study. In addition, for the reasons discussed in the previous paragraph, it is not clear that combined single-dipole estimates are necessarily closer, at each demagnetization step, to the true moments than those obtained with multipole fitting. In truth, both set of estimates have errors, but the excellent agreement between them, the results with synthetic data, and previous validation of the single-dipole technique (Lima & Weiss, 2016) strongly suggest that such estimates are quite close to the true net moment.

The second set of experimental data is comprised of magnetic field maps associated with an AF demagnetization sequence of subsamples from two dusty-olivine bearing chondrules from the meteorite Dominion Range (DOM) 08006, a CO carbonaceous chondrite (Figure 17). This analysis was part of a study (Borlina et al., 2021) demonstrating that chondrules carried an ancient magnetization acquired in the solar nebula prior to the accretion of the meteorite's parent body. Those records can constrain the ancient magnetic fields present in the region of the solar nebula where the chondrules were formed. This particular analysis focused on demonstrating two aspects to support the primordial nature of the magnetization: (a) mutually oriented subsamples of the same chondrule should be magnetized in the same direction, and (b) the direction of the magnetization in mutually oriented chondrules should be randomly distributed on the unit sphere. Three of the four chondrules extracted from DOM 08006 were fragmented into two pieces to test whether (a) holds true. For all four chondrules, magnetic field data were obtained using the SQUID microscope magnetometer in the MIT Paleomagnetism Laboratory. Two of those chondrules (DOC 5 and DOC 6) exhibited predominantly multipolar behavior for their smallest subsamples (e.g., Figure 17a), making it difficult to reliably use single-dipole fitting moment estimation in those cases.

The AF demagnetization sequence was realized in 10 mT steps until no further observable decrease in magnetization intensity was detected. For each AF step, the magnetic field of each subsample was measured six times: once after single applications of the AF in the $x$, $y$, and $z$ directions in succession, twice after applications in the $x$ direction, twice after applications in the $y$ direction, and once after an application in the $z$ direction. Moment estimates were then obtained for each magnetic map and all six moments were averaged to reduce the effects of gyroremanent magnetization (GRM) and anhysteretic remanent magnetization (ARM) noise during AF demagnetization. Figure 17a shows the magnetic map of subsample DOC 5A (left) after undergoing the last application of AF in the $z$ direction at the 30 mT AF step, which clearly exhibits multipolar behavior, together with model maps (top row) and residual maps (bottom row) for select model degrees using a regularization factor $L_{\mathrm{REG}}$ of 2. Convergence of the moment estimate for this map was achieved for model degrees above 4 (Figures 17b and 17c). At model degree 7, residuals are essentially uncorrelated (Figure 17a). Further increasing the model degree caused the moment estimate to begin diverging, owing to the effects of noise on the estimates, as discussed in Sections 2.3.4, 3.2, and 3.5. Given the somewhat poor SNRs in those maps (estimated to range from ∼10:1 down to ∼2:1), this was expected to happen for such higher model degrees. Subsample DOC 6A was similarly analyzed, but because the average SNR was lower, we used different values for the regularization factor $L_{\mathrm{REG}}$ (2 and 4) to improve stability and accuracy, depending on the specific map being processed.

Based on these demagnetization data, we constructed a plot of the orthographic projections of the net moment vector and identified a magnetization component in the 0–30 mT AF range using principal component analysis (PCA) (Borlina et al., 2021). After obtaining directional estimates for the components identified in all four subsamples, we compared the directions and associated maximum angular deviations (MADs) using an equal-area plot (Figure 17d). Notice the very good agreement in magnetization direction for the two fragments of each chondrule and also the difference in magnetization direction between the two chondrules. These moment estimates for the multipolar subsamples represent a refinement over the estimates shown in Borlina et al. (2021), which were obtained using upward continuation at an earlier stage of the development of our technique and utilized different solution selection criteria. Note that data in this figure are plotted with the orientation convention used in Borlina et al. (2021) to facilitate comparison. Given the weak magnetization of the chondrules measured in the demagnetization sequences (ranging from $10^{-12}$ to $10^{-13}$ $\mathrm{Am}^2$ for the multipolar subsamples), this analysis relied exclusively on magnetic microscopy and on the ability to accurately estimate net moments from magnetic field maps, illustrating how valuable our net moment estimation technique can be in helping tackle novel science questions.

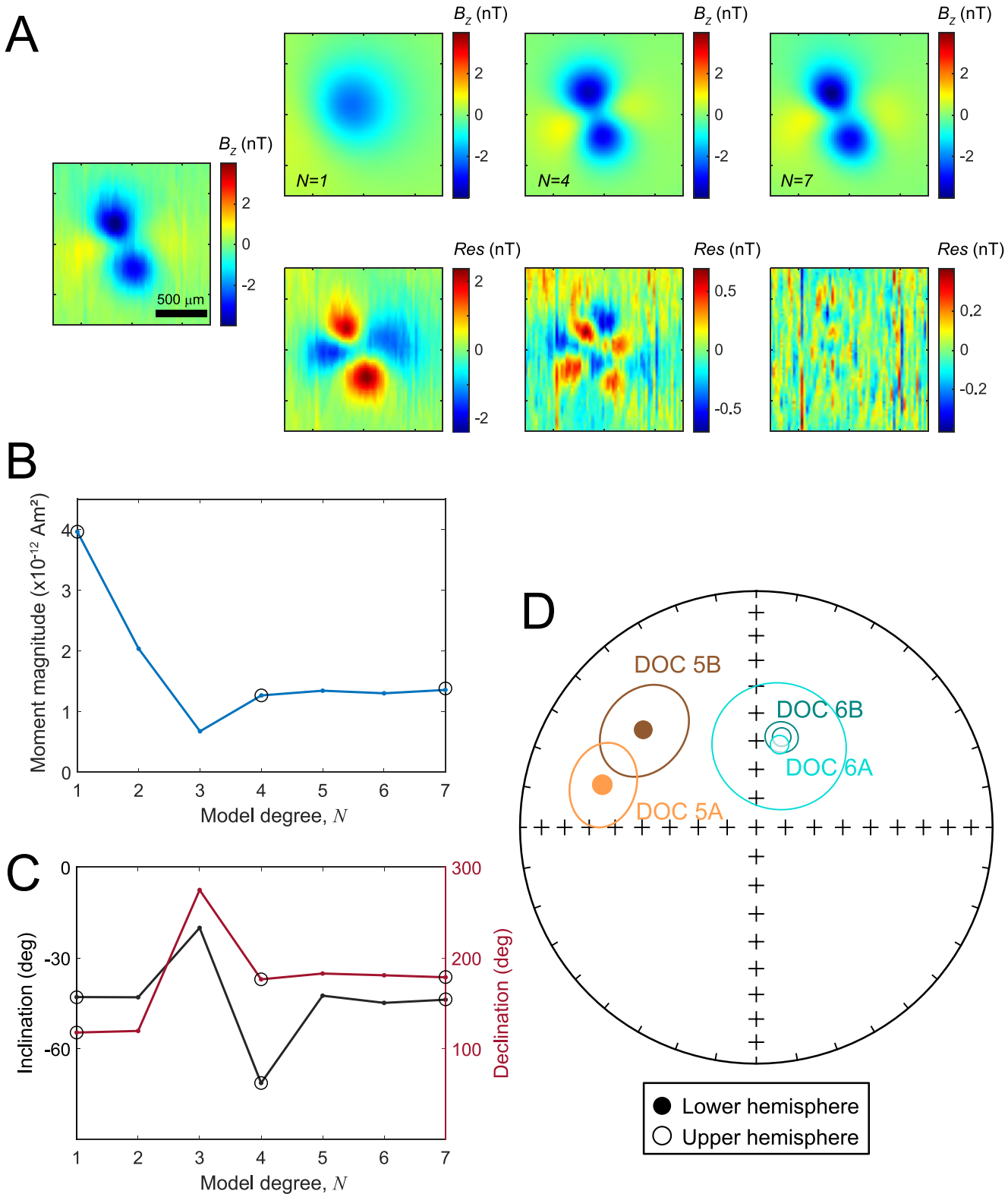


**Figure 17.**

## 5. Conclusions

Moment estimation with multipole fitting greatly expands the category of geological samples suitable for ultra-high sensitivity moment magnetometry analysis. We summarize below the main characteristics and advantages of our multipole fitting technique:

- By increasing the complexity of the source model through spherical harmonic multipole expansions, we can accurately estimate the net moment of complex magnetization patterns even under adverse noise conditions.
- This is particularly critical for very high spatial resolution magnetic microscopes (e.g., the QDM and scanning MTJ microscope) for which maps of isolated features often deviate significantly from that of a magnetic dipole.
- However, indetermination of the origin location for the multipole expansion leads to an intricate mixed linear-nonlinear inverse problem.
- Increasing the degrees of freedom in our model results in higher sensitivity to imperfections in the magnetic data, such as noise and amplitude offsets.
- This increased sensitivity is partly overcome by implementing regularization strategies based on SVD truncation so as to yield satisfactorily accurate solutions while stabilizing the moment estimates.
- Picking an optimal or near-optimal solution among the moment estimates produced by the technique requires judicious analysis of changes in the estimated moments and in residuals as model degrees are increased.
- We have successfully tested the technique with synthetic and experimental data and applied it to novel paleomagnetic studies of terrestrial and extraterrestrial rocks.

Some of the limitations of the technique are as follows:

- Decreased capability for estimating moments of extended sources and sources with high aspect ratios, which may require high model degrees due to the pointwise and symmetric nature of the multipole expansion [each multipole can be interpreted as a discrete set of dipoles at very close proximity (Wikswo & Swinney, 1985)].
- Longer computational times for larger maps ($>100 \times 100$ measurements) and higher degrees ($>15$).
- Higher sensitivity to imperfections in the data, such as noise and amplitude offset, makes it unfeasible to use a high truncation point (e.g., $>12$) of the multipole expansion in some situations. Nevertheless, moment estimates may still be obtained by introducing some amount of upward continuation on the magnetic data (typically by less than 2x the original sensor-to-sample distance).
- Existence of multiple solution candidates in a few situations, requiring careful manual inspection of the results to pick out the most promising one or to average the estimates obtained.

**Figure 17.** Demagnetization data and paleodirectional data for mutually oriented subsamples of two dusty-olivine bearing chondrules (DOC 5 and DOC 6) extracted from CO carbonaceous chondrite meteorite Dominion Range 08006 (Borlina et al., 2021). Each chondrule was fragmented into two pieces (named 5A and 5B, and 6A and 6B) to assess the unidirectionality of its magnetization and all 4 subsamples were measured using the superconducting quantum interference device microscope in the Massachusetts Institute of Technology Paleomagnetism Laboratory while undergoing progressive alternating-field (AF) demagnetization in 10 mT steps. For each AF step, the magnetic field of each subsample was measured six times: once after single applications of the AF in the $x$, $y$, and $z$ directions in succession, twice after applications in the $x$ direction, twice after applications in the $y$ direction, and once after an application in the $z$ direction. The moments associated with each set of 6 maps were then averaged to reduce the effects of spurious gyroremanent magnetization (GRM). Subsamples DOC 5A and DOC 6A were noticeable non-dipolar and were analyzed using our net moment multipole expansion method. Subsamples DOC 5B and DOC 6B were nearly dipolar, allowing for a single-dipole fitting moment estimation method (Lima & Weiss, 2016) to be used. (a) $B_z$ map of multipolar sample DOC 5A (left) after undergoing the last AF application in the $z$ direction at the 30 mT step (~300 μm sensor-to-sample distance). Top row shows the model field maps for select model degrees and bottom row shows the corresponding residual maps in each case. (b) Magnitude (left) and (c) direction (right) of the moment estimates as a function of model degree. Notice the convergence of the estimates past degree 4. Circle outlines indicate degrees for which maps are shown in (a, d) Directions and maximum angular deviations (MADs) for the high-coercivity components identified via principal component analysis (PCA) in the 2 multipolar subsamples (DOC 5A and DOC 6A) and in the 2 dipolar subsamples (DOC 5B and DOC 6B). Notice the very good agreement in direction between subsamples of the same chondrule and also the directional mismatch between chondrules, both supporting the hypothesis of ancient remanent magnetizations of thermal origin that were preserved in the meteorite (Borlina et al., 2021).

## Data Availability Statement

All synthetic and experimental replication data, as well as MATLAB code implementing the technique, are available at the Harvard Dataverse: https://doi.org/10.7910/DVN/N4MMCT (Lima, 2023).

**Acknowledgments**
This work was supported in part by National Science Foundation (NSF) CDS&E-MSS Grants DMS-1521765 (EAL, BPW, CSB) and DMS-1521749 (DPH) and Geophysics Grant EAR-2044806 (EAL, BPW, CSB), National Aeronautics and Space Administration (NASA) Discovery Grant NNM16AA09C (BPW) and Solar Systems Workings Grant 80NSSC21K0154 (BPW), the MIT-France Seed Fund (EAL, CSB), and an Institut National de Recherche en Informatique et en Automatique (INRIA) grant to the associate team IMPINGE (LB). The authors thank K. Fabian and an anonymous reviewer for their insightful comments and suggestions, which helped improve this manuscript. EAL and BPW also thank Thomas F. Peterson, Jr. for his generous gift to the MIT Paleomagnetism Laboratory. We are grateful to Juliette Leblond, Dmitry Ponomarev, Sylvain Chevillard, and Roger Fu for many valuable discussions. Lastly, EAL would like to thank John P. Wikswo, a former mentor, for piquing EAL's interest in magnetic multipoles many years ago when recounting a question he was asked during oral examination as a young PhD candidate: "When computing a multipole expansion of the magnetic field produced by the human heart, can you place the origin of the expansion at the person's left foot?."

## References

Baratchart, L., Chevillard, S., Hardin, D. P., Leblond, J., Lima, E. A., & Marmorat, J.-P. (2019). Magnetic moment estimation and bounded extremal problems. *Inverse Problems and Imaging*, *13*(1), 39–67. https://doi.org/10.3934/ipi.2019003

Baratchart, L., Hardin, D. P., Lima, E. A., Saff, E. B., & Weiss, B. P. (2013). Characterizing kernels of operators related to thin-plate magnetizations via generalizations of Hodge decompositions. *Inverse Problems*, *29*(1), 015004. https://doi.org/10.1088/0266-5611/29/1/015004

Baratchart, L., Leblond, J., Lima, E. A., & Ponomarev, D. (2017). Magnetization moment recovery using Kelvin transformation and Fourier analysis. *Journal of Physics: Conference Series*, *904*, 012011. https://doi.org/10.1088/1742-6596/904/1/012011

Baudenbacher, F., Fong, L. E., Holzer, J. R., & Radparvar, M. (2003). Monolithic low-transition-temperature superconducting magnetometers for high resolution imaging magnetic fields of room temperature samples. *Applied Physics Letters*, *82*(20), 3487–3489. https://doi.org/10.1063/1.1572968

Berkovic, G., & Shafir, E. (2012). Optical methods for distance and displacement measurements. *Advances in Optics and Photonics*, *4*(4), 441–471. https://doi.org/10.1364/AOP.4.000441

Berndt, T., Muxworthy, A. R., & Fabian, K. (2016). Does size matter? Statistical limits of paleomagnetic field reconstruction from small rock specimens. *Journal of Geophysical Research: Solid Earth*, *121*(1), 15–26. https://doi.org/10.1002/2015JB012441

Blakely, R. J. (1996). *Potential theory in gravity & magnetic applications*. Cambridge University Press.

Bobyl, A., Podladchikov, Y., Austrheim, H., Jamtveit, B., Johansen, T., & Shantsev, D. (2007). Magnetic field visualization of magnetic minerals and grain boundary regions using magneto-optical imaging. *Journal of Geophysical Research*, *112*(B4), B04105. https://doi.org/10.1029/2006JB004305

Borlina, C. S., Weiss, B. P., Bryson, J. F. J., Bai, X. N., Lima, E. A., Chatterjee, N., & Mansbach, E. N. (2021). Paleomagnetic evidence for a disk substructure in the early solar system. *Science Advances*, *7*(42), eabj6928. https://doi.org/10.1126/sciadv.abj6928

Borlina, C. S., Weiss, B. P., Lima, E. A., Tang, F. Z., Taylor, R. J. M., Einsle, J. F., et al. (2020). Reevaluating the evidence for a Hadean-Eoarchean dynamo. *Science Advances*, *6*(15), eaav9634. https://doi.org/10.1126/sciadv.aav9634

Butkov, E. (1968). *Mathematical physics*. Addison-Wesley.

Cain, J. C., Hendricks, S. J., Langel, R. A., & Hudson, W. V. (1967). A proposed model for the international geomagnetic reference field-1965. *Journal of Geomagnetism and Geoelectricity*, *19*(4), 335–355. https://doi.org/10.5636/jgg.19.335

Cantor, R., & Koelle, D. (2004). Practical DC SQUIDS: Configuration and performance. In *The SQUID handbook* (pp. 171–217). John Wiley & Sons, Ltd. https://doi.org/10.1002/3527603646.ch5

Collinson, D. W. (1983). *Methods of rock magnetism and palaeomagnetism: Techniques and instrumentation*. Chapman and Hall.

Cortes-Ortuno, D., Fabian, K., & de Groot, L. V. (2021). Single particle multipole expansions from micromagnetic tomography. *Geochemistry, Geophysics, Geosystems*, *22*(4), e2021GC009663. https://doi.org/10.1029/2021GC009663

Cortes-Ortuno, D., Fabian, K., & de Groot, L. V. (2022). Mapping magnetic signals of individual magnetite grains to their internal magnetic configurations using micromagnetic models. *Journal of Geophysical Research: Solid Earth*, *127*(5), e2022JB024234. https://doi.org/10.1029/2022JB024234

Couch, S. M., Graziani, C., & Flocke, N. (2013). An improved multipole approximation for self-gravity and its importance for core-collapse supernova simulations. *The Astrophysical Journal*, *778*(2), 181. https://doi.org/10.1088/0004-637X/778/2/181

Courant, R., & Hilbert, D. (1991). *Methods of mathematical physics* (1st ed., Vol. 1). Wiley-Interscience.

Drung, D., & Mück, M. (2004). SQUID electronics. In *The SQUID handbook* (pp. 127–170). John Wiley & Sons, Ltd. https://doi.org/10.1002/3527603646.ch4

Egli, R., & Heller, F. (2000). High-resolution imaging using a high-Tc superconducting quantum interference device (SQUID) magnetometer. *Journal of Geophysical Research*, *105*(B11), 25709–25727. https://doi.org/10.1029/2000JB900192

Ehlmann, B. L., Anderson, F. S., Andrews-Hanna, J., Catling, D. C., Christensen, P., Cohen, B. A., et al. (2016). The sustainability of habitability on terrestrial planets: Insights, questions, and needed measurements from Mars for understanding the evolution of Earth-like worlds. *Journal of Geophysical Research: Planets*, *121*(10), 1927–1961. https://doi.org/10.1002/2016JE005134

Fong, L. E., Holzer, J. R., McBride, K. K., Lima, E. A., Baudenbacher, F., & Radparvar, M. (2005). High-resolution room-temperature sample scanning superconducting quantum interference device microscope configurable for geological and biomagnetic applications. *Review of Scientific Instruments*, *76*(5), 053703. https://doi.org/10.1063/1.1884025

Fu, R. R., Lima, E. A., Volk, M. W. R., & Trubko, R. (2020). High-sensitivity moment magnetometry with the quantum diamond microscope. *Geochemistry, Geophysics, Geosystems*, *21*(8), e2020GC009147. https://doi.org/10.1029/2020GC009147

Fu, R. R., Weiss, B. P., Lima, E. A., Harrison, R. J., Bai, X. N., Desch, S. J., et al. (2014). Solar nebula magnetic fields recorded in the Semarkona meteorite. *Science*, *346*(6213), 1089–1092. https://doi.org/10.1126/science.1258022

Fu, R. R., Weiss, B. P., Lima, E. A., Kehayias, P., Araujo, J., Glenn, D. R., et al. (2017). Evaluating the paleomagnetic potential of single zircon crystals using the Bishop Tuff. *Earth and Planetary Science Letters*, *458*, 1–13. https://doi.org/10.1016/j.epsl.2016.09.038

Fukuda, J., & Johnson, K. M. (2010). Mixed linear-non-linear inversion of crustal deformation data: Bayesian inference of model, weighting and regularization parameters. *Geophysical Journal International*, *181*(3), 1441–1458. https://doi.org/10.1111/j.1365-246X.2010.04564.x

Glenn, D. R., Fu, R. R., Kehayias, P., Le Sage, D., Lima, E. A., Weiss, B. P., & Walsworth, R. L. (2017). Micrometer-scale magnetic imaging of geological samples using a quantum diamond microscope. *Geochemistry, Geophysics, Geosystems*, *18*(8), 3254–3267. https://doi.org/10.1002/2017GC006946

Golub, G. H., & Van Loan, C. F. (2013). *Matrix computations* (4th ed.). Johns Hopkins University Press.

Gruhl, F., Muck, M., von Kreutzbruck, M., & Dechert, J. (2001). A scanning superconducting quantum interference device microscope with high spatial resolution for room temperature samples. *Review of Scientific Instruments*, *72*(4), 2090–2096. https://doi.org/10.1063/1.1359189

Hankard, F., Gattacceca, J., Fermon, C., Pannetier-Lecoeur, M., Langlais, B., Quesnel, Y., et al. (2009). Magnetic field microscopy of rock samples using a giant magnetoresistance-based scanning magnetometer. *Geochemistry, Geophysics, Geosystems*, *10*, Q10Y06. https://doi.org/10.1029/2009GC002750

Hansen, P. C. (1987). *Rank-deficient and discrete ill-posed problems: Numerical aspects of linear inversion*. Society for Industrial and Applied Mathematics.

Hansen, P. C., & O'Leary, D. P. (1993). The use of the L-curve in the regularization of discrete ill-posed problems. *SIAM Journal on Scientific Computing*, *14*(6), 1487–1503. https://doi.org/10.1137/0914086

Jackson, J. D. (1999). *Classical electrodynamics* (3rd ed.). Wiley.

Kawai, J., Oda, H., Fujihira, J., Miyamoto, M., Miyagi, I., & Sato, M. (2016). SQUID microscope with hollow-structured cryostat for magnetic field imaging of room temperature samples. *IEEE Transactions on Applied Superconductivity*, *26*(5), 1–5. https://doi.org/10.1109/TASC.2016.2536751

Kirschvink, J. L. (1981). How sensitive should a rock magnetometer be for use in paleomagnetism. In H. Weinstock, & W. C. Overton Jr. (Eds.), *SQUID applications to geophysics* (pp. 111–114). Society of Exploration Geophysicists.

Kletetschka, G., Schnabl, P., Sifnerova, K., Tasaryova, Z., Manda, S., & Pruner, P. (2013). Magnetic scanning and interpretation of paleomagnetic data from Prague Synform's volcanics. *Studia Geophysica et Geodaetica*, *57*(1), 103–117. https://doi.org/10.1007/s11200-012-0723-4

Koch, R. H., Foglietti, V., Rozen, J. R., Stawiasz, K. G., Ketchen, M. B., Lathrop, D. K., et al. (1994). Effects of radio frequency radiation on the dc SQUID. *Applied Physics Letters*, *65*(1), 100–102. https://doi.org/10.1063/1.113046

Lapotre, M. G. A., O'Rourke, J. G., Schaefer, L. K., Siebach, K. L., Spalding, C., Tikoo, S. M., & Wordsworth, R. D. (2020). Probing space to understand Earth. *Nature Reviews Earth & Environment*, *1*(3), 170–181. https://doi.org/10.1038/s43017-020-0029-y

Lee, S. Y., Matthews, J., & Wellstood, F. C. (2004). Position noise in scanning superconducting quantum interference device microscopy. *Applied Physics Letters*, *84*(24), 5001–5003. https://doi.org/10.1063/1.1763215

Lee, T. S., Chemla, Y. R., Dantsker, E., & Clarke, J. (1997). High-Tc SQUID microscope for room temperature samples. *IEEE Transactions on Applied Superconductivity*, *7*(2), 3147–3150. https://doi.org/10.1109/77.621999

Lima, E. (2023). Replication data for: Estimating the net magnetic moment of geological samples from planar field maps using multipoles [Dataset]. Harvard Dataverse. https://doi.org/10.7910/DVN/N4MMCT

Lima, E. A., Bruno, A. C., Carvalho, H. R., & Weiss, B. P. (2014). Scanning magnetic tunnel junction microscope for high-resolution imaging of remanent magnetization fields. *Measurement Science and Technology*, *25*(10), 105401. https://doi.org/10.1088/0957-0233/25/10/105401

Lima, E. A., Bruno, A. C., & Szczupak, J. (1999). Two-dimensional spatial frequency response of SQUID planar gradiometers. *Superconductor Science and Technology*, *12*(11), 949–952. https://doi.org/10.1088/0953-2048/12/11/376

Lima, E. A., Bruno, A. C., & Szczupak, J. (2002). Two-dimensional deconvolution technique to recover the original magnetic field from the flux measured by SQUID planar gradiometers. *Superconductor Science and Technology*, *15*(8), 1259–1267. https://doi.org/10.1088/0953-2048/15/8/316

Lima, E. A., & Weiss, B. P. (2009). Obtaining vector magnetic field maps from single-component measurements of geological samples. *Journal of Geophysical Research*, *114*(B6), B06102. https://doi.org/10.1029/2008JB006006

Lima, E. A., & Weiss, B. P. (2016). Ultra-high sensitivity moment magnetometry of geological samples using magnetic microscopy. *Geochemistry, Geophysics, Geosystems*, *17*(9), 3754–3774. https://doi.org/10.1002/2016GC006487

Lima, E. A., Weiss, B. P., Baratchart, L., Hardin, D. P., & Saff, E. B. (2013). Fast inversion of magnetic field maps of unidirectional planar geological magnetization. *Journal of Geophysical Research: Solid Earth*, *118*(6), 2723–2752. https://doi.org/10.1002/jgrb.50229

Louzada, K. L., Weiss, B. P., Maloof, A. C., Stewart, S. T., Swanson-Hysell, N. L., & Soule, S. A. (2008). Paleomagnetism of Lonar impact crater, India. *Earth and Planetary Science Letters*, *275*(3–4), 308–319. https://doi.org/10.1016/j.epsl.2008.08.025

Lowes, F. J. (1994). The geomagnetic eccentric dipole—Facts and fallacies. *Geophysical Journal International*, *118*(3), 671–679. https://doi.org/10.1111/j.1365-246X.1994.tb03992.x

Lowrie, W., & Fichtner, A. (2020). *Fundamentals of geophysics* (3rd ed.). Cambridge University Press.

Myre, J. M., Lascu, I., Lima, E. A., Feinberg, J. M., Saar, M. O., & Weiss, B. P. (2019). Using TNT-NN to unlock the fast full spatial inversion of large magnetic microscopy data sets. *Earth Planets and Space*, *71*(1), 14. https://doi.org/10.1186/s40623-019-0988-8

Pastore, Z., Lelievre, P., McEnroe, S. A., & Church, N. S. (2022). 3D joint inversion of scanning magnetic microscopy data. *Geophysical Research Letters*, *49*(1), e2021GL096072. https://doi.org/10.1029/2021GL096072

Pastore, Z., McEnroe, S. A., Church, N. S., & Oda, H. (2021). Mapping and modeling sources of natural remanent magnetization in the microcline–sillimanite gneiss, Northwest Adirondack Mountains: Implications for crustal magnetism. *Geochemistry, Geophysics, Geosystems*, *22*(3), e2020GC009580. https://doi.org/10.1029/2020GC009580

Pastore, Z., McEnroe, S. A., ter Maat, G. W., Oda, H., Church, N. S., & Fumagalli, P. (2018). Mapping magnetic sources at the millimeter to micrometer scale in dunite and serpentinite by high-resolution magnetic microscopy. *Lithos*, *323*, 174–190. https://doi.org/10.1016/j.lithos.2018.09.018

Raab, R. E., & de Lange, O. L. (2005). *Multipole theory in electromagnetism: Classical, quantum, and symmetry aspects, with applications*. Oxford University Press.

Roth, B. J., Sepulveda, N. G., & Wikswo, J. P. (1989). Using a magnetometer to image a two-dimensional current distribution. *Journal of Applied Physics*, *65*(1), 361–372. https://doi.org/10.1063/1.342549

Schöne, S., Mück, M., Thummes, G., & Heiden, C. (1997). Investigation of the response of superconducting quantum interference devices to temperature variation. *Review of Scientific Instruments*, *68*(1), 85–88. https://doi.org/10.1063/1.1147709

Tan, S., Ma, Y. P., Thomas, I. M., & Wikswo, J. P. (1996). Reconstruction of two-dimensional magnetization and susceptibility distributions from the magnetic field of soft magnetic materials. *IEEE Transactions on Magnetics*, *32*(1), 230–234. https://doi.org/10.1109/20.477575

Tauxe, L. (2010). *Essentials of paleomagnetism*. University of California Press.

Uehara, M., & Nakamura, N. (2007). Scanning magnetic microscope system utilizing a magneto-impedance sensor for a nondestructive diagnostic tool of geological samples. *Review of Scientific Instruments*, *78*(4), 043708. https://doi.org/10.1063/1.2722402

Uehara, M., van der Beek, C., Gattacceca, J., Skidanov, V., & Quesnel, Y. (2010). Advances in magneto-optical imaging applied to rock magnetism and paleomagnetism. *Geochemistry, Geophysics, Geosystems*, *11*(5), Q05Y09. https://doi.org/10.1029/2009GC002653

Usui, Y., Uehara, M., & Okuno, K. (2012). A rapid inversion and resolution analysis of magnetic microscope data by the subtractive optimally localized averages method. *Computers & Geosciences*, *38*(1), 145–155. https://doi.org/10.1016/j.cageo.2011.05.001

Weiss, B. P., Bai, X. N., & Fu, R. R. (2021). History of the solar nebula from meteorite paleomagnetism. *Science Advances*, *7*(1). https://doi.org/10.1126/sciadv.aba5967

Weiss, B. P., Fong, L. E., Vali, H., Lima, E. A., & Baudenbacher, F. J. (2008). Paleointensity of the ancient Martian magnetic field. *Geophysical Research Letters*, *35*(23), L23207. https://doi.org/10.1029/2008GL035585

Weiss, B. P., Fu, R. R., Einsle, J. F., Glenn, D. R., Kehayias, P., Bell, E. A., et al. (2018). Secondary magnetic inclusions in detrital zircons from the Jack Hills, Western Australia, and implications for the origin of the geodynamo. *Geology*, *46*(5), 427–430. https://doi.org/10.1130/G39938.1

Weiss, B. P., Lima, E. A., Fong, L. E., & Baudenbacher, F. J. (2007). Paleomagnetic analysis using SQUID microscopy. *Journal of Geophysical Research*, *112*(B9), B09105. https://doi.org/10.1029/2007JB004940

Weiss, B. P., Pedersen, S., Garrick-Bethell, I., Stewart, S. T., Louzada, K. L., Maloof, A. C., & Swanson-Hysell, N. L. (2010). Paleomagnetism of impact spherules from Lonar crater, India and a test for impact-generated fields. *Earth and Planetary Science Letters*, *298*(1–2), 66–76. https://doi.org/10.1016/j.epsl.2010.07.028

Wikswo, J. P., & Swinney, K. R. (1984). A comparison of scalar multipole expansions. *Journal of Applied Physics*, *56*(11), 3039–3049. https://doi.org/10.1063/1.333885

Wikswo, J. P., & Swinney, K. R. (1985). Scalar multipole expansions and their dipole equivalents. *Journal of Applied Physics*, *57*(9), 4301–4308. https://doi.org/10.1063/1.334589

## References From the Supporting Information

Atfeh, B., Baratchart, L., Leblond, J., & Partington, J. R. (2010). Bounded extremal and Cauchy–Laplace problems on the sphere and shell. *Journal of Fourier Analysis and Applications*, *16*(2), 177–203. https://doi.org/10.1007/s00041-009-9110-0

Axler, S., Bourdon, P., & Ramey, W. (2000). *Harmonic function theory*. Springer.

Rudin, W. (1991). *Functional analysis*. Mc Graw-Hill.

Schwartz, L. (1950). *Théorie des distributions*. Tome I. Hermann & Cie.

*Geochemistry, Geophysics, Geosystems*

Supporting Information for

# Estimating the Net Magnetic Moment of Geological Samples from Planar Field Maps Using Multipoles

**Eduardo A. Lima[1], Benjamin P. Weiss[1], Caue S. Borlina[1,2], Laurent Baratchart[3], and Douglas P. Hardin[4]**

[1]Department of Earth, Atmospheric, and Planetary Sciences, Massachusetts Institute of Technology, Cambridge, MA 02139 USA

[2]Department of Earth and Planetary Sciences, Johns Hopkins University, Baltimore, MD 21218 USA

[3]Centre de Recherche INRIA Sophia Antipolis - Méditerranée, 06902 Sophia-Antipolis Cedex, France

[4]Center for Constructive Approximation, Department of Mathematics, Vanderbilt University, Nashville, TN 37240 USA

Corresponding author: Eduardo Andrade Lima (limaea@mit.edu)

## Contents of this file



## Introduction

In this document, we have collected results and ancillary derivations that further support the results shown in the main text and provide a deeper explanation for some statements that readers unfamiliar with certain aspects of the technique may find useful.

**Text S1: Factors Contributing to Upward Continuation Error**

Two main factors contribute to errors in the calculation of upward continuation of planar magnetic maps: limited mapping area and finite spatial sampling resolution. Given that such errors may impact moment estimation accuracy, we model their effect on the magnetic data and briefly discuss ways to mitigate them.

We represent the effect of a finite mapping area by a two-dimensional characteristic function $\chi$, which is equal to 1 inside the mapping area and 0 outside:

$$\tilde{B}_z(x,y,h) = B_z(x,y,h)\cdot\chi(x,y) \quad , \tag{S1}$$

where $\tilde{B}_z$ denotes the magnetic data cropped to the mapping area (i.e., the field map). Calculation of upward continuation is exact when the magnetic data are known over the whole plane (Blakely, 1996). However, in practice that is never achieved and instead we only have access to $\tilde{B}_z$.

The impact of this on the calculation of the upward continuation can be modeled analytically. We begin by expressing the field data upward continued to the plane $z = h + \Delta h$ as the convolution of the original field data (known over the whole plane $z = h$) with the Poisson kernel, shown in square brackets:

$$\begin{aligned} B_z(x,y,h+\Delta h) &= B_z(x,y,h) * \left[\frac{2\pi\Delta h}{\left(x^2+y^2+\Delta h\right)^{3/2}}\right] = \left[B_z(x,y,h)\cdot\left(\chi(x,y)+\overline{\chi}(x,y)\right)\right] * \left[\frac{2\pi\Delta h}{\left(x^2+y^2+\Delta h\right)^{3/2}}\right] = \\ &= \left\{\tilde{B}_z(x,y,h) * \left[\frac{2\pi\Delta h}{\left(x^2+y^2+\Delta h\right)^{3/2}}\right]\right\} + \left\{\overline{\tilde{B}}_z(x,y,h) * \left[\frac{2\pi\Delta h}{\left(x^2+y^2+\Delta h\right)^{3/2}}\right]\right\} \quad , \end{aligned} \tag{S2}$$

where $*$ stands for the (two-dimensional) convolution operation, $\overline{\chi}$ denotes the complement of $\chi$ (i.e., zero inside the mapping area and one outside) such that $\chi + \overline{\chi}$ is the unit constant function and $\overline{\tilde{B}}_z(x,y,h) = B_z(x,y,h)\cdot\overline{\chi}(x,y)$ represents the magnetic data outside the mapping area. The left term in curly braces is the cropped data upward continued and the right term in curly braces is all the data outside the mapping area upward continued. Equation (S2) then allows us to express the error introduced by using cropped magnetic data in the calculation of the upward continuation:

$$\begin{aligned} \tilde{B}_z(x,y,h+\Delta h) &= \tilde{B}_z(x,y,h) * \left[\frac{2\pi\Delta h}{\left(x^2+y^2+\Delta h\right)^{3/2}}\right] = B_z(x,y,h+\Delta h) - \overline{\tilde{B}}_z(x,y,h) * \left[\frac{2\pi\Delta h}{\left(x^2+y^2+\Delta h\right)^{3/2}}\right] = \\ &= B_z(x,y,h+\Delta h) + E(x,y,h,\Delta h) \quad . \end{aligned} \tag{S3}$$

Thus, the measured magnetic data upward continued to a sensor-to-sample distance of $h + \Delta h$ is given by the exact field at $h + \Delta h$ plus an error term $E$ that depends on the data that were not measured

$$E(x,y,h,\Delta h) = -\overline{\tilde{B}}_z(x,y,h) * \left[ \frac{2\pi\Delta h}{\left(x^2+y^2+\Delta h\right)^{3/2}} \right] . \tag{S4}$$

Given that the Poisson kernel is a single-peaked function whose width depends on the amount of upward continuation $\Delta h$, (S4) tells us that the error will generally be higher at the edges of the field map and decrease towards the center. In addition, the error strongly depends on the magnitude of the field at the edges of the map: the larger the mapping area, the smaller $\overline{\tilde{B}}_z(x,y,h)$ and the closer $\tilde{B}_z(x,y,h+\Delta h)$ is to the actual field at $h+\Delta h$. Similarly, the smaller $\Delta h$, the narrower the Poisson kernel becomes and the smaller the error is.

How much of the error "bleeds" into the center of the map is determined by $\Delta h$, which regulates the width of the Poisson kernel. As a rule of thumb, the larger the mapping area the higher the degree of upward continuation that can be adequately performed. Clearly, the mapping area is also limited by noise contamination, as measuring past a certain distance from the center will not yield any relevant magnetic data once the magnetic signal drops below the sensor's noise floor. This overall behavior highlights the importance of mapping the field beyond the region containing magnetic sources, whenever possible, so as to adequately capture the field decay and make the field strength as small as possible at the edges of the magnetic map. For the typical mapping areas used in SQUID microscopy, such as the ones shown in this paper, upward continuing the data by an amount greater than one or two times the sensor-to-sample distance may often lead to significant error in moment estimation.

The inaccuracies associated with finite step sizes are more easily understood in the Fourier domain. In this case, convolution operations are replaced by multiplications and the Poisson kernel takes its familiar expression in the Fourier domain:

$$\hat{B}_z(k_x,k_y,h+\Delta h) = \hat{B}_z(k_x,k_y,h)\cdot e^{-\Delta h k} , \tag{S5}$$

where the hat symbol denotes a two-dimensional Fourier transform performed on the $x$ and $y$ variables and $k=\sqrt{k_x^2+k_y^2}$. This expression is exact when the Fourier transform is computed over the whole $k_x$-$k_y$ spatial frequency plane. This, however, corresponds to an infinitesimal step size, which is obviously not attainable in practice. Thus, (S5) is effectively only computed in a rectangular region $R$ of the spatial frequency plane determined by the mapping step size

$$R: |k_x| \le \frac{2\pi}{\Delta x}, |k_y| \le \frac{2\pi}{\Delta y} , \tag{S6}$$

where $\Delta x$ and $\Delta y$ are the step sizes in the $x$ and $y$ directions, respectively, which are typically equal. Owing to the exponential decay of the upward continuation low-pass filter and the band-limited characteristics of the spectrum of the field map, such inaccuracies are ordinarily of secondary importance, unless coarse spatial sampling is used for some reason.

We use a set of 50,000 dipoles with arbitrary orientations randomly distributed in a 100 μm cubic volume to illustrate how the mapping area effects prevail under normal conditions (Fig. S10). Notice that this error is concentrated on the edges of the map, as predicted by (S4), accounting for over 99.5% of the overall inaccuracies in the upward continuation in this case.

**Text S2: On the Density of Multipolar Fields**

**S2.1: Notation and preliminaries**

We let $S$ be a connected, compact subset of $\mathbb{R}^3$, which we think of as being the sample. We further let $O \subset \mathbb{R}^2$ be a planar bounded connected Lipschitz-regular open set (that is, whose boundary is locally a Lipschitz graph), and we put $Q := \overline{O} \times \{h\}$ which is a compact subset of the horizontal plane $\mathbb{R}^2 \times \{h\}$ in $\mathbb{R}^3$, where $h > 0$ is the "height" at which measurements are performed and $Q$ the area where these measurements are taken. We assume throughout that $S \subset \{x = (x_1, x_2, x_3)^t \in \mathbb{R}^3 : x_3 \leq h - \varepsilon\}$ for some $\varepsilon > 0$; namely, that $Q$ lies "above" $S$. Here and below, a superscript "t" means "transpose".

We need a few functional spaces on $\mathbb{R}^n$, where $n$ will be set to 2 or 3. We write $C^\infty(\Omega)$ for the space of smooth functions on an open set $\Omega \subset \mathbb{R}^n$ having continuous derivatives of any order, and $C_0^\infty(\Omega)$ for the space of smooth functions with compact support in $\Omega$. Recall that distributions on $\Omega$ are linear forms on $C_0^\infty(\Omega)$ that are continuous for a certain topology, the precise definition of which may be found in (Schwartz, 1950, Sec. I.2). The duality product between distributions and functions will be denoted with brackets, as in $\langle \mathfrak{d}, \varphi \rangle$. The support of a distribution $\mathfrak{d}$ on $\Omega$, denoted by $\operatorname{supp} \mathfrak{d}$, is the largest closed set $E \subset \Omega$ such that $\mathfrak{d}(\varphi) = 0$ for all $\varphi$ in $C_0^\infty(\Omega \setminus E)$. When $\operatorname{supp} \mathfrak{d}$ is compact in $\Omega$, we can find $\varphi \in C_0^\infty(\Omega)$ which is identically 1 on $\operatorname{supp} \mathfrak{d}$ and then, for $f \in C^\infty(\Omega)$, the value of $\langle \mathfrak{d}, \varphi f \rangle$ does not depend on the exact choice of such a $\varphi$. Hence, a distribution with compact support acts naturally on $C^\infty$-smooth functions even if they do not have compact support, and may be regarded as a distribution on any open set containing its support.

For $\alpha = (\alpha_1, \cdots, \alpha_n)$ a multi-index (that is: a $n$-tuple of nonnegative integers), we put $\partial^\alpha$ for the differential operator $\partial_{x_1}^{\alpha_1} \cdots \partial_{x_3}^{\alpha_n}$, where $x = (x_1, \cdots, x_n)^t$ displays the coordinates of $x \in \mathbb{R}^n$ and $\partial_{x_j}^{\alpha_j}$ denotes the $\alpha_j$-th partial derivative with respect to the variable $x_j$. The $\alpha$-derivative of a distribution $\mathfrak{d}$ acts on $\varphi \in C_0^\infty(\Omega)$ by $\langle \partial^\alpha \mathfrak{d}, \varphi \rangle := (-1)^{|\alpha|} \langle \mathfrak{d}, \partial^\alpha \varphi \rangle$, where $|\alpha| := \alpha_1 + \cdots + \alpha_n$ is called the *weight* of $\alpha$.

For any integer $m > 0$, the previous considerations extend at once to $\mathbb{R}^m$-valued distributions, acting naturally on $(C_0^\infty(\Omega))^m$ *via* the Euclidean scalar product. That is: for $\mathbf{D} = (D_1, \cdots, D_m)$ $\mathbb{R}^m$-valued distribution and $\mathbf{f} = (f_1, \cdots, f_m)$ a $\mathbb{R}^m$-valued function, we set $\langle \mathbf{D}, \mathbf{f} \rangle := \sum_j \langle D_j, f_j \rangle$.

Recall the familiar divergence operator, acting on $n$-vectors of differentiable quantities by $\operatorname{div}(a_1, \cdots, a_n) = \sum_j \partial_{x_j} a_j$, and the Newton kernel with pole at $x \in \mathbb{R}^3$, which is the function $N_x : \mathbb{R}^3 \setminus \{x\} \to \mathbb{R}$ defined by $N_x(y) := -1/(4\pi |x - y|)$, with $|x|$ to mean the Euclidean norm of $x$. For $\mathbf{D}$ a $\mathbb{R}^3$-valued distribution in $\mathbb{R}^3$ supported on $S$, we define its *magnetic potential* at a point $x \in \mathbb{R}^3 \setminus S$ by the formula:

$$\Phi(\mathbf{D})(x) := \langle \operatorname{div} \mathbf{D}, N_x \rangle = -\langle \mathbf{D}, \nabla_y N_x \rangle = \frac{1}{4\pi} \left\langle \mathbf{D}, \frac{x - \cdot}{|x - \cdot|^3} \right\rangle , \tag{S7}$$

where we used the definition of distributional derivatives and the notation $\nabla_y$ to indicate the gradient with respect to $y$; here and below, a dot as in $(x - \cdot)/|x - \cdot|^3$ designates a dummy variable. In fact, $\Phi(\mathbf{D})$ is the (distributional) solution to

$$\Delta \Phi = \operatorname{div} \mathbf{D} \tag{S8}$$

that vanishes at infinity, with $\Delta := \Sigma_{1 \le j \le 3} \partial_{x_j}^2$ to mean the Laplace operator.

The *magnetic field* of $\mathbf{D}$ is defined as the $\mathbb{R}^3$-valued vector field $\mathbf{b}(\mathbf{D})$ on $\mathbb{R}^3 \setminus S$ given by $\mathbf{b}(\mathbf{D}) := -\mu_0 \nabla \Phi(\mathbf{D})$, where $\mu_0 = 4\pi \times c$ with $c = 10^{-7}\, H\, m^{-1}$ and $\nabla$ stands for the gradient. Standard calculus with distributions shows that (S7) is a smooth function of $x$ and that differentiation can be performed inside the duality bracket (Rudin, 1991, Theorem 6.35), therefore the $j$-th component of the magnetic field of $\mathbf{D} = (D_1, D_2, D_3)$ at $x \in \mathbb{R}^3 \setminus S$ can be rewritten as:

$$[\mathbf{b}(\mathbf{D})(x)]_j := -c \left( \left\langle \frac{1}{|x - \cdot|^3}, D_j \right\rangle - 3 \left\langle [x - \cdot]_j \frac{(x - \cdot)}{|x - \cdot|^5}, \mathbf{D} \right\rangle \right) \qquad 1 \le j \le 3 . \tag{S9}$$

Note that $\Phi(\mathbf{D})$ and the components of $\mathbf{b}(\mathbf{D})$ are harmonic functions on $\mathbb{R}^3 \setminus S$: this follows at once from (S8) and the fact that derivatives commute, taking into account that $\mathbf{D}$ is supported on $S$.

A *dipole* is a $\mathbb{R}^3$-valued distribution of the form $\mathbf{v}\delta_x$, where $\mathbf{v} \in \mathbb{R}^3$ and $\delta_x$ is the Dirac mass at $x \in \mathbb{R}^3$. For $\alpha \in \mathbb{N}^3$ a multi-index with $|\alpha| > 0$, a *multipole* is a distribution of the form $\partial^\alpha \mathbf{d}$ where $\mathbf{d}$ is a dipole. We speak of a $\alpha$ - multipole when we need to specify $\alpha$, and call $|\alpha|$ the *order* of the multipole. Clearly, $\operatorname{supp} \mathbf{v}\delta_x = \operatorname{supp} \partial^\alpha (\mathbf{v}\delta_x) = \{x\}$. In the case of either a dipole or a multipole, we call $\mathbf{v}$ the *associated vector*.

**S2.2: Density of multipolar fields**

Let $\mathcal{D}_S^{'}$ indicate the space of $\mathbb{R}^3$-valued distributions supported on $S$. By definition, the *forward operator* $A:\mathcal{D}_S^{'}\to L^2(Q)$ maps a $\mathbb{R}^3$-valued distribution to the restriction on $Q$ of the vertical component of its field: $A(\mathbf{D}):=\left(\mathbf{b}(\mathbf{D})]_3\right)_{|Q}$. This is (an idealized version of) the measurement operator.

With a slight abuse of notation, we continue to use the letter $A$ to designate the restriction of $A$ to various subspaces of $\mathcal{D}_S^{'}$. Since the distance $\mathrm{d}(Q,S)$ from $Q$ to $S$ is strictly positive, it is obvious from (S9) that $A$ is indeed valued in $L^2(Q)$ (and even in the space $C^\infty(Q)$ of smooth functions on $Q$, meaning they are smooth in a neighborhood of $Q$). Writing $(e_j)_{1\le j\le 3}$ for the canonical basis of $\mathbb{R}^3$ and using a dot to indicate the Euclidean scalar product, we also introduce the operator $A^*:L^2(Q)\to\left(C^\infty(S)\right)^3$ given by

$$A^*(\Psi)(x):=-\frac{\mu_0}{4\pi}\int\Psi(y)\mathbf{K}(x-y)\,dy,\qquad x\in S, \tag{S10}$$

where

$$\mathbf{K}(x)=\frac{e_3}{|x|^3}-3x\frac{e_3\cdot x}{|x|^5}=\nabla\left(\frac{e_3\cdot x}{|x|^3}\right). \tag{S11}$$

In view of (S11), a compact way of re-writing (S10) is

$$A^*(\Psi)(x):=-\mu_0\nabla(\nabla U^\psi\cdot e_3)(x),\qquad U^\psi(x)=-\frac{1}{4\pi}\int\frac{\Psi(y)}{|x-y|}dy, \tag{S12}$$

and it follows from first principles that

$$\langle\psi,A\,\mathbf{D}\rangle=\langle A^*\psi,\mathbf{D}\rangle,\qquad \psi\in L^2(Q). \tag{S13}$$

Indeed, since $A$ and $A^*$ are convolution operators by definition [see (S9) and (S10)], it follows from (Rudin, 1991, Theorem 6.35) that (S13) holds when $\psi\in C_0^\infty(O)$, and we can pass to the limit since the latter space is dense in $L^2(Q)$ while convergence of $\psi_n$ to $\psi$ in $L^2(Q)$ entails convergence of $A^*\psi_n$ to $A^*\psi$ together with all its derivatives, the convergence being uniform in a neighborhood of $S$; this is enough to ensure convergence of $\langle A^*\psi_n,\mathbf{D}\rangle$ to $\langle A^*\psi,\mathbf{D}\rangle$, because distributions with compact support have finite order (Rudin, 1991, Theorem 6.24).

Let us now introduce the space $\mathcal{M}(z)$ generated by all dipoles and multipoles of any order and arbitrary associated vector supported in a point $z$. As the derivatives $\partial^\alpha(1/|x|)$ are of the form $P_\alpha/|x|^{2|\alpha|+1}$, where $P_\alpha$ ranges over all homogeneous harmonic polynomials of degree $|\alpha|$ when $\alpha\in\mathbb{N}^3$ ranges over multi-indices of given weight (Axler et al., 2000, Theorem 5.25), and since the

restrictions to the unit sphere of homogeneous harmonic polynomials of degree $k$ are precisely the spherical harmonics of degree $k$ (Axler et al., 2000, p. 80) while magnetic fields are harmonic gradients (more precisely: gradients of a harmonic potential) outside the support of the distribution generating them, it follows from Atfeh et al. (2010, Lemma 4) that magnetic fields of members of $\mathcal{M}(z)$, when restricted to the unit sphere centered at $z$, are dense (with respect to any $L^p$-norm, $1 \leq p \leq \infty$) in the space of restrictions to that sphere of all magnetic fields generated by a distribution compactly supported inside the unit ball centered at $z$. Using Kelvin transform and dilations, this density property extends easily on any sphere compactly containing both the support of the distributions generating the fields and the point $z$.

Below, we prove a related density property for the normal component of the field, but in a planar context.

**Lemma S2.1.** *For any $z \in S$, the image $A\big(\mathcal{M}(z)\big)$ of $\mathcal{M}(z)$ under $A$ is dense in $L^2(Q)$.*

Proof. If the conclusion of the lemma is false, there is a nonzero function $f \in L^2(Q)$ which is orthogonal to $A\big(\mathcal{M}(z)\big)$; *i.e.*, such that

$$0 = \langle f, A(\partial^\alpha(\mathbf{v}\delta_x)\rangle = \langle A^* f, \partial^\alpha(\mathbf{v}\delta_x\rangle = (-1)^{|\alpha|}\langle \partial^\alpha(A^* f), \mathbf{v}\delta_x\rangle = (-1)^{|\alpha|}\partial^\alpha(A^* f)(x)\cdot\mathbf{v} \qquad \text{(S14)}$$

for all multi-indices $\alpha \in \mathbb{N}^3$ and all $\mathbf{v} \in \mathbb{R}^3$; in (S14), we used (S13) to get the second equality. For $x \in \mathbb{R}^3 \setminus Q$, let $Bf(x)$ denote the right-hand side of (S10). Then, $Bf$ coincides with $A^* f$ on a neighborhood of $S$, and it is real analytic in $\mathbb{R}^3 \setminus Q$ because it is harmonic there (Axler et al., 2000, Theorem 1.28) [harmonicity is obvious from (S12)]. As (S14) tells us that all the derivatives of $A^* f$ (therefore also of $Bf$ vanish at $x$, we get that $Bf \equiv 0$ by real analyticity. Now, if $V \subset \mathbb{R}^2$ is a non-empty open set and if we let $W := V \times \{0\} \subset \mathbb{R}^3$, it follows from the discussion after Baratchart et al. (2019, Eq. (9)) that the restriction map $f \mapsto \big(Bf\big)_{|W}$ is injective. Hence $f \equiv 0$, a contradiction that proves our contention.

**Text S3: Magnetic Data from Both Sides of a Geological Sample**

Having magnetic data available from both the top and bottom sides of a sample may be advantageous for constraining inversions and separating magnetization components (Baratchart et al., 2013; Egli & Heller, 2000; Pastore et al., 2022), which is potentially feasible in magnetic microscopy unlike in other applications (e.g., aeromagnetic surveys). In particular, magnetic data from both sides may significantly improve numerical issues observed in the computation of net moments. Whereas, in principle, it is possible to flip a sample over and obtain a field map of its bottom surface, in practice experimental constraints often make it difficult to use such data in an effective way. Accurate registration of the top and bottom field maps could be very hard to achieve without adding magnetic and/or optical

markers to the sample mount, which need to be placed far enough to avoid interfering with the sample's magnetic field and increase sample preparation and measurement times. In addition, significant differences in spatial resolution and moment sensitivity between the top and bottom maps are frequently experienced because geological samples are usually mounted on glass or quartz substrates owing to their fragile nature when polished down to 100 μm or less. Therefore, when mapping the sample's bottom surface, the thickness of the substrate adds to the nominal sensor-to-sample distance, which may increase the latter by >100 times (the smaller the nominal sensor-to-sample distance the more pronounced those differences are). Lastly, precise estimates of the difference in effective sensor-to-sample distance between the two sides are needed to build an expanded matrix $\mathbf{A}$ that incorporates information from the bottom side of the sample.

In this paper, we assume that only field data from the top side of the sample is available. Additional data from the bottom side, if reliably obtainable, would only help improve accuracy of net moment estimates. In this case, a straightforward way to compute net moment estimates from two-sided data would consist of "stacking" in vector $\mathbf{b}$ the magnetic data measured from the top and bottom sides and expanding matrix $\mathbf{A}$ accordingly, yielding a system with $2K$ linear equations and $N^2 + 2N$ unknowns.

**References**


Atfeh, B., Baratchart, L., Leblond, J., & Partington, J. R. (2010). Bounded extremal and Cauchy–Laplace problems on the sphere and shell. *Journal of Fourier Analysis and Applications*, *16*(2), 177–203. https://doi.org/10.1007/s00041-009-9110-0

Axler, S., Bourdon, P., & Ramey, W. (2000). *Harmonic function theory*. New York, NY: Springer.

Baratchart, L., Hardin, D. P., Lima, E. A., Saff, E. B., & Weiss, B. P. (2013). Characterizing kernels of operators related to thin-plate magnetizations via generalizations of Hodge decompositions. *Inverse Problems*, *29*(1), 015004. https://doi.org/10.1088/0266-5611/29/1/015004

Baratchart, L., Chevillard, S., Hardin, D. P., Leblond, J., Lima, E. A., & Marmorat, J.-P. (2019). Magnetic moment estimation and bounded extremal problems. *Inverse Problems & Imaging*, *13*(1), 39–67. https://doi.org/10.3934/ipi.2019003

Blakely, R. J. (1996). *Potential theory in gravity & magnetic applications*. Cambridge: Cambridge University Press.

Egli, R., & Heller, F. (2000). High-resolution imaging using a high-Tc superconducting quantum interference device (SQUID) magnetometer. *Journal of Geophysical Research: Solid Earth*, *105*(B11), 25709–25727. https://doi.org/10.1029/2000JB900192

Pastore, Z., Lelievre, P., McEnroe, S. A., & Church, N. S. (2022). 3D joint inversion of scanning magnetic microscopy data. *Geophysical Research Letters*, *49*(1), e2021GL096072. https://doi.org/10.1029/2021GL096072

Rudin, W. (1991). *Functional analysis*. New York, NY: Mc Graw-Hill.

Schwartz, L. (1950). *Théorie des distributions. Tome I*. Hermann & Cie., Paris.

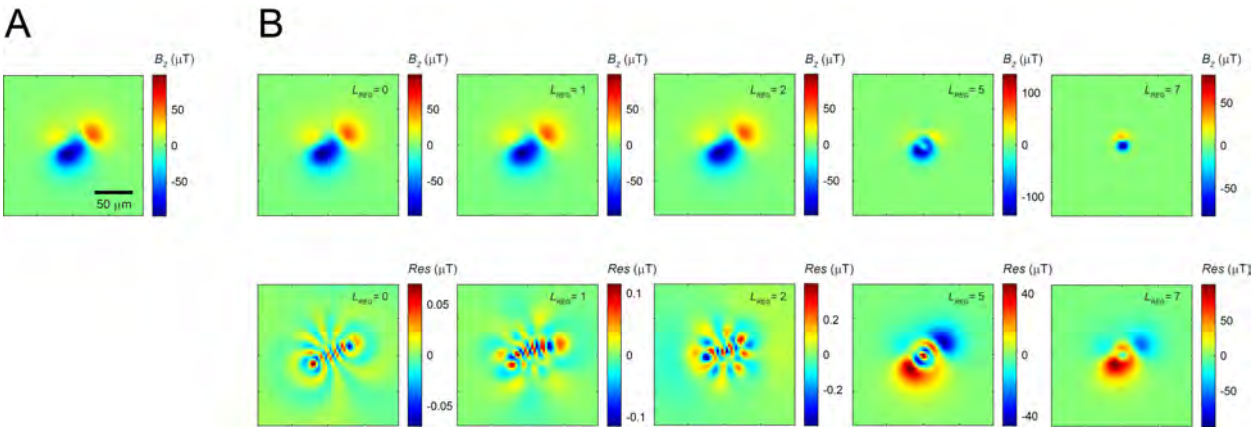


**Figure S1.** Effect of the regularization parameter $L_{REG}$ on the ability of the model to reproduce the data. Introducing regularization via SVD truncation stabilizes net moment estimates in the presence of noise at the expense of matching the field data. **(A)** Simulated $B_z$ field map for Source A at a 25 μm sensor-to-sample distance (see Fig. 2A). **(B)** Model field map for increasing values of $L_{REG}$, ranging from no truncation ($L_{REG} = 0$) to the maximum truncation ($L_{REG} = 7$), which corresponds to the preservation of only three coefficients and singular values/vectors. Notice the increasing residuals with larger degree of regularization introduced. Truncation of the SVD is not equivalent to truncating the multipole series, as each left singular vector represents a linear combination of multipole components. This is evidenced by the fact that the field map obtained for $L_{REG} = 7$ is substantially different from the dipole components shown in Fig. 2B (i.e., the first three terms in the multipole expansion), exhibiting a noticeably different spatial decay; instead, it corresponds to a linear combination of the first three left singular vectors shown in Fig. 3.

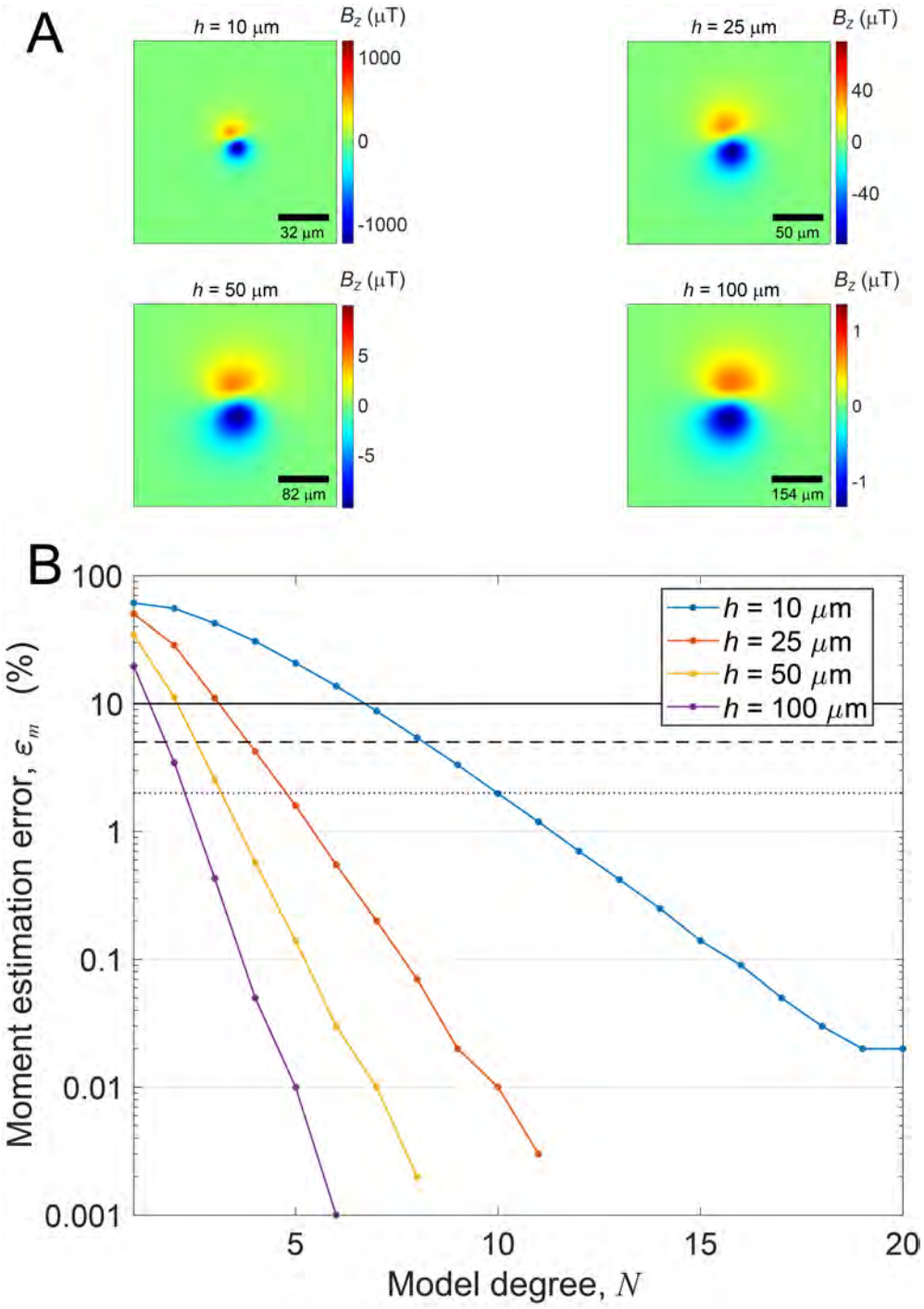


**Figure S2.** Net moment estimation results for Source B [two dipoles vertically spaced (i.e., in the *Z* direction), noiseless case; Table 2] with varying multipole model degrees. **(A)** $B_z$ field maps simulated at four different sensor-to-sample distances. Notice the apparent directional change as the magnetic field from the top dipole becomes less prominent with increasing sensor-to-sample distance and the map progressively reflects the net moment direction. **(B)** Net moment estimation error as a function of model degree for the maps shown in (A). Solid, dashed, and dotted black lines represent 10%, 5%, and 2% thresholds for the estimation error, respectively.

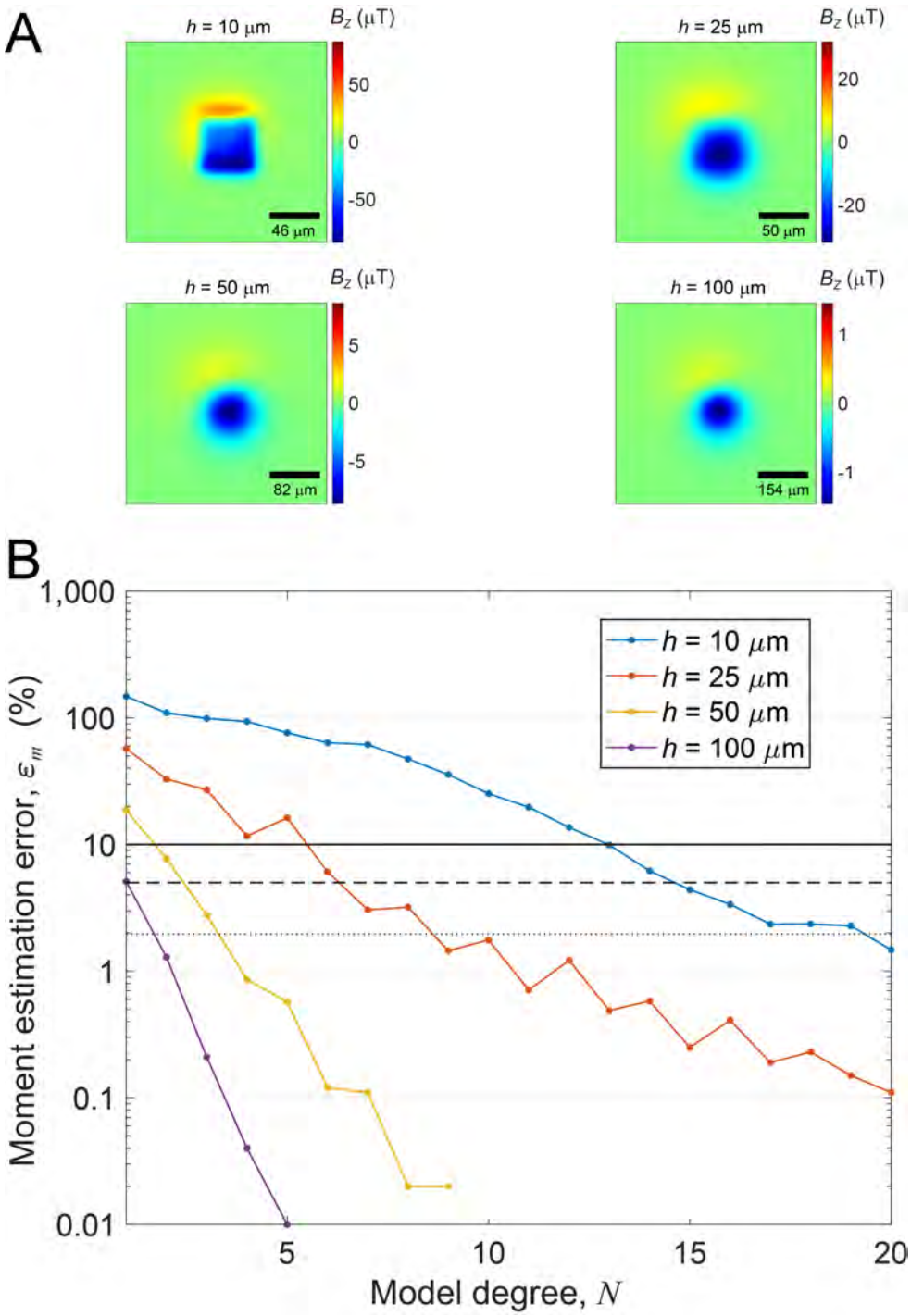


**Figure S3.** Net moment estimation results for Source C (uniformly magnetized square thin slab without noise; Table 2) with varying multipole model degree. **(A)** $B_z$ field maps simulated at four different sensor-to-sample distances. **(B)** Net moment estimation error as a function of model degree for the maps shown in (A). Solid, dashed, and dotted black lines represent 10%, 5%, and 2% thresholds for the estimation error, respectively.

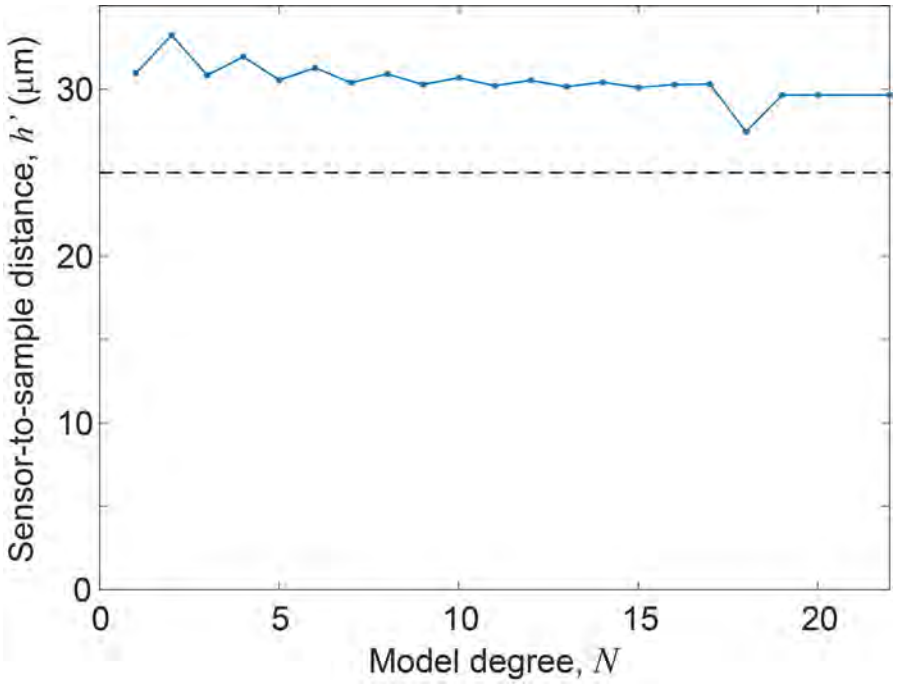


**Figure S4.** Sensor-to-sample distance associated with each moment estimate for Source A (noiseless case), obtained with varying model degree, and the true sensor-to-sample distance (25 μm – see Fig. 5) represented by a black dashed line. As expected, our multipole expansion model does not recover the physical distance given that it places the origin of the expansion at the depth best suited to represent the data using a spherical harmonic multipole expansion truncated at degree $N$.

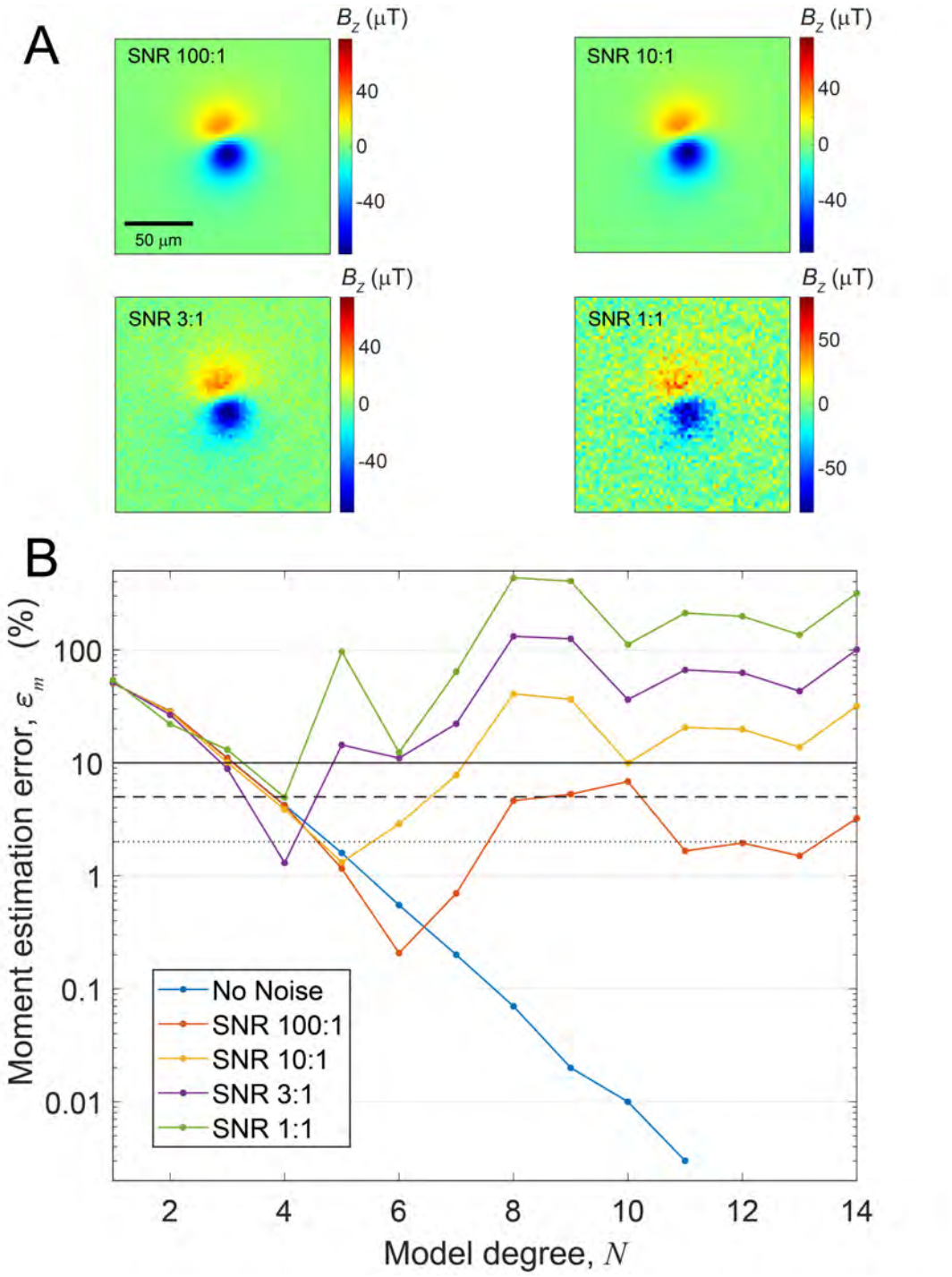


**Figure S5.** Net moment estimation results for Source B with varying model degree for different signal-to-noise ratios (SNRs). **(A)** Simulated $B_z$ field maps for a sensor-to-sample distance of 25 μm with SNR ranging from infinite (noiseless) down to 1:1. **(B)** Moment estimation error as a function of model degree for 5 different SNRs. Solid, dashed, and dotted black lines represent 10%, 5%, and 2% thresholds for the estimation error, respectively.

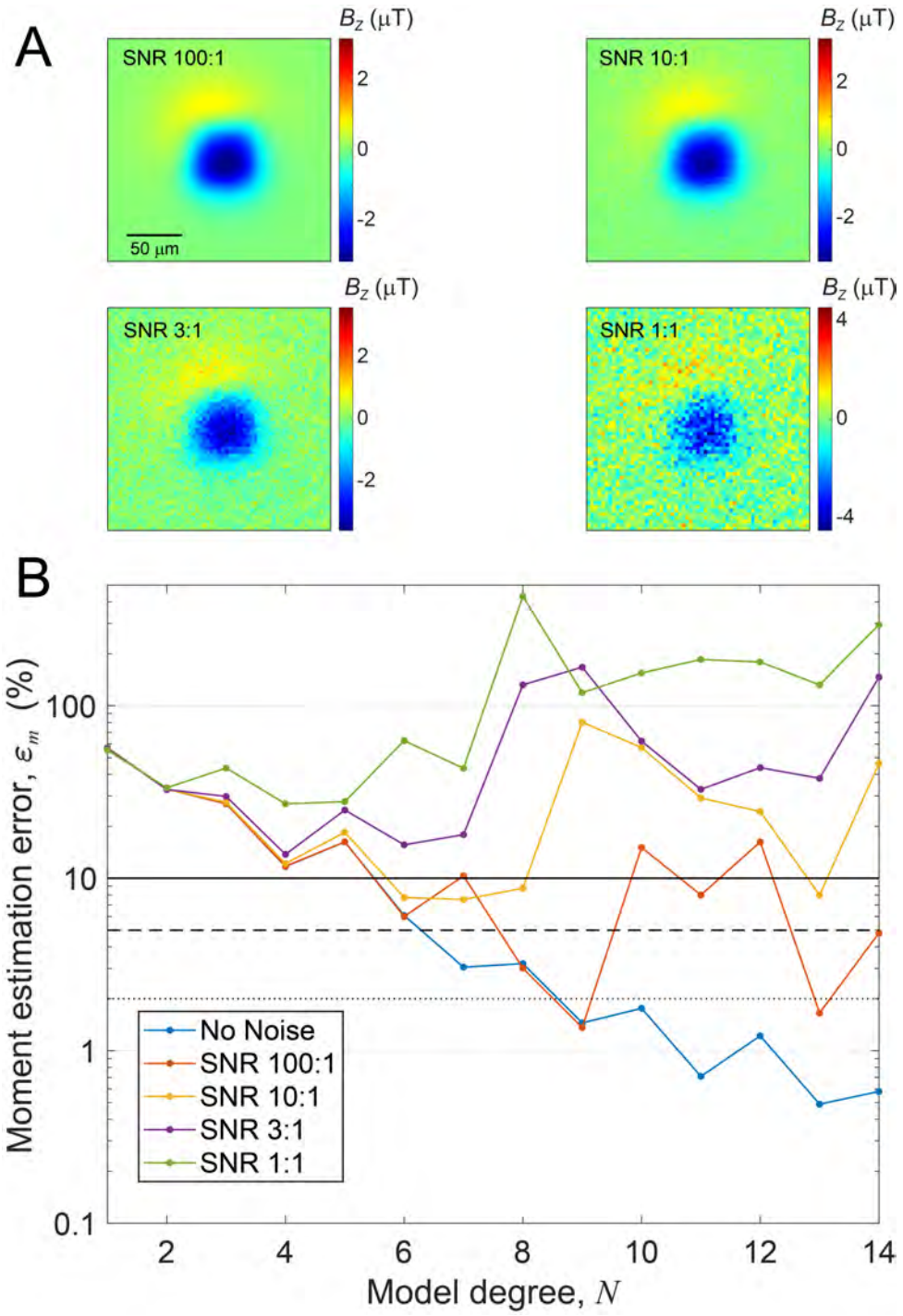


**Figure S6.** Net moment estimation results for Source C with varying model degree for different signal-to-noise ratios (SNRs). **(A)** Simulated $B_z$ field maps for a sensor-to-sample distance of 25 μm with SNR ranging from infinite (noiseless) down to 1:1. **(B)** Moment estimation error as a function of model degree for 5 different SNRs. Solid, dashed, and dotted black lines represent 10%, 5%, and 2% thresholds for the estimation error, respectively.

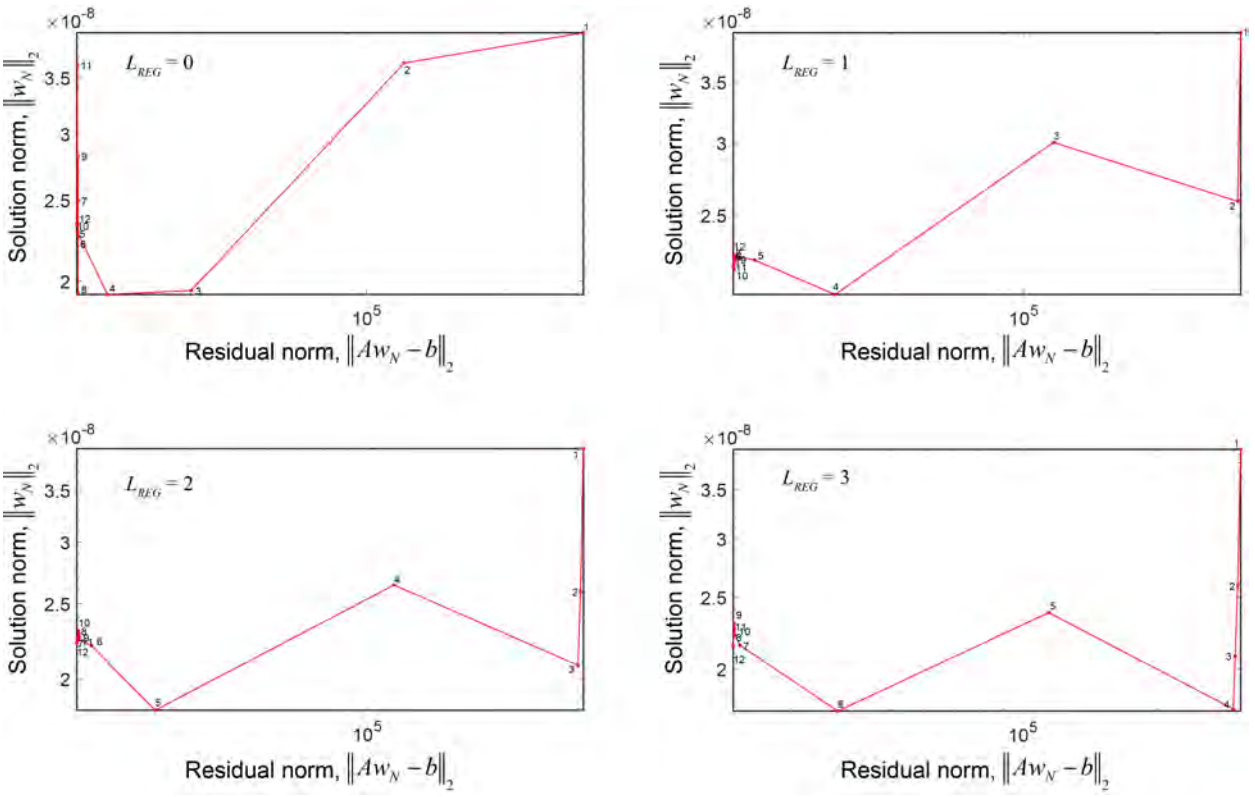


**Figure S7.** Examples of typical solution norm versus residual norm plots (L-curves) obtained in this inverse problem. In this specific example, we show curves obtained for Source A corrupted with white noise (10:1 SNR) and mapped at a 25 μm sensor-to-sample distance using different SVD truncation factors $L_{REG}$. Numbers on the curves correspond to model degrees, one of the three regularization factors acting simultaneously ($L_{REG}$ and origin location are the other two regularization factors). Notice that such curves often do not present the expected "L" shape in this problem and do not generally help in the selection of the optimal model degree. For this particular example, the optimal model degrees are: 6 ($L_{REG}$ = 0), 11/12 ($L_{REG}$ = 1), 7 ($L_{REG}$ = 2), 8 ($L_{REG}$ = 3), as determined by the minimum value of the moment estimation error.

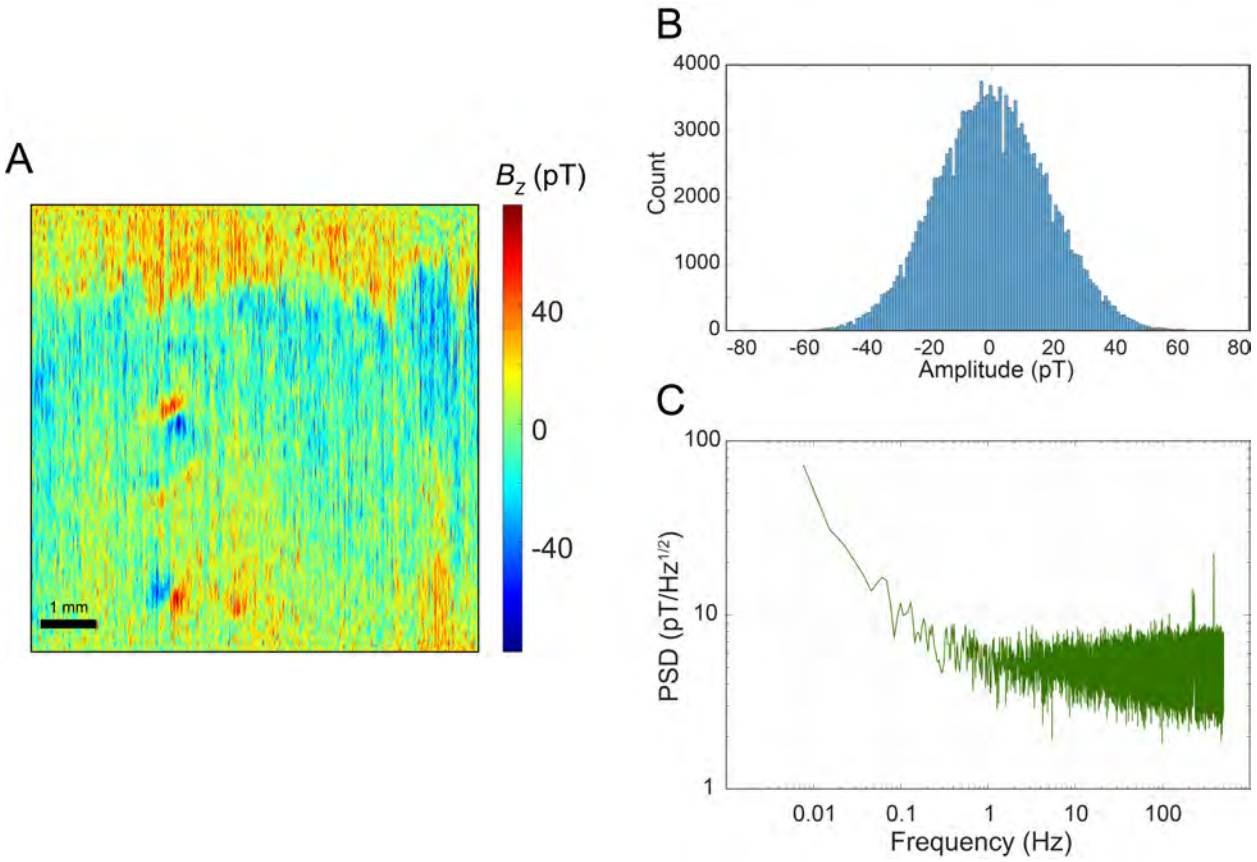


**Figure S8.** Low-critical- temperature SQUID microscope noise, measured with the MIT SQUID microscope at the most sensitive scale of the read-out electronics (i.e., largest noise amplification). **(A)** Map of the $B_z$ field of a non-magnetic sample (acid-washed Ge 124 quartz disc – 8 x 8 mm$^2$ scanning area with 20 μm step size and a sensor-to-sample distance of 180 μm), capturing several additive noise components: sensor noise, environmental noise, background contamination (e.g., dipolar features), stage motion noise, and quantization noise. Sub-regions of this field map were randomly chosen to generate the SQUID microscope noise added to synthetic maps. Each vertical scan line corresponds to a segment of the noise time series. Because magnetic measurements are not taken during the retrace scans, adjacent segments in the map are not subsequent in time, having instead a gap between them corresponding to the retrace time. As a consequence, the noise distribution differs along the scan direction versus along the transverse direction, with the latter corresponding to a very coarse sampling of the noise time series. **(B)** Distribution of noise amplitude values in the measured field map shown in (A), displaying a Gaussian (normal) behavior. **(C)** Power spectral density (PSD) of a continuous SQUID noise time series measured under similar conditions as the map shown in (A). A 1/*f* noise component dominates from DC until ~0.5 Hz, beyond which the white noise dominates.

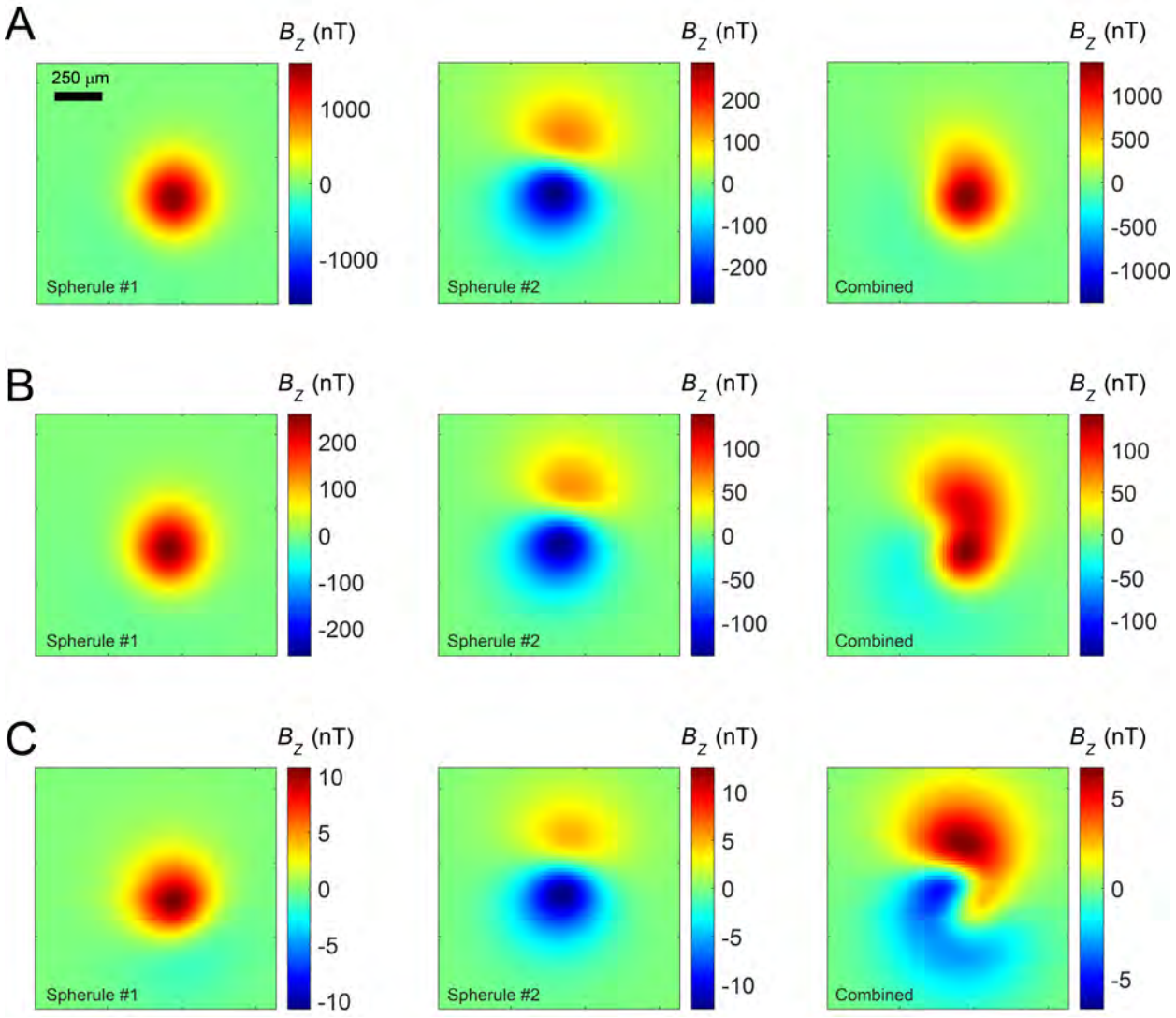


**Figure S9.** Select individual maps of two spherules from Lonar crater, India, during AF demagnetization, and resulting combined maps used for estimating net moment with the multipole expansion model. **(A)** IRM (i.e., laboratory NRM) data. **(B)** AF 40 mT step data. **(C)** AF 140 mT step data.

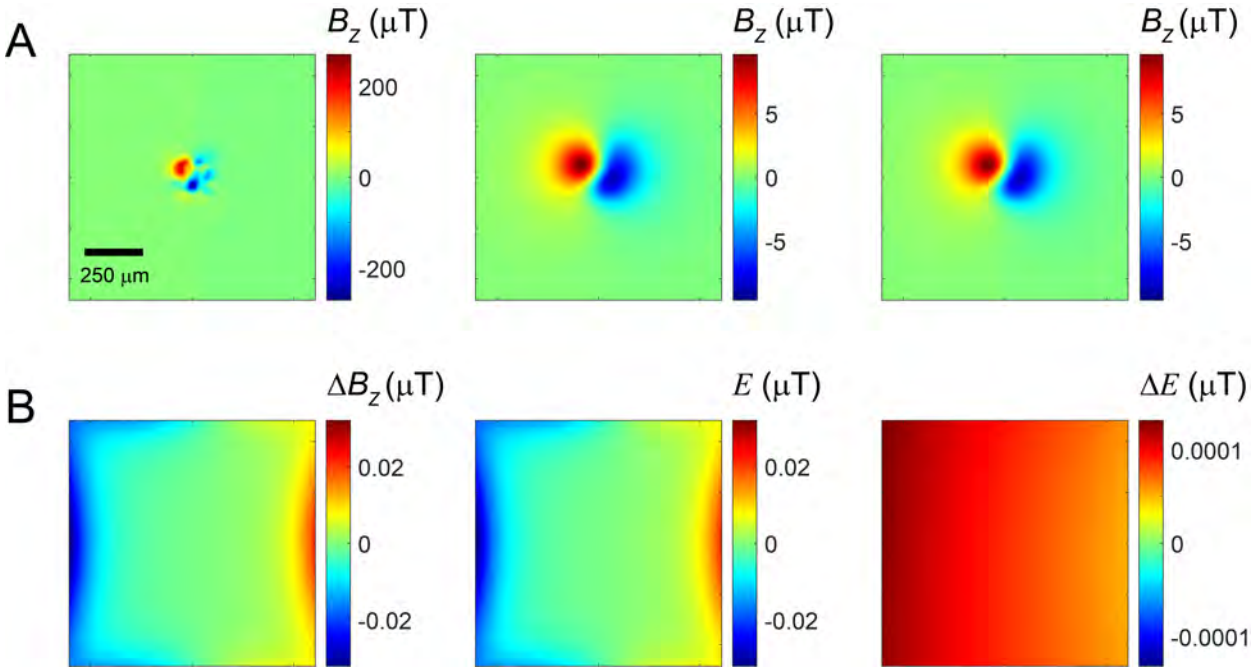


**Figure S10.** Modeling of the upward continuation error using a synthetic source comprised of a set of 50,000 dipoles with equal strength and arbitrary orientations randomly distributed in a 100 μm cubic volume. **(A)** (Left) Map of the field of the synthetic source at a sensor-to-sample distance of 25 μm. (Center) Map of the field of the synthetic source at a sensor-to-sample distance of 100 μm. (Right) Map of the field of the synthetic source shown in (A, left) upward continued by 75 μm, yielding an effective sensor-to-sample distance of 100 μm. **(B)** (Left) Difference between the true map (A, center) and the upward continued map (A, right) for a sensor-to-sample distance of 100 μm. (Center) Error in the upward continuation predicted by (S4), based on the magnetic data outside the mapping area shown in (A, left). (Right) Difference between the true upward continuation error (left) and the predicted upward continuation error due to mapping area size (center), showing that the latter accounts for >99.5% of the true error in this upward continuation calculation. Upward continuation errors are relatively small in this case owing to the enlarged mapping area, demonstrating the importance of capturing most of the field decay in the original magnetic map prior to using upward continuation. Nevertheless, as observed in a similar case shown in Fig. 11, even small errors can noticeably impact net moment estimation for complex magnetizations.

**Table S1.** Net magnetic moments obtained for a sample comprised of two impact melt spherules collected from Lonar crater, India, using two different estimation methods. **(A)** Individual magnetic moments for each spherule at different AF steps, estimated using a dipole-fitting technique. **(B)** Net magnetic moments obtained by: (i) adding the corresponding moments in (A) for each AF step (M dips, Inc Dips, Dec Dips); and (ii) using our multipole fitting estimation technique on combined maps of the spherules (M MultiP, Inc MultiP, Dec MultiP). Also shown are the multipole model degree used for the estimate in each AF step and the differences in magnitude and direction between estimates obtained with the dipole model and estimates obtained with the multipole model.

**(A)**

| AF step | | M1 | Inc1 | Dec1 | | M2 | Inc2 | Dec2 |
|---|---|---|---|---|---|---|---|---|
| **0** | | 2.49E-10 | 070.0 | 331.0 | | 7.09E-11 | -017.7 | 349.1 |
| **20** | | 1.57E-10 | 070.2 | 333.3 | | 5.44E-11 | -017.9 | 348.7 |
| **40** | | 4.08E-11 | 070.0 | 338.0 | | 2.98E-11 | -018.9 | 348.8 |
| **60** | | 1.46E-11 | 072.2 | 343.1 | | 1.94E-11 | -019.7 | 347.5 |
| **80** | | 5.15E-12 | 075.4 | 010.9 | | 1.22E-11 | -020.4 | 348.4 |
| **100** | | 2.64E-12 | 062.2 | 018.3 | | 7.23E-12 | -020.4 | 347.4 |
| **140** | | 1.83E-12 | 048.8 | 016.3 | | 2.65E-12 | -022.8 | 351.7 |
| **200** | | 1.14E-12 | 038.0 | 020.6 | | 1.48E-12 | -016.9 | 359.8 |

**(B)**

| AF step | | M Dips | Inc Dips | Dec Dips | | M MultiP | Inc MultiP | Dec MultiP | Model degree | | Magnitude Difference (%) | Angular Difference (deg) |
|---|---|---|---|---|---|---|---|---|---|---|---|---|
| **0** | | 2.61E-10 | 54.6 | 339.0 | | 2.44E-10 | 53.5 | 336.6 | 13 | | -6.6% | 1.8 |
| **20** | | 1.68E-10 | 51.5 | 340.9 | | 1.57E-10 | 49.8 | 339.4 | 14 | | -6.4% | 2.0 |
| **40** | | 5.08E-11 | 34.4 | 345.2 | | 5.14E-11 | 33.5 | 344.9 | 2 | | 1.1% | 0.9 |
| **60** | | 2.38E-11 | 18.0 | 346.7 | | 2.21E-11 | 17.6 | 344.1 | 2 | | -7.4% | 2.4 |
| **80** | | 1.26E-11 | 03.4 | 350.7 | | 1.24E-11 | 02.7 | 348.0 | 2 | | -2.0% | 2.7 |
| **100** | | 7.86E-12 | -01.3 | 352.0 | | 8.02E-12 | 00.1 | 352.8 | 7 | | 2.0% | 1.6 |
| **140** | | 3.59E-12 | 05.6 | 359.8 | | 3.31E-12 | 06.0 | 357.1 | 2 | | -7.8% | 2.7 |
| **200** | | 2.30E-12 | 06.8 | 007.8 | | 2.27E-12 | 09.1 | 005.1 | 1 | | -1.4% | 3.6 |

**Table S2:** Compilation of data type, noise type and SNR, regularization parameters, offset compensation, least-squares algorithm, and optimization algorithm used in each figure containing moment estimates in the main text and in this SI. †MATLAB's algorithm *mldivide* provides faster computation of the solution to the linear least-squares problem but does not allow for the implementation of the regularization technique. ‡MATLAB's algorithm *lsqnonlin* yields faster convergence of the optimization but less consistent solution properties that allow us to pick out the optimal solution.

| Figure | Data Type | Noise | SNR | Regularization | $L_{REG}$ | Linear Least-squares Algorithm† | Offset Compensation | Optimization Algorithm‡ |
|---|---|---|---|---|---|---|---|---|
| 2 | Synthetic | No | ∞ | No | N/A | mldivide | No | lsqnonlin |
| 3 | Synthetic | No | ∞ | No | N/A | mldivide | No | lsqnonlin |
| 4 | Synthetic | No | ∞ | No | N/A | mldivide | No | lsqnonlin |
| 5 | Synthetic | No | ∞ | No | N/A | mldivide | No | lsqnonlin |
| 6 | Synthetic | No | ∞ | No | N/A | mldivide | No | lsqnonlin |
| 7 | Synthetic | White noise | ∞, 100:1, 10:1, 3:1, 1:1 | No | N/A | mldivide | No | lsqnonlin |
| 8 | Synthetic | White noise | ∞, 100:1, 10:1, 3:1, 1:1 | No | N/A | mldivide | No | lsqnonlin |
| 9 | Synthetic | White noise | 3:1 | Yes | 0 – 6 | svds | No | lsqnonlin |
| 10 | Synthetic | White noise | 3:1 | Yes | 0 | svds | No | lsqnonlin |
| 11 | Synthetic | No | ∞ | No | N/A | mldivide | No | lsqnonlin |
| 12 | Synthetic | No | ∞ | No | N/A | mldivide | Yes | lsqnonlin |
| 13 | Synthetic | SM noise | 3:1, 1:1 | Yes | 1 – 3 | svds | Yes | fminunc |
| 14 | Synthetic | SM noise | 3:1 | Yes | 0 – 3 | svds | Yes | fminunc |
| 16 | Experimental | N/A | N/A | Yes | 0 – 3 | svds | Yes | fminunc |
| 17 | Experimental | N/A | N/A | Yes | 1 – 4 | svds | Yes | fminunc |
| S2 | Synthetic | No | ∞ | No | N/A | mldivide | No | lsqnonlin |
| S3 | Synthetic | No | ∞ | No | N/A | mldivide | No | lsqnonlin |
| S4 | Synthetic | White noise | ∞, 100:1, 10:1, 3:1, 1:1 | No | N/A | mldivide | No | lsqnonlin |
| S5 | Synthetic | White noise | ∞, 100:1, 10:1, 3:1, 1:1 | No | N/A | mldivide | No | lsqnonlin |
| S6 | Synthetic | White noise | 10:1 | Yes | 0 – 3 | svds | No | fminunc |